

# Cooling and Manipulating Trapped Molecular Ions



Ivan Storgaard Vogelius

Department of Physics and Astronomy  
University of Aarhus, Denmark

PhD Thesis

---

This thesis is submitted to the Faculty of Science at the University of Aarhus, Denmark, in order to fulfill the requirements for obtaining the PhD degree in Physics.

The studies have been carried out under the supervision of Associate Professor Lars Bojer Madsen and Associate Professor Michael Drewsen at the Department of Physics and Astronomy, University of Aarhus, from July 2001 to August 2005.

# Contents

<b>List of Publications</b>	<b>vii</b>
<b>Preface</b>	<b>ix</b>
<b>Abstract</b>	<b>xi</b>
<b>1 Introduction to the Thesis</b>	<b>1</b>
1.1 Outline of the Thesis . . . . .	2
<b>2 Introduction to Cold, Trapped Ions</b>	<b>5</b>
2.1 The Harmonic Oscillator . . . . .	5
2.2 A Two Level Atom Interacting with Light . . . . .	6
2.2.1 Effect of spontaneous decay . . . . .	8
2.3 Elements of Molecular Physics . . . . .	8
2.3.1 Structure of diatomic molecules . . . . .	9
2.3.2 Selection rules for radiative transitions . . . . .	11
2.3.3 Polyatomic molecules . . . . .	11
2.4 Stimulated Raman Adiabatic Passage – STIRAP . . . . .	12
2.4.1 STIRAP in the interaction picture . . . . .	13
2.5 The Linear Paul Trap . . . . .	16
2.6 Laser Cooling . . . . .	18
2.6.1 Doppler cooling . . . . .	19
2.6.2 Cooling of ions in a trap . . . . .	21
2.6.3 Sympathetic cooling of ions . . . . .	24
<b>3 Blackbody-Radiation-Assisted Laser Cooling of Molecular Ions</b>	<b>29</b>
3.1 Cooling Concept . . . . .	30
3.2 Numerical Simulations . . . . .	31
3.2.1 Rate equations for the population dynamics . . . . .	31
3.2.2 Calculation of molecular properties . . . . .	32
3.2.3 Solving the population dynamics . . . . .	35
3.2.4 Numerical results . . . . .	37
3.3 Direct Two-Laser Scheme . . . . .	38
3.4 Laser Cooling of Molecular Rotations Assisted by Incoherent Sources . . . . .	40

---

3.4.1	Cooling schemes . . . . .	40
3.4.2	Numerical simulations . . . . .	42
3.5	Conclusion . . . . .	46
<b>4</b>	<b>Cooling of Molecular Ions with Rotational Substructure</b>	<b>47</b>
4.1	$(^{2S+1})\Pi$ -states; Hunds Case (a) . . . . .	47
4.1.1	Energy levels and selection rules . . . . .	48
4.1.2	Cooling schemes . . . . .	49
4.1.3	Numerical simulations . . . . .	50
4.2	$(^{2S+1})\Sigma$ -states; Hunds Case (b) . . . . .	52
4.2.1	Energy levels of doublet states . . . . .	53
4.2.2	Energy levels of triplet states . . . . .	53
4.2.3	Selection rules . . . . .	54
4.2.4	Cooling scheme . . . . .	55
4.2.5	Numerical simulations . . . . .	55
4.3	Conclusion . . . . .	60
<b>5</b>	<b>Quantized Motion of Charged Particles in a Trap</b>	<b>61</b>
5.1	A Single Ion in a Harmonic Trap . . . . .	61
5.1.1	Energy eigenstates . . . . .	61
5.1.2	Transition matrix elements . . . . .	62
5.2	Strings of Ions in a Trap . . . . .	64
5.2.1	Equilibrium positions and vibrational modes . . . . .	64
5.2.2	The quantized vibrational motion . . . . .	66
5.2.3	Transition matrix elements . . . . .	66
<b>6</b>	<b>Internal Cooling of Molecules Through Atomic Cooling Cycles</b>	<b>69</b>
6.1	Sympathetic Cooling of the Axial Modes . . . . .	69
6.2	Internal Cooling . . . . .	71
6.3	Numerical Simulations . . . . .	74
6.3.1	Complications and prospects for improvement . . . . .	77
6.4	Conclusion . . . . .	79
<b>7</b>	<b>State Preparation by Projection Measurement</b>	<b>81</b>
7.1	Introduction . . . . .	81
7.2	Selection Sequence . . . . .	82
7.3	Efficiency of the CEI and CS Steps . . . . .	83
7.3.1	Correlation of external motion and the internal molecular state (CEI) . . . . .	84
7.3.2	External state conditional shelving (CS) . . . . .	90
7.4	Imperfections in the Individual Steps . . . . .	92
7.5	Over-all Confidence of Steps 1-4 . . . . .	93
7.6	State Purification (SP) . . . . .	94
7.6.1	Confidence of the selection sequence after SP . . . . .	94
7.6.2	Alternative approach . . . . .	95

## CONTENTS

---

7.7 Conclusion . . . . .	95
<b>8 Summary and Outlook</b>	<b>97</b>
<b>Acknowledgements</b>	<b>99</b>
<b>A Einstein Coefficients</b>	<b>101</b>
<b>B Hönl-London Factors of <math>^1\Sigma</math> States</b>	<b>103</b>
<b>C Hönl-London Factors for Hunds Case (a) and (b)</b>	<b>105</b>
C.1 Hunds Case (a) . . . . .	105
C.2 Hunds Case (b) . . . . .	106
<b>Bibliography</b>	<b>109</b>



# List of Publications

- I. I. S. Vogelius, L. B. Madsen, and M. Drewsen. *Blackbody-Radiation-Assisted Laser Cooling of Molecular Ions*. Phys. Rev. Lett. **89** 173003 (2002).
- II. I. S. Vogelius, L. B. Madsen, and M. Drewsen. *Rotational Cooling of Molecules Using Lamps*. J. Phys. B: At. Mol. Opt. Phys. **37**, 4571 (2004).
- III. I. S. Vogelius, L. B. Madsen, and M. Drewsen. *Rotational Cooling of Heteronuclear Molecular Ions with  $^1\Sigma$ ,  $^2\Sigma$ ,  $^3\Sigma$ , and  $^2\Pi$  Electronic Ground States*. Phys. Rev. A **70**, 053412 (2004).
- IV. A. Bertelsen, I. S. Vogelius, S. Jørgensen, R. Kosloff and M. Drewsen. *Photodissociation of Cold  $\text{MgH}^+$  Ions Towards Rotational Temperature Measurements and Controlled Dissociation*. Eur. Phys. J. D **31**, 403 (2004).
- V. I. S. Vogelius, L. B. Madsen, and M. Drewsen. *Probabilistic State Preparation of a Single Molecular Ion by Projection Measurement*. physics/0507181. Submitted for publication.
- VI. I. S. Vogelius, L. B. Madsen, and M. Drewsen. *Rotational Cooling of Molecules Through Atomic Cooling Cycles*. Manuscript in preparation.





# Preface

The present thesis is based on my work as a PhD student during the last four years at the University of Aarhus under supervision of Lars Bojer Madsen and Michael Drewsen. The goal of the project has been to develop cooling schemes for the internal degrees of freedom of translationally cold molecular ions in traps. While the project is theoretical, a close connection to the experimental group have been maintained throughout. As a result, the developed cooling schemes have been reconsidered several times and continuously modified to facilitate experimental realization. As a student, it has been very interesting to work on the borderline of theory and experiment and I certainly feel that I have learned important things by the interplay and that the final result is better than it would have been without cooperation with experimental group.

Ivan Storgaard Vogelius  
August, 2005



# Abstract

**Dansk resumé.** *Laserkøling af atomer har gennem de seneste 20 år ført til en mængde spændende resultater og en opblomstring af nye forskningsområder som f.eks. kvantecomputere. Med baggrund i denne succes er det naturligt at undersøge mulighederne for at laserkøle molekyler. Grundet molekylers komplekse indre struktur er det imidlertid ikke muligt direkte at overføre de atomare kølingsskemaer til molekyler. I denne afhandling undersøges mulighederne for at køle molekylære ioner. Den eksterne bevægelse af molekylære ioner kan køles relativt let ved at fange dem sammen med kolde atomare ioner, men molekylerne vil fortsat rotere og vibrere. I afhandlingen afdækkes et antal eksperimentelt attraktive metoder til at køle og kontrollere den rotationelle og vibrationelle bevægelse af sådanne molekylioner.*

Laser cooling of atoms has been the subject of intense investigation during the last two decades. The new experimental possibilities have led to new research areas, such as quantum logic, and initiated renewed interest in atomic physics in general. The large impact of laser cooling was recognized with the Nobel Prize in 1997 to Steven Chu, Claude Cohen-Tannoudji, and William D. Phillips for development of methods to cool and trap atoms with laser light, and later, in 2001, Eric A. Cornell, Wolfgang Ketterle, and Carl E. Wieman were awarded the price for the achievement of Bose-Einstein condensation in dilute gases of alkali atoms, and for early fundamental studies of the properties of the condensates.

With the success of laser cooling of atoms in mind, it is natural to consider possibilities for applying laser cooling techniques to molecules. Unfortunately, the complex rotational and vibrational structure of molecules prevents the direct application of the laser cooling techniques developed for atoms. In this thesis, possibilities for cooling and controlling molecular ions are considered. The strength of the Coulomb interaction results in highly effective sympathetic cooling of the translational degrees of freedom of molecular ions that are trapped in an environment with laser cooled atomic ions. It turns out that the rotational and vibrational degrees of freedom of such translationally cooled molecular ions remain unaffected by the sympathetic cooling. In the thesis, a number of schemes to cool the rotational degrees of freedom of molecular ions are presented and a scheme for state-specific preparation of a molecular ion by projection measurement is proposed. It is shown that cooling and projection measurement of a large number of molecular ion species is experimentally feasible.



# CHAPTER 1

## Introduction to the Thesis

Powerful techniques for manipulating, cooling and trapping atoms have recently paved the way for extremely detailed investigations of atomic physics phenomena, as well as been essential ingredients in the development of research fields such as atom optics [1], physics of trapped condensed dilute gases [2] and quantum information [3]. Such powerful techniques have not yet been established for molecules, but the field is presently experiencing increased interest and many promising approaches are being investigated.

Although molecules are routinely cooled internally and translationally in supersonic expanded beams [4], their high average translational velocities ( $\sim 100$  -  $1000$  m/s) limit this method to experiments requiring only short interaction times. Effective methods to cool and trap molecules are therefore highly desired. Unfortunately, molecules are more difficult to cool than atoms due to the absence of closed optical pumping cycles. However, several different routes for obtaining cold molecules have been investigated [5–7], but so-far only a few methods have been sufficiently simple to have allowed for experimental demonstration. These schemes include production of cold molecules from an ultracold cloud of atoms using a tunable Feshbach resonance [8–12] or photoassociation [13, 14], cooling by collision with a low temperature buffer gas [7, 15], and deceleration and trapping of polar molecules by electric fields [16–22]. One of the most important results have been achievement of Bose-Einstein condensates of weakly bound molecules [23–27], which sparked a wealth of investigations of the crossover between Bardeen-Cooper-Schreiffer (BCS)-type superfluidity and Bose-Einstein condensation [28–32].

Molecular ions constitute another class of molecules that are interesting to cool and manipulate. Promising applications of cold, trapped molecular ions include investigations of collision and reaction dynamics at low temperature [33], high-resolution spectroscopy [34], coherent control experiments [35], and state specific reactions studies [36, 37]. For much of this research, long-term localized and state-specific targets are highly desirable.

In this thesis we consider several ways to obtain such targets. We consider trapped molecular ions sympathetically cooled by atomic ions [38, 39], where

previous investigations show that molecular ions can be translationally cooled to temperatures of a few mK, at which stage they become immobile and localize spatially in Coulomb crystal structures [38, 40]. Though these molecules are translationally cold, studies indicate that the internal degrees of freedom of at least smaller hetero-nuclear molecules, due to their interaction with the black-body radiation (BBR), are close to be in equilibrium with the temperature of the surroundings [41, 42]. This is not unexpected since the many order of magnitude difference between the internal transitions frequencies in the molecule ( $\gtrsim 10^{11}$  Hz) and the frequency of the collective vibrational modes in the Coulomb crystals ( $\lesssim 10^7$  Hz) leads to very inefficient coupling between these degrees of freedom. In the thesis, several schemes for rotational cooling of such translationally cold, but internally hot molecular ions are proposed. We consider realistic experimental constraints for the implementations of the schemes and show that the schemes are feasible to implement with present day technology.

## 1.1 Outline of the Thesis

The thesis is organized as follows

**Chapter 2.** A short description of basic physics of trapped molecular ions is presented. The chapter includes a brief discussion of the linear Paul trap, used for trapping and cooling atomic and molecular ions. The structure and dynamics of molecules is discussed and sympathetic cooling of molecular ions in a trap is shown. Finally, the chapter ends with experimental data showing that  $\text{MgH}^+$  is translationally cooled by simultaneously trapped and laser cooled  $\text{Mg}^+$ , but the rotational temperature of the molecular ions remain unaffected by sympathetic cooling.

**Chapter 3.** Schemes for cooling of the rotational degrees of freedom of translationally cooled molecular ions is presented. Numerical simulations show that the schemes can cool the rotational degree of freedom of various diatomic heteronuclear molecular ions with  $^1\Sigma$  electronic ground state. The schemes are relatively simple and realistic experimental conditions are considered.

**Chapter 4** The schemes of chapter 3 are extended to more complex electronic ground states of heteronuclear molecular ions. It is shown that it is experimentally realistic to cool heteronuclear ions with various electronic ground states.

**Chapter 5** The quantized motion of ions in a harmonic trap is discussed and a formalism is developed allowing the calculation of motional transition matrix elements. The chapter represents an intermezzo before novel schemes for cooling and manipulation of molecular ions is presented in the subsequent chapters.

**Chapter 6** A method to cool the internal degrees of freedom of molecular ions without a dissipative process in the molecular ions is presented. The scheme functions by coupling the internal state of the molecular ions and the collective state of an atomic and molecular ion in a trap, thus allowing cooling of the molecular ion through the atomic cooling cycles. Since the cooling

concept does not involve spontaneous decay in the molecule, it is largely independent of internal molecular structure and dynamics and may thus be applied to molecules that cannot be cooled with the previous schemes, e.g. polyatomic molecules.

**Chapter 7** A method for state preparation of a molecular ion by projection measurement is presented. The method is based on correlation of the internal state of the molecular ion and the collective motional state of the two ion system. Detection of the molecular states then proceeds by detection of the collective motional state by the atomic shelving method. Numerical simulations are used to demonstrate effective state preparation of a large number of rotational states of  $\text{MgH}^+$  and the application to more complex molecules is considered.

**Chapter 8** The results of the previous chapters are briefly summarized and discussed and possible future work is considered.





# CHAPTER 2

## Introduction to Cold, Trapped Ions

In this chapter some fundamental processes in quantum mechanics, trapping and laser cooling is discussed. The focus is on the mechanisms necessary to gain a basic understanding of trapping and cooling of charged atoms and molecules. For a more concise discussion of the basic quantum mechanical concepts the reader should consult standard quantum mechanics textbooks, e.g. the excellent books by Griffith and Sakurai [43, 44].

### 2.1 The Harmonic Oscillator

The Hamiltonian for a particle with mass  $m$  in a harmonic oscillator potential of frequency  $\Omega$  is given by

$$H = \frac{p^2}{2m} + \frac{1}{2}m\Omega^2 x^2 \quad (2.1)$$

The most elegant way of treating this system is by operator methods. Define the ladder operators  $a_{\pm} = \sqrt{\frac{m\Omega}{2\hbar}}x \mp i\frac{p}{\sqrt{2m\Omega\hbar}}$ . Using  $[x, p] = i\hbar$  we find the important relations

$$\begin{aligned} [a_-, a_+] &= 1 \\ H &= \hbar\Omega(a_+a_- + \frac{1}{2}) \end{aligned} \quad (2.2)$$

Assume that  $|n\rangle$  is an eigenfunction of  $H$  with energy  $E$ . Using only equation(2.2) we then find that  $a_{\pm}|n\rangle$  are also eigenfunctions of  $H$  with energy  $E \pm \hbar\Omega$ . Now, since no eigenstate can have negative energy, we may fix the bottom of the spectrum  $|0\rangle$  as the non-trivial eigenstate fulfilling  $a_-|0\rangle = 0$ . From

equation (2.2) we find that  $H|0\rangle = \frac{1}{2}\hbar\Omega$ . The spectrum has then be derived

$$H|n\rangle = \hbar\Omega(n + \frac{1}{2})|n\rangle \quad (2.3)$$

The norm of  $a_{\pm}|n\rangle$  can be calculated directly using equation (2.2)

$$\begin{aligned} a_+|n\rangle &= \sqrt{n+1}|n+1\rangle \\ a_-|n\rangle &= \sqrt{n}|n-1\rangle \end{aligned} \quad (2.4)$$

## 2.2 A Two Level Atom Interacting with Light

Let us consider a two level atom obeying the Hamiltonian

$$H_{\text{atom}} = \omega_g|g\rangle\langle g| + \omega_e|e\rangle\langle e|. \quad (2.5)$$

Assume that this two level atom is subject to an incident monochromatic plane wave of frequency  $\omega$ ,  $\mathbf{E}(\mathbf{r}, t) = -\frac{1}{2}\hat{\epsilon}E_0e^{i(\mathbf{k}\cdot\mathbf{r}-\omega t)} + c.c.$  The interaction Hamiltonian, in the case of a moderate power near resonant field, is then given by

$$H_{\text{int}} = -\frac{1}{2}E_0\langle e|\hat{\epsilon}\cdot\mathbf{r}|g\rangle e^{-i\omega t}|e\rangle\langle g| + h.c., \quad (2.6)$$

where we have used the dipole approximation,  $e^{i\mathbf{k}\cdot\mathbf{r}} \simeq 1$  and applied the rotating wave approximation [RWA], which is valid for moderate intensity fields [45].

Define the Rabi frequency  $\Omega_{\text{Rabi}} = -eE_0\langle e|\hat{\epsilon}\cdot\mathbf{r}|g\rangle$ . By choosing an appropriate phase of  $|g\rangle$  and  $|e\rangle$ , one can absorb a possible complex phase of  $\Omega_{\text{Rabi}}$  in the wave functions, provided  $\hat{\epsilon}E_0$  is constant. In the remainder of this thesis we shall assume this has been done, implying that  $\Omega_{\text{Rabi}}$  is real and positive. The expression in equation (2.6) can thus be reduced to

$$H_{\text{int}} = -\hbar\frac{1}{2}\Omega_{\text{Rabi}}|e\rangle\langle g|e^{-i\omega t} - \hbar\frac{1}{2}\Omega_{\text{Rabi}}|g\rangle\langle e|e^{i\omega t}. \quad (2.7)$$

Choose the energy so  $\omega_g = 0$  and  $\omega_e = \omega_{ge} = \omega_e - \omega_g$ . The general atomic wave function can be written  $|\Psi\rangle = c_g|g\rangle + c_e|e\rangle$  and the Schrödinger equation is given by

$$\frac{d}{dt}\begin{bmatrix} c_g \\ c_e \end{bmatrix} = -i\begin{bmatrix} 0 & \frac{1}{2}\Omega_{\text{Rabi}}e^{i\omega t} \\ \frac{1}{2}\Omega_{\text{Rabi}}e^{-i\omega t} & \omega_e \end{bmatrix}\begin{bmatrix} c_g \\ c_e \end{bmatrix}. \quad (2.8)$$

Introducing  $a_g(t) = c_g(t)$  and  $a_e(t) = c_e(t)e^{i\omega t}$  the above expression can be rewritten as

$$\frac{d}{dt}\begin{bmatrix} a_g \\ a_e \end{bmatrix} = -i\begin{bmatrix} 0 & \frac{1}{2}\Omega_{\text{Rabi}} \\ \frac{1}{2}\Omega_{\text{Rabi}} & \Delta \end{bmatrix}\begin{bmatrix} a_g \\ a_e \end{bmatrix}, \quad (2.9)$$

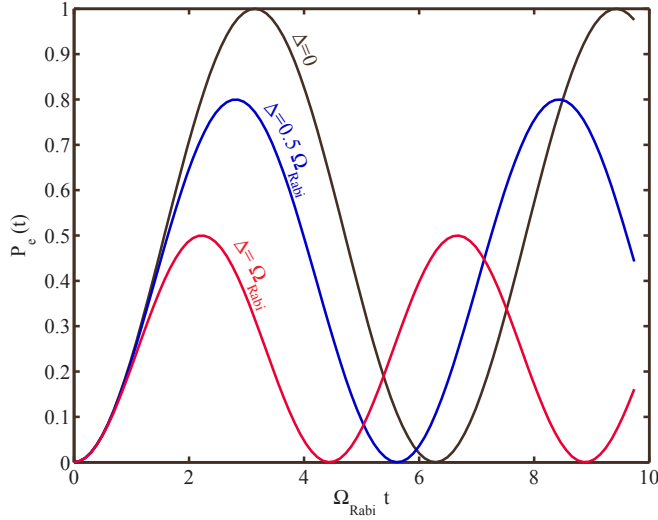


**Figure 2.1:** Population in  $|e\rangle$  as function of time for three detunings. On resonance, the population performs harmonic oscillations with frequency  $\Omega_{\text{Rabi}}$ , while increasing detuning results in a higher frequency of Rabi oscillations, but lower amplitude.

where we defined the detuning  $\Delta = \omega - \omega_{eg}$ . Equation(2.9) is solved by the expressions [45]

$$\begin{aligned} a_g(t) &= \left[ \cos\left(\frac{\chi t}{2}\right) + i \frac{\Delta}{\chi} \sin\left(\frac{\chi t}{2}\right) \right] e^{-i\Delta t/2} \\ a_e(t) &= \left[ -i \frac{\Omega_{\text{Rabi}}}{\chi} \sin\left(\frac{\chi t}{2}\right) \right] e^{-i\Delta t/2}, \end{aligned} \quad (2.10)$$

where we introduced the off-resonant Rabi frequency  $\chi = \sqrt{\Delta^2 + \Omega_{\text{Rabi}}^2}$ .

Assuming that the atom is in the ground state at time  $t = 0$  we find the population in the excited state as function of time to be

$$P_e(t) = |a_e(t)|^2 = \frac{\Omega_{\text{Rabi}}^2}{\chi^2} \sin^2\left(\frac{\chi t}{2}\right). \quad (2.11)$$

We immediately see, that the population performs harmonic oscillations - Rabi oscillations - with frequency  $\chi$ . Figure 2.1 shows the excited state population against time for a number of detunings.

It should be emphasized that in applying the rotating wave approximation, we assume moderate field strengths, as multi-photon transitions could otherwise be significant. If multi-photon transitions are significant, the theory developed by Shirley should be applied [46].

### 2.2.1 Effect of spontaneous decay

In order to include the effect of spontaneous emission, we introduce the density matrix,  $\rho$  [44, 45].

$$\rho = \begin{bmatrix} \rho_{11} & \rho_{12} \\ \rho_{21} & \rho_{22} \end{bmatrix} = \begin{bmatrix} c_g c_g^* & c_g c_e^* \\ c_e c_g^* & c_e c_e^* \end{bmatrix}. \quad (2.12)$$

The equation of motion for the density matrix, with spontaneous decay from  $|e\rangle$  to  $|g\rangle$  with rate  $\Gamma$  included, is given by [47, page 23] [45, page 205] (check)

$$\begin{aligned} \frac{d\rho_{11}}{dt} &= \Gamma\rho_{22} + \frac{i}{2}(\Omega e^{-i\Delta t}\rho_{12} - \Omega e^{i\Delta t}\rho_{21}) \\ \frac{d\tilde{\rho}_{12}}{dt} &= -\left(\frac{\Gamma}{2} - i\Delta\right)\rho_{12} - \frac{i}{2}\Omega e^{i\Delta t}(\rho_{22} - \rho_{11}) \\ \frac{d\tilde{\rho}_{21}}{dt} &= -\left(\frac{\Gamma}{2} + i\Delta\right)\tilde{\rho}_{21} + \frac{i}{2}\Omega e^{-i\Delta t}(\rho_{22} - \rho_{11}) \\ \frac{d\rho_{22}}{dt} &= -\Gamma\rho_{22} - \frac{i}{2}(\Omega e^{-i\Delta t}\tilde{\rho}_{12} - \Omega e^{i\Delta t}\rho_{21}). \end{aligned} \quad (2.13)$$

Equation (2.13) generally has to be solved numerically. One finds that the solutions perform damped Rabi oscillations reaching steady state for  $t \gg \Gamma^{-1}$ . At steady state ( $\dot{\rho} = 0$ ) we find the excited state population

$$\rho_{22} = \frac{\Omega^2/4}{\Delta^2 + \Omega^2/2 + \Gamma^2/4} = \frac{s}{2(1+s)}, \quad (2.14)$$

where we introduced the saturation parameter  $s = \frac{\Omega^2/2}{\delta^2 + \Gamma^2/4}$ , illustrating the asymptotic behavior  $\rho_{22} \rightarrow \frac{1}{2}$  for  $\Omega \rightarrow \infty$ .

In steady state the spontaneous decay rate from the excited state,  $\Gamma\rho_{22}$ , equals the net excitation rate from the ground state,  $\gamma$ . Hence, a steady state expression for the line profile is given by the power-broadened Lorentzian

$$\gamma = \Gamma \frac{\Omega^2/4}{\Delta^2 + \Omega^2/2 + \Gamma^2/4}. \quad (2.15)$$

## 2.3 Elements of Molecular Physics

In this section, some general properties of molecules will be discussed with emphasis on the structure of internal energy levels and selection rules for radiative transitions.

In this section, attention is given mostly to diatomic molecules, as they have the simplest structure and are therefore more likely to be amenable for controlled manipulations. Some of the schemes to be considered later in this thesis may, however, be used for polyatomic molecules, so such molecules will be considered briefly. Good sources for a basic understanding of the physics of both diatomic and polyatomic molecules are [48–50], while the classics [51] and [52] give more detailed accounts. For a thorough description of diatomic molecular spectra in a more modern formalism, reference [53] is recommended.

### 2.3.1 Structure of diatomic molecules

Neglecting spin-interactions, the Hamiltonian for a general diatomic molecule with  $N$  electrons is:

$$\begin{aligned}
 H = & - \sum_{i=1}^N \frac{\hbar^2}{2m_e} \nabla_i^2 - \sum_{j=1,2} \frac{\hbar^2}{2M_j} \nabla_j^2 - \sum_{i=1}^N \sum_{j=1,2} \frac{Z_j e^2}{4\pi\epsilon_0 |\mathbf{r}_i - \mathbf{R}_j|} \\
 & + \sum_{i < j} \frac{e^2}{4\pi\epsilon_0 |\mathbf{r}_i - \mathbf{r}_j|} + \frac{Z_1 Z_2 e^2}{4\pi\epsilon_0 |\mathbf{R}_1 - \mathbf{R}_2|}.
 \end{aligned} \tag{2.16}$$

Here  $\mathbf{r}_i$  and  $\mathbf{R}_j$  denote the position of the  $i$ th electron and the  $j$ th nucleus, respectively, while  $\nabla_i$  and  $\nabla_j$  denote differentiation with respect to the corresponding coordinate. Similarly  $m_e$ ,  $M_j$  and  $Z_j$  denote the electron mass, the mass of the  $j$ th nucleus, and the charge of the  $j$ th nucleus.

Since  $m_e \ll M_j$  we may apply the Born-Oppenheimer approximation, in which the electronic wave function is assumed to adapt to the internuclear distance,  $\mathbf{R} = \mathbf{R}_2 - \mathbf{R}_1$ , instantly. The total molecular wave function  $\Psi(\mathbf{R}, \mathbf{r}_i)$  can then be expanded on the complete set of electronic wave functions  $\phi_k(\mathbf{R}, \mathbf{r}_i)$  solving the stationary Schrödinger equation for the electrons at fixed  $\mathbf{R}$ . The expansion coefficients are the nuclear wave functions

$$\Psi(\mathbf{R}, \mathbf{r}_i) = \sum_k F(\mathbf{R}) \phi_k(\mathbf{R}, \mathbf{r}_i). \tag{2.17}$$

As both wave functions in the expansion depend on  $\mathbf{R}$ , the Schrödinger equation will contain a term  $2\nabla_{\mathbf{R}} F(\mathbf{R}) \cdot \nabla_{\mathbf{R}} \phi_k(\mathbf{R}, \mathbf{r}_i)$  preventing the separation of the equation for the nuclear wave function. In the Born-Oppenheimer approximation this term is neglected, since  $|\nabla_{\mathbf{R}} \phi_k(\mathbf{R}, \mathbf{r}_i)| \ll |\nabla_{\mathbf{R}} F(\mathbf{R})|$  is typically fulfilled close to the equilibrium internuclear distance,  $R_e$  [48, 49]. A separated equation for the nuclear wave function is then obtained

$$\left[ -\frac{\hbar^2}{2\mu} \nabla_{\mathbf{R}}^2 + E_s(\mathbf{R}) - E \right] F(\mathbf{R}) = 0. \tag{2.18}$$

Here  $E_s(\mathbf{R})$  is the eigenvalue of the electronic Hamiltonian at internuclear distance  $\mathbf{R}$ ,  $E$  is the total energy of the system and  $\mu$  is the reduced mass of the nuclei. To further simplify the problem, assume that the total angular momentum of the electrons is zero, which implies that  $E_s(\mathbf{R})$  is spherically symmetric. The well-known procedure for solving the radial wave equation for atoms may then be applied by writing  $F_s(\mathbf{R}) = R^{-1} f_{\nu, N}^s(R) Y_{N, M_N}(\theta, \phi)$ , with  $Y_{N, M_N}(\theta, \phi)$  being the spherical harmonics and  $\nu$  the quantum number corresponding to vibrational motion - formally equivalent to the principal quantum number in the atomic case. We use  $N$  to denote the rotational quanta, reserving  $J$  for coupled angular momentum. An equation for  $f_{\nu, N}^s$  is then obtained

$$\left[ -\frac{\hbar^2}{2\mu} \left( \frac{d^2}{dR^2} - \frac{N(N+1)}{R^2} \right) + E_s(R) - E_{s, \nu, N} \right] f_{\nu, N}^s = 0. \tag{2.19}$$

In the rigid rotator approximation this gives a rotational energy of  $E_{rot} = \frac{\hbar^2}{2\mu R_e^2} N(N+1)$  and  $2N+1$ -fold degeneracy of each rotational state. The vibrational energy spectrum is found by expanding  $E_s(R)$  around the minimum at  $R_e$ ,  $E_s(R) \simeq E_S(R_e) + \frac{1}{2} \frac{d^2 E(R)}{dR^2} \Big|_{R_e} (R - R_e)^2$ . Equation (2.19) is thus reduced to the equation of a harmonic oscillator and the vibrational part of the energy spectrum takes the form  $E_\nu = \hbar\omega(\nu + \frac{1}{2})$  with  $\omega = \sqrt{\frac{d^2 E(R)}{\mu dR^2} \Big|_{R_e}}$ .

The results above give the basic features of the structure of diatomic molecules. The energy difference between electronic states dominate (typically in the visible or ultraviolet range), followed by the vibrational structure with typical energies on the order of thousands of  $\text{cm}^{-1}$  (infrared range) and, finally, the rotational energies are the smallest, being on the order of tens of  $\text{cm}^{-1}$  (far-infrared or millimeter range). For the lighter species the vibrational energy spacing will generally be large enough to secure that only the ground vibrational band will be populated if the molecules are in equilibrium with black-body-radiation (BBR) at room temperature, while many rotational levels will normally be populated. The main focus in this thesis is to present theoretical schemes for controlling the ro-vibrational degrees of freedom in molecular ions that are initially in equilibrium with BBR at room temperature.

To estimate the accuracy of the approximations involved, we note that the harmonic approximation of the electronic potential is good at low values of  $\nu$  as such nuclear wave functions will only be significant close to  $R_e$ , while the rigid rotator approximation also requires a moderate  $N$ . These conditions will typically be fulfilled if the molecules are in equilibrium with BBR. Hence, the basic considerations presented here suffice to explain the essence of the cooling schemes presented in the following chapters.

### Substructure of the ro-vibrational spectrum

Interactions due to spin and possible nonzero electronic orbital angular momentum have so far been neglected. The effect of these interactions is considered in more detail in chapter 4. Here, only a brief introduction is given.

The axial symmetry of diatomic molecules ensures the conservation of electronic angular momentum  $\mathbf{L}$  along the internuclear axis, chosen to correspond to the  $z$ -axis. Therefore, the eigenstates of the Hamiltonian can be characterized by the total electronic spin  $s$ , the absolute projection of electronic angular momentum along the internuclear axis  $\Lambda$  and the eigenvalue of the operator of reflections in the  $XZ$  plane, denoted “+” or “-”. A notation imitating atomic spectroscopic notation is introduced by denoting the electronic state  $^{2s+1}\Lambda^\pm$  with Greek letters  $\Sigma, \Pi, \Delta, \dots$  to represent  $\Lambda = 0, 1, 2, \dots$

Fortunately, the  $^1\Sigma^+$ -state is a common electronic ground state in molecules, and the discussion of molecular structure above remains valid, albeit a non-vanishing electric quadrupole contribution should be taken into account if one or more of the nuclei has spin  $\geq 1$ . Coupling of the remaining angular momenta in the molecules will generally lead to a splitting in energy smaller than 1MHz,

and may therefore be neglected compared to the typical bandwidth of a laser. Molecular ions with the  $^1\Sigma^+$  ground state include  $\text{MgH}^+$  and  $\text{ArH}^+$ , which will be used to illustrate the cooling schemes in the forthcoming chapters, as they are experimentally attractive for a first implementation of the cooling schemes. The choice of these molecular ions will be further justified as the cooling schemes are presented.

In the case of a  $^{2s+1}\Sigma$  ground state with  $s > 0$ , for example encountered in  $\text{CO}^+$ , a perturbation term of the type  $W = \gamma \mathbf{S} \cdot \mathbf{N}$  is present. Splittings of this kind will often be large enough to require special attention when performing optical pumping with lasers, although all substates may still be addressed by using pulsed lasers due to their larger bandwidth. Similarly, the introduction of states with  $\Lambda > 0$  leads to a splitting of the ro-vibrational structure with a magnitude that may vary significantly depending on the molecule.

In chapter 4, molecules in electronic substates different from  $^1\Sigma^+$  are considered further. Again, the reader is referred to reference [53] for a discussion of the finer details of the spectra of diatomic molecules.

### 2.3.2 Selection rules for radiative transitions

The radiative selection rules will be the cornerstone of any optical cooling scheme. In the dipole approximation the transition amplitude is proportional to the matrix elements of the dipole moment  $\langle \Psi_\alpha | \mathbf{D} | \Psi_\beta \rangle$ , which gives the selection rule  $\Delta N = \pm 1$ ,  $\Delta M_N = 0, \pm 1$ , seen from conservation of angular momentum or by direct inspection. In the special case of homonuclear molecules, all pure ro-vibrational transitions will be symmetry forbidden. As a result we will see that only heteronuclear diatomic molecules are amenable for the cooling schemes presented in chapters 3 and 4.

Turning to vibrational transitions, the transition strength will also depend on the dipole matrix element, which may be expanded around  $R_e$ ,

$$I_{\nu,\nu'} \propto \langle f'_{\nu'} | \mathbf{D}(R) | f_\nu \rangle \simeq \langle f'_{\nu'} | \mathbf{D}(R_e) + \left. \frac{d\mathbf{D}}{dR} \right|_{R_e} (R - R_e) | f_\nu \rangle. \quad (2.20)$$

The term involving  $\mathbf{D}(R_e)$  vanishes due to the orthogonality of the vibrational eigenfunctions, and applying the ladder operator technique on the harmonic oscillator eigenstates,  $|f_\nu\rangle$ , the selection rule for vibrational transitions,  $\Delta\nu = \pm 1$ , is found. It should be emphasized that this selection rule is by no means strict since the approximations involved are significant. Hence,  $\Delta\nu \neq \pm 1$ -transitions do occur, but they are typically damped by an order of magnitude or more with respect to the harmonically allowed  $\Delta\nu = \pm 1$  transitions.

### 2.3.3 Polyatomic molecules

Polyatomic molecules will only be considered briefly in this thesis. For the general polyatomic molecule cylindrical symmetry is broken, complicating the analysis. Furthermore, several vibrational and rotational modes will be present,

which implies a much richer ro-vibrational structure. As a result, cooling schemes relying on spontaneous decay and selection rules within the molecule will be hard to apply to polyatomic molecules. The cooling schemes presented in chapters 3 and 4 rely on spontaneous decay within the molecule and are therefore, at best, difficult to apply to polyatomic molecules<sup>1)</sup>. The schemes presented in chapter 6 and 7, on the other hand, do not involve spontaneous decay within the molecules and these schemes are thus more promising to apply to polyatomic molecules.

## 2.4 Stimulated Raman Adiabatic Passage – STIRAP

We now turn to study an elegant technique for population transfer in a  $\Lambda$  type system, i.e. a system with two metastable states,  $|1\rangle$  and  $|3\rangle$ , and one excited state. The excited state,  $|2\rangle$ , may be short lived, while  $|1\rangle$  and  $|3\rangle$  should have longer lifetimes. The goal of the scheme is to transfer population from  $|1\rangle$  to  $|3\rangle$  without loss of population, despite using a short-lived state as intermediate state. The scheme relies on the use of two lasers, a *pump laser* and a *stokes laser*, of which the former is near-resonant with the transition  $|1\rangle \leftrightarrow |2\rangle$  with time-dependent Rabi frequency  $\Omega_p$  and the latter is near-resonant with the transition  $|3\rangle \leftrightarrow |2\rangle$  with time-dependent Rabi frequency  $\Omega_s$ . See figure 2.4 for an overview of the system.

The method of *stimulated Raman adiabatic passage*, STIRAP, will be demonstrated below. In the spirit of the present chapter, the demonstration should provide a basic understanding of the technique, facilitating the application of a modified STIRAP technique to molecular ions in a trap in chapter 7. For a more complete discussion the reader is referred to references [54–56].

The RWA Hamiltonian of the system in the Schrödinger picture is given by

$$H_s = \sum_{n=1}^3 \omega_n |n\rangle \langle n| + \left( \frac{1}{2} \Omega_p e^{-i\omega_p t} |2\rangle \langle 1| + \frac{1}{2} \Omega_s e^{i\omega_s t} |3\rangle \langle 2| + h.c. \right) \quad (2.21)$$

In order to gain more insight, the system should be transformed to an interaction picture. The general method of unitary transformation is outlined below for completeness. For a more complete description the reader is referred to reference sakuraiModernQM.

### Unitary transformations and the interaction picture

Let  $H_s$  be the Hamiltonian of a system in the Schrödinger picture and let  $|\Psi, t\rangle_s$  be a general state ket of the system at time  $t$ . Now, define

$$\begin{aligned} |\Psi, t\rangle_I &= U |\Psi, t\rangle_s \\ O_I &= U O_s U^\dagger, \end{aligned} \quad (2.22)$$

<sup>1)</sup>As an exception to the rule, the schemes are applicable to the special case of linear polyatomic molecules with nonzero permanent dipole moment



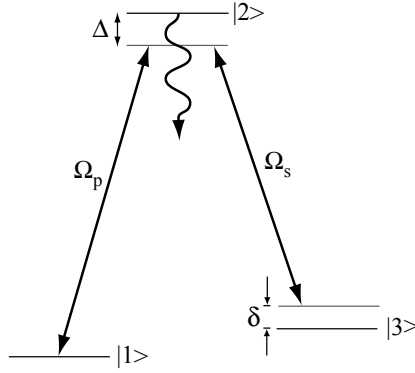


**Figure 2.2:** Schematic representation of the STIRAP process. The system consists of three states  $|1\rangle$ ,  $|2\rangle$  and  $|3\rangle$  of which  $|2\rangle$  decays and the others are metastable. Two lasers are involved in the process. The pump laser is detuned  $\Delta$  from the  $|1\rangle \leftrightarrow |2\rangle$  transition, while the frequency of the stokes laser is chosen, so the detuning from two-photon resonance is  $\delta$ . The Rabi-frequencies of the transitions will be time-dependent, with  $\Omega_s, \Omega_p \rightarrow 0$  for  $t \rightarrow \pm\infty$ . The objective of the process is to effectively transfer population from  $|1\rangle$  to  $|3\rangle$ .

where  $U$  is a unitary operator,  $UU^\dagger = \mathbb{1}$ , and  $O_s$  is an observable in the Schrödinger picture, which is transformed to the interaction picture observable  $O_I$ . It is straightforward to prove that the expectation value of any observable in the interaction picture,  $\langle \Psi |_I O_I | \Psi \rangle_I$ , equals the expectation value of the corresponding observable in the Schrödinger picture,  $\langle \Psi |_s O_s | \Psi \rangle_s$ . It remains to derive the equation of motion for  $|\Psi\rangle_I$ . Applying the Schrödinger equation we find

$$i \frac{\partial}{\partial t} |\Psi\rangle_I = i\hbar \dot{U} |\Psi\rangle_s + U H_s |\Psi\rangle_s = i\dot{U}U^\dagger |\Psi\rangle_I + U H_s U^\dagger |\Psi\rangle_I, \quad (2.23)$$

leading us to define the interaction picture Hamiltonian  $H_I = i\dot{U}U^\dagger + U H_s U^\dagger$ . These maneuvers concludes the general discussion on the unitary transformations. The remaining discussion of the STIRAP process should convince the reader of their relevance.

### 2.4.1 STIRAP in the interaction picture

Define the unitary operator

$$U = \exp \{ i[\omega_1 |1\rangle \langle 1| + (\omega_1 + \omega_p) |2\rangle \langle 2| + (\omega_1 + \omega_p - \omega_s) |3\rangle \langle 3|] t \}. \quad (2.24)$$

The interaction picture Hamiltonian can be found from the definition in section 2.4. Choosing the basis  $\{|1\rangle, |2\rangle, |3\rangle\}$  we find [55]

$$H_I = \hbar \begin{bmatrix} 0 & \frac{1}{2}\Omega_p & 0 \\ \frac{1}{2}\Omega_p & \Delta & \frac{1}{2}\Omega_s \\ 0 & \frac{1}{2}\Omega_s & \delta \end{bmatrix}. \quad (2.25)$$

From equation (2.25) we immediately see that when  $\Omega_s \gg \Omega_p \simeq 0$  there is a zero energy eigenstate of the perturbed system parallel to the unperturbed eigenstate  $|1\rangle$ . Furthermore, for  $\delta = 0$  and  $\Omega_p \gg \Omega_s \simeq 0$  there is a zero energy eigenstate of the perturbed system parallel to  $|3\rangle$ . In the following we shall assume two-photon resonance by letting  $\delta = 0$ . The general eigenstates of  $H_I$  are given by

$$\begin{aligned} |\Phi_+\rangle &= \sin\theta \sin\phi |1\rangle + \cos\phi |2\rangle + \cos\theta \sin\phi |3\rangle \\ |\Phi_0\rangle &= \cos\theta |1\rangle - \sin\theta |3\rangle \\ |\Phi_-\rangle &= \sin\theta \cos\phi |1\rangle - \sin\phi |2\rangle + \cos\theta \cos\phi |3\rangle, \end{aligned} \quad (2.26)$$

where  $\tan\theta = \frac{\Omega_p}{\Omega_s}$  and  $\phi$  is a more complex function of the Rabi frequencies and detunings given in references [56, 57].

The eigenvalues of the perturbed (or *dressed*) atom are given by

$$\begin{aligned} \omega_{\pm} &= \Delta \pm \sqrt{\Delta^2 + \Omega_p^2 + \Omega_s^2} \\ \omega_0 &= 0. \end{aligned} \quad (2.27)$$

Of the dressed atom eigenstates in equation(2.26), the most interesting is  $|\Psi_0\rangle$ . In the limiting cases  $\Omega_s \gg \Omega_p \simeq 0$  and  $\Omega_p \gg \Omega_s \simeq 0$ ,  $|\Psi_0\rangle$  is parallel to  $|1\rangle$  and  $|3\rangle$ , respectively. Furthermore, it has constant eigenvalue  $\omega_0 = 0$  and it is orthogonal to the short-lived bare atom state  $|2\rangle$  regardless of the magnitude of the Rabi frequencies.

We conclude that effective transfer can occur if the laser intensities are chosen so  $\Omega_s \gg \Omega_p \simeq 0$  in the beginning of the transfer, and then swept slow enough to ensure adiabatic evolution of the system<sup>2)</sup> to the situation  $\Omega_p \gg \Omega_s \simeq 0$ . Since  $|\Psi_0\rangle$  is orthogonal to  $|2\rangle$  during the whole process, adiabatic evolution ensures negligible population of the short-lived state  $|2\rangle$  and thus no loss of population due to spontaneous decay. The pulse sequence described here is sometimes denoted *counter-intuitive* for obvious reasons. The mathematics is, however, clear and physically the system can be well understood since the initial presence of  $\Omega_s$  creates dressed states of  $|2\rangle$  and  $|3\rangle$ , allowing the application of a second pulse that transfers  $|1\rangle$  to a dressed state which is orthogonal to  $|2\rangle$ .

<sup>2)</sup>see references [54, 55] for a discussion of the condition for adiabatic evolution

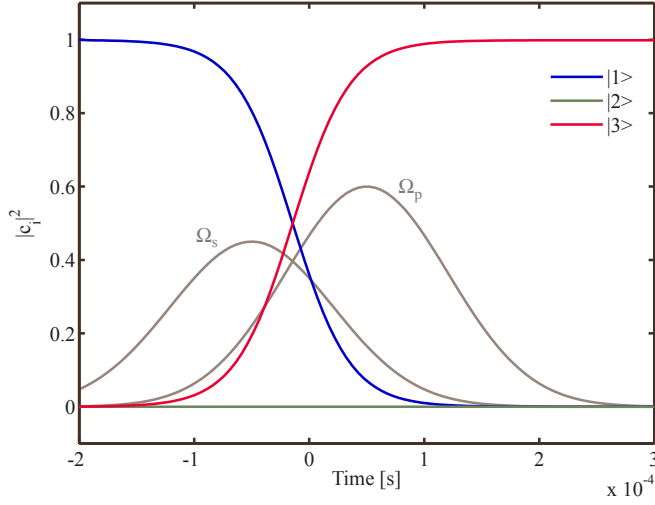


**Figure 2.3:** Numerical simulation of the population evolution during the STIRAP process. The parameters are  $\Omega_s = 30$  MHz,  $\Omega_p = 40$  MHz and  $\Delta = 10$  MHz. To simulate spontaneous decay losses from  $|2\rangle$  an imaginary term of 10 MHz was introduced on the element  $(i, j) = (2, 2)$  in the interaction Hamiltonian of equation (2.25). This decay rate is much faster than  $\Delta t$  and  $\tau$  that were both taken to  $10^{-4}$  s. The conservation of the population shows that no population is scattered on  $|2\rangle$ . The pulse envelopes in arbitrary units are depicted as gray lines.

The pulses are normally chosen to be gaussian in shape, that is

$$\begin{aligned}\Omega_s(t) &= \Omega_s^0 \exp\left[-\left(\frac{t + \Delta t/2}{\tau}\right)^2\right] \\ \Omega_p(t) &= \Omega_p^0 \exp\left[-\left(\frac{t - \Delta t/2}{\tau}\right)^2\right],\end{aligned}\tag{2.28}$$

where  $\Delta t$  is the delay between the pulses and  $\tau$  is the characteristic width of the two pulses. It can be shown, that the optimum choice of pulse delay is  $\Delta t = \tau$  [55]. Furthermore, the conditions for adiabatic following in the STIRAP process with gaussian pulses are [55, 58]

$$\begin{aligned}\sqrt{\Omega_s^2 + \Omega_p^2} \tau &\gg 1 \\ \Omega_s, \Omega_p &\gg \Delta,\end{aligned}\tag{2.29}$$

which implies that adiabatic following can be ensured by increasing the pulse length,  $\tau$ , or the Rabi frequencies  $\Omega_s, \Omega_p$ . The results of numerical simulations of the STIRAP process are given in figure 2.3 and 2.4.

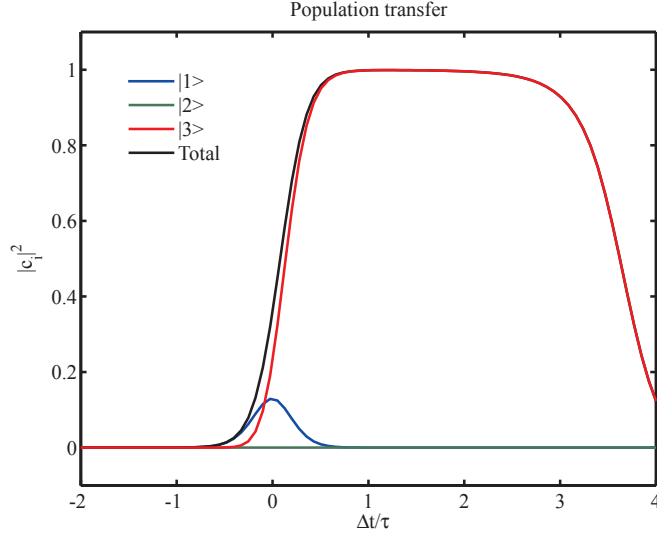


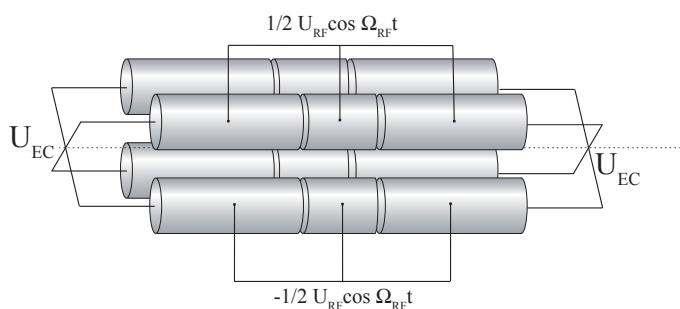
**Figure 2.4:** Numerical simulation of the population distribution after the STIRAP process vs. the pulse delay  $\Delta t$ . The parameters in the simulations are the same as in figure 2.3. In particular, a decay rate of  $10\text{MHz}$  from  $|2\rangle$  is responsible for massive losses from the system unless the condition  $\Delta t \sim \tau$  is fulfilled. The flatness of the transition efficiency peak around  $\Delta t = \tau$  does, however, indicate that the process is quite robust. Robustness with respect to time delay as well as Rabi frequencies is a general feature of STIRAP making it experimentally attractive.

## 2.5 The Linear Paul Trap

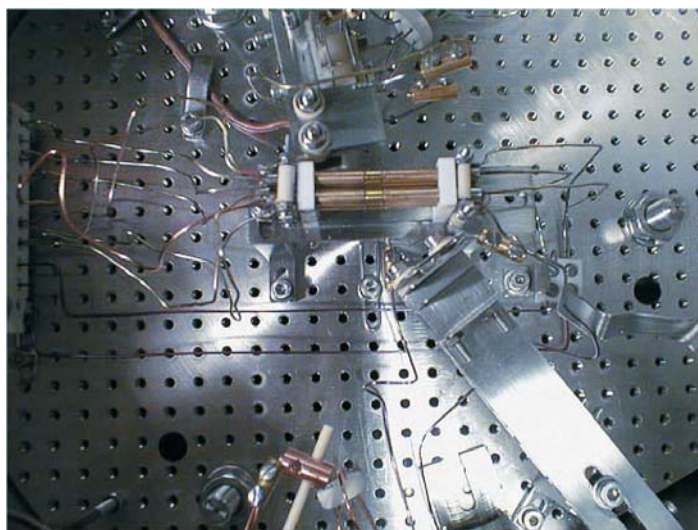
Throughout this thesis a number of experiments with molecular ions in a linear Paul trap will be proposed. We therefore proceed by introducing the trap.

A linear Paul trap [60, 61] is depicted schematically and by a photo in figure 2.5. It consists of four electrodes like its ancestor, the quadrupole mass filter. Radio frequency (rf) voltage is applied in-phase to diagonally opposite electrodes, but with a  $\pi$  phase shift between neighboring electrodes. The rf voltage applied leads to an effective trapping potential in the radial direction. Each of the four trap electrodes are divided into three subsections and a positive dc voltage is applied to the end sections, thus creating axial confinement for charged particles. By appropriate choices of the rf and dc voltages, three dimensional confinement of charged particles can be achieved [62]. The pseudo-potential experienced by a particle with mass  $m$  and charge  $Q$  can be shown to be a three dimensional harmonic oscillator given by

$$U_{\text{pseudo}} = \frac{1}{2}m\omega_r^2 r^2 + \frac{1}{2}m\omega_z^2 z^2, \quad (2.30)$$



(a) Sketch of a Linear Paul trap



(b) Photo of a Linear Paul trap

**Figure 2.5:** (a) Sketch of a linear Paul trap. Radio frequency voltage is applied with diagonally opposite electrodes in phase and neighboring electrodes  $\pi$  out of phase, thus creating radial confinement of charged particles. Positive DC voltage,  $U_{EC}$ , is applied to the end caps to provide axial confinement. (b) Picture of a Linear Paul trap used in the group at the University of Aarhus. The golden rods of the trap is seen at the center of the image. The distance between the screw-holes in the optical table is 10 mm. The sketch in (a) was kindly provided by Anders Mortensen [59]

where the effective radial and axial frequencies,  $\omega_r$  and  $\omega_z$ , are given by

$$\begin{aligned}\omega_z &= 0.5\Omega_{rf}\sqrt{a} \\ \omega_r &= 0.5\Omega_{rf}\sqrt{\frac{1}{2}(q^2 - a)}.\end{aligned}\tag{2.31}$$

Here

$$\begin{aligned} a &= \eta \frac{8QU_{dc}}{m\Omega_{rf}^2 z_0^2} \\ q &= \frac{2QU_{rf}}{m\Omega_{rf}^2 r_0^2} \end{aligned} \tag{2.32}$$

and  $\Omega_{rf}$  denotes the frequency of the rf voltage,  $U_{dc}$  the amplitude of the dc voltage.  $z_0$ ,  $r_0$  and  $\eta$  are parameters relating to the trap dimensions [62, 63].  $r$  denotes the radial coordinate,  $r^2 = x^2 + y^2$  and  $z$  is the axial coordinate. It can be shown that stable orbits for a single ion exist when  $a$  and  $q$  are within a certain stability range [62]. In addition to the effective potential,  $U_{\text{pseudo}}$ , trapped ions are subject to a potential oscillating at frequency  $\Omega_{rf}$ . The amplitude of the resulting micr-motion can, however, be shown to be negligible when  $r$  is small [64].

With a typical dc voltage of 1 V, the linear Paul trap has a potential depth of approximately 1 eV, which is very large compared to, for example, a typical magneto-optical trap [65]. For an in-depth discussion of the linear Paul trap in general, the reader is referred to references [60–62], while the traps used in the group at University of Aarhus are described in more detail in [57, 59, 63, 66]

## 2.6 Laser Cooling

According to Liouville's theorem (See, e.g., [47] for a good discussion), the phase space density of an ensemble cannot be changed if the ensemble is described by Hamilton's equations. Cooling of a system, on the other hand, is characterized by an increase in phase space density. Thus, one should always keep Liouville's theorem in mind as it immediately informs us that any attempt to cool a system without the introduction of a non-Hamiltonian (dissipative) process will be futile. In classical mechanics, an example of a dissipative term is friction, being proportional to the velocity of a particle. In order to cool an ensemble of atoms or molecules it will hence be necessary to introduce a force resembling friction, something which is typically achieved through spontaneous emission cycles.

Another way to reach the same conclusion is by considering entropy. Again, thermodynamics show that an ensemble of particles can only lose entropy, i.e. cool down, if another system (the ensemble of photons in the case of spontaneous emission cycles) gains entropy.

In the previous section we saw that the linear Paul trap establishes a three-dimensional effectively harmonic trapping potential. We may load ions into the trap, but unless cooling is introduced, the ions will not lie still in the trapping potential due to their thermal energy. We now move on to consider Doppler cooling.

Doppler cooling cannot, however, bring the ions to the ground state of the harmonic trapping potential. We will therefore also briefly consider methods

to cool atomic ions below the temperature obtainable with Doppler cooling in section 2.6.2.

### 2.6.1 Doppler cooling

Doppler cooling is, as the name suggests, based on the Doppler effect in the photon absorption probability for a moving ion [67]. We consider the scheme in one dimension for simplicity. The geometry of a cooling experiment is sketched in figure 2.6. Two counterpropagating lasers are detuned to the red of the resonant transition frequency,  $\omega_{ge}$ , of a two-level ion moving with velocity  $v$ . Laser 2, propagating from the positive  $z$ -axis in figure 2.6, will then be shifted closer to resonance in the ions rest frame, due to the Doppler effect. Similarly, laser 1 will be farther from resonance as a result of the Doppler effect. With  $k_i$ ,  $i = 1, 2$  denoting the wave number of the laser propagating from  $z = -\infty$  and from  $z = +\infty$ , respectively (see figure 2.6), the probability of absorbing a photon with momentum vector  $\hbar k_2 \hat{z}$  is higher than the probability of absorbing a photon with momentum vector in the same direction as the ion momentum. Furthermore, the momentum of the spontaneously emitted photons will average to zero after many cooling cycles. The net effect of many absorption-reemission cycles is to brake the ion due to momentum conservation.

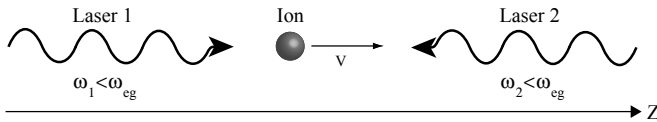


**Figure 2.6:** Geometry in a one-dimensional Doppler cooling experiment. Both lasers are detuned to the red of  $\omega_{ge}$ . The result is larger absorption probability for the photon coming from the left than for the photon coming from the right, due to the Doppler shift in the frame of the moving ion.

We now proceed with a more quantitative description of Doppler cooling. The expression for the line width in equation (2.15) must be modified slightly for a moving ion. As a result we find the following expression for the radiative force on an atom due to a near-resonant light field with wave-vector of magnitude  $k$  and Rabi frequency  $\Omega$  propagating opposite to the atomic motion

$$F_2 = \hbar k \Gamma \frac{\Omega^2/4}{(\Delta - kv_z)^2 + \Omega^2/2 + \Gamma^2/4}, \quad (2.33)$$

where  $v_z$  denotes the velocity of the ion. If the intensity is small, the forces can be summed, which gives the following expression for the combined radiative

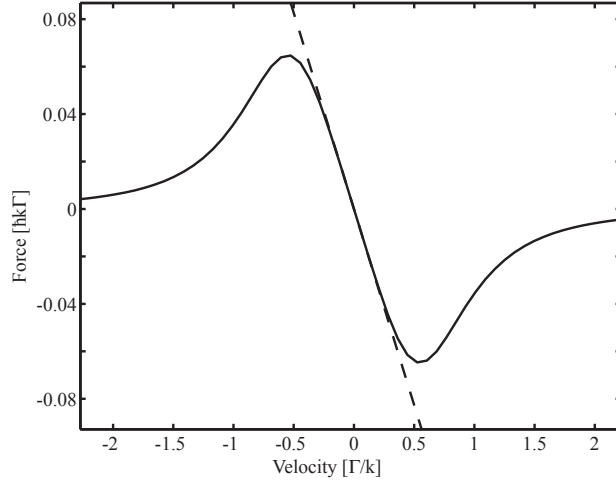


**Figure 2.7:** The total light force on an atom moving in one dimension with two counterpropagating lasers detuned  $-\Gamma/2$  from resonance with a saturation parameter  $s=0.1$ . Solid line depicts the full expression (2.34), while the dashed line depicts the linear approximation at small velocities from equation (2.35).

force

$$F_z = \frac{\Omega^2}{4} \hbar k \Gamma \left[ \frac{1}{(\Delta - kv_z)^2 + \Omega^2/2 + \Gamma^2/4} - \frac{1}{(\Delta + kv_z)^2 + \Omega^2/2 + \Gamma^2/4} \right], \quad (2.34)$$

where  $k = |k_1| = |k_2|$ . The expression can be expanded around  $v_z = 0$  giving

$$F_z = -\alpha v_z + \mathcal{O}(v_z^3), \quad (2.35)$$

with  $\alpha = -2\hbar k_z^2 \frac{s}{(s+1)^2} \frac{\Delta\Gamma}{\Delta^2 + \Gamma^2/4}$ . Equation (2.35) clearly states, that the force is equivalent to friction for  $\alpha > 0$ , i.e. for  $\Delta < 0$ . The basic principle of Doppler cooling is thus established. By setting  $\frac{d\alpha}{d\Delta} = 0$  one finds the detuning maximizing the cooling force  $\Delta = -\Gamma/2$ . Both expression (2.34) and (2.35) at optimal detuning and  $s = 0.1$  are depicted in figure 2.7.

According to equation (2.34), we should be able to cool to zero temperature. However, until now we have neglected recoil in reemission on account of the momentum averaging to zero. Nonetheless, a mean kinetic energy of  $\hbar\omega_r = \frac{\hbar^2 k^2}{2M_{\text{atom}}}$  is transferred to the atom for each spontaneous emission. Here  $M_{\text{atom}}$  denotes the atomic mass. Energy conservation then implies that the absorbed photon has average frequency  $\omega_{\text{abs}} = \omega_{ge} + \omega_r$ . Similarly the spontaneously emitted photon will have average frequency  $\omega_{\text{emit}} = \omega_{ge} - \omega_r$ . In one absorption-reemission cycle, the atom will thus have gained a kinetic energy of  $2\hbar\omega_r$  due to



recoil<sup>3)</sup>. Since two laser beams are involved, we find the average energy transfer to the atoms  $\dot{E}_{\text{recoil}} = 4\hbar\omega_r\gamma$ , where  $\gamma$  was given in equation (2.15). Now, by equating the rate of heating due to recoil and the cooling rate  $\dot{E}_{\text{cool}} = -2\alpha < v_z^2 >$  at the optimal choice of  $\Delta = -\Gamma/2$  we find the *Doppler temperature*,

$$T_D = \frac{\hbar\Gamma}{2k_b}, \quad (2.36)$$

representing the minimum obtainable temperature with Doppler cooling. Here,  $k_b$  denotes Boltzmann's constant.

### Doppler cooling of molecules - failure and explanation

The huge success of Doppler cooling of atoms, where countless applications has appeared, forces one to consider cooling schemes for molecules. The basic spectrum of molecules was considered in section 2.3. Unfortunately it is immediately clear that the large amount of ro-vibrational energy levels in molecules makes it impossible to construct a closed optical pumping cycle, necessary for Doppler cooling, without introducing a vast number of lasers. If one excites an excited electronic state in a molecule, the first step in Doppler cooling, the subsequent spontaneous decay will in general take place to a number of different vibrational states in the electronic ground state, which will then slowly cascade down through the vibrational spectrum through different rotational states. The population will therefore quickly be lost from the cooling cycle, and the molecule will cease to be cooled. The NH radical may, however, be an exception to this rule with a Franck-Condon factor<sup>4)</sup> for the  $A^3\Pi, \nu = 0 \leftrightarrow X^3\Sigma^-, \nu = 0$  transition which is greater than 0.999 [68]. Hence, it has been suggested to use that transition for optical cooling after it has been trapped [18, 69]. But for other molecules, it is impossible to apply the Doppler cooling scheme.

### 2.6.2 Cooling of ions in a trap

In section 2.5 we saw that a linear Paul trap can be used to generate an effective potential minimum for charged particles in free space. If the kinetic energy of trapped ions is much larger than the average Coulomb energy of neighboring ions, the ions will move around in the potential well. If, on the other hand, the Coulomb energy between the ions is dominant, the ions will form a crystal with the inter-ion distances determined by the repulsive Coulomb force between the ions and the confining potential of the trap. More specifically, crystals can be shown to form when the ration of potential to kinetic energy,  $\Gamma_{\text{corr}} = E_{\text{kinetic}}/E_{\text{potential}}$ , exceeds a value of approximately 150 [70]. The finite temperature of the ions is then reflected in vibrations in the crystal lattice,

<sup>3)</sup>The same result can be found from evaluating the momentum spread induced by the spontaneously emitted photons. See [47, page 88] for a further discussion of both approaches.

<sup>4)</sup>The Franck-Condon factors are derived from the overlap of the vibrational states, giving the branching ratios between vibrational states in an electronic transition [48].

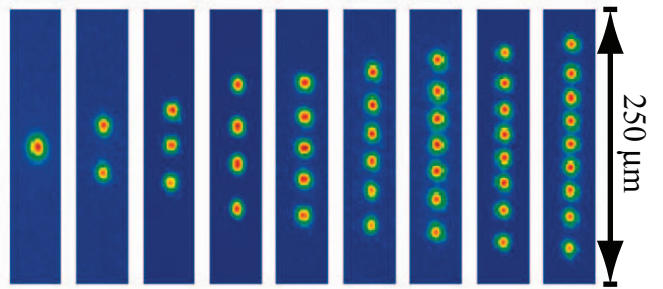


**Figure 2.8:** Strings of laser cooled  $^{40}\text{Ca}^+$  demonstrating high level of control over the loading procedure obtained through resonance-enhanced two-photon ionization.

equivalent to phonons known from solid state physics. Crystalline structure of trapped charged particles can thus be observed with hot, but highly charged particles as first seen as far back as 1959 [71].

If the trapped ions are Doppler cooled as described in section 2.6.1 the ions in the trap are decelerated. A quite substantial number of atomic ions has previously been trapped and cooled in ion traps<sup>5)</sup> and crystalline structures are now produced routinely in ion traps. When the trap is loaded by resonance-enhanced two-photon ionization [73], one can ensure that only one species is loaded into the trap and it is then possible to load the ions at a slow enough rate to allow control of the number of ions in the crystal, as shown in figure 2.8.

In the experimental group in Aarhus, the work has been focused on  $\text{Mg}^+$  and  $\text{Ca}^+$ . Level schemes with the lowest-lying states relevant for cooling is shown in figure 2.9. From the linewidths of the transitions used for Doppler cooling and equation (2.36) we find Doppler temperatures of 1.0 mK and 0.5 mK for  $^{24}\text{Mg}^+$  and  $^{40}\text{Ca}^+$ , respectively. While this is cold enough for crystalline structures to form, it is not enough to cool the ions to the ground state of the harmonic trapping potential<sup>6)</sup>. Thus if ground state cooling is desired, another cooling scheme must be applied.

### Sideband cooling

To reach the motional ground state in a trap it is necessary to apply a cooling mechanism beyond Doppler cooling. If the frequency of the harmonic trapping potential is much greater than the linewidth of an atomic transition, the system

<sup>5)</sup>Atomic ions that have been trapped and laser cooled include  $\text{Be}^+$  [72],  $\text{Mg}^+$  [73],  $\text{Ca}^+$  [73],  $\text{Ba}^+$  [74],  $\text{Hg}^+$  [75, 76] and  $\text{Cd}^+$  [77].

<sup>6)</sup>A temperature of 1 mK corresponds to a Maxwell-Boltzmann distribution peaked around an angular frequency of  $\sim 130$  MHz, which should be compared to the frequency of the harmonic trapping potential which is typically  $\sim 10$  MHz.

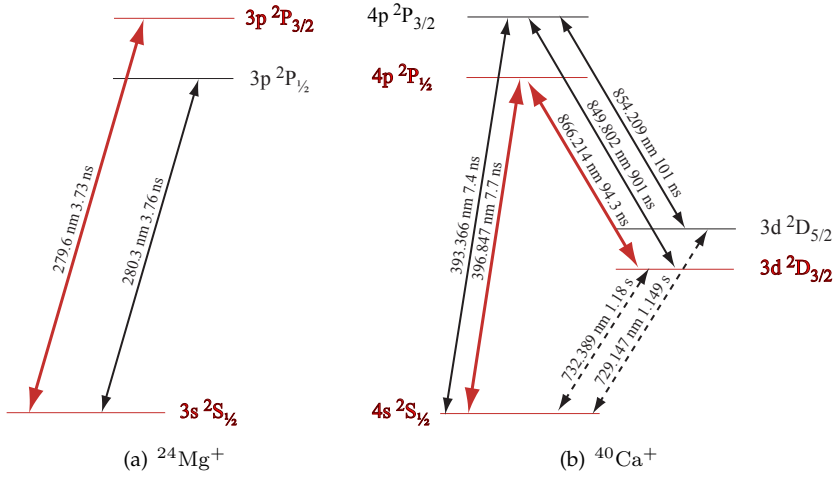


**Figure 2.9:** Levels schemes for  $^{24}\text{Mg}^+$  and  $^{40}\text{Ca}^+$ . The red transitions in the figure are involved in Doppler cooling of the ions. A 866 nm repumping laser is necessary in the  $^{40}\text{Ca}^+$  scheme to avoid loss of population from the  $4s^2S_{1/2} - 4p^2P_{1/2}$  cooling cycle to the metastable  $3d^2D_{3/2}$  state.

is said to be trapped in the *strong binding regime*. In this regime, it is possible to use a scheme called *resolved sideband cooling*, first derived in 1975 [78].

Assume a two level ion trapped in the strong binding regime. The ion states are then dressed by the motional states in the trapping potential, so the state kets can be written  $|g, n\rangle$  for the ground state and  $|e, n\rangle$  for the excited atomic state. Here,  $n$  denotes the number states of the motion of the ions in the harmonic potential. For optical frequencies and typical trapping frequencies, spontaneous transitions will predominantly take place without changing the motional state<sup>7)</sup>. Since the sidebands of vibrational motion in the trap potential are well resolved in the strong binding regime, it is possible to excite a transition from a state  $|g, n\rangle$  to  $|e, n-1\rangle$ . Subsequent spontaneous decay will then bring the population to  $|g, n-1\rangle$ . One excitation and spontaneous emission thus removes a quanta of vibrational motion in the trap potential. After a number of such cooling cycle the system is brought to its ground state  $|g, 0\rangle$ . The cooling scheme is schematically depicted in figure 2.10.

In order to be in the strong binding regime with a Paul trap, it is desirable to use a very narrow transition in the cooling process. For  $^{40}\text{Ca}^+$ , the  $4s^2S_{1/2} - 3d^2D_{5/2}$  transition has been used [79, 80]. A few other ions have been cooled using the sideband cooling scheme, both individually and several ions in a string [81–83].

<sup>7)</sup>A proof of this statement is given in section 5.1.2

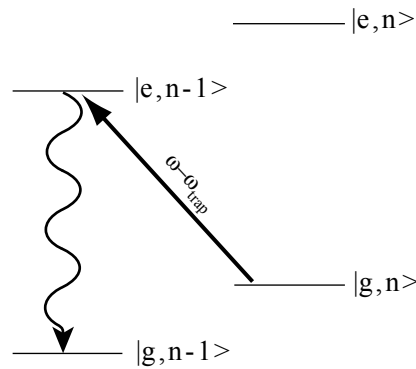


**Figure 2.10:** Sketch of one cooling cycle in the resolved sideband cooling scheme. A transition is driven on the red sideband of the quantized motion in the trapping potential. The transition thus has a resonance frequency  $\omega - \omega_{\text{trap}}$ , where  $\omega$  denotes the resonance frequency of the bare ion and  $\omega_{\text{trap}}$  denotes the frequency of the trapping potential. Subsequent spontaneous emission will predominantly take place on the carrier, ie without changing the motional state in the trapping potential. Each cooling cycle then removes one quantum of vibrational excitation from the system. Through the passage of several cooling cycles it is possible to cool the ions to the ground state of the harmonic trapping potential.

### 2.6.3 Sympathetic cooling of ions

The transfer of momentum between charged particles in a trap is very effective due to the strength of the Coulomb interaction. As a result it is possible to cool ions indirectly by loading them into a trap together with laser cooled ions, since momentum will be transferred from the unperturbed ions to the ions that are laser cooled. The momentum will then be removed from the laser cooled species by the laser fields as described in the previous section and thereby cooling of both species is achieved. The method is attractive since it is independent of the structure of the sympathetically cooled ions, albeit the charge-to-mass ratios of the ions need to be similar for effective sympathetic cooling. A number of experimental demonstrations of sympathetic cooling to low temperatures in Paul and Penning traps exist [84–87]. Sympathetic cooling to the motional ground state in the trap through sideband cooling has also been demonstrated [72, 88].

#### Sympathetic cooling of the translational temperature of molecular ions

Since sympathetic cooling is independent of the structure of the sympathetically cooled ions, it is possible to cool molecular ions by loading them into a trap with laser cooled atomic ions. Experiments have shown that more than 1000  $\text{MgH}^+$  ions can be sympathetically cooled to temperatures low enough to form

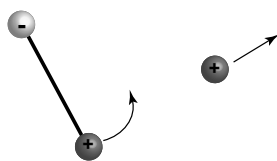


**Figure 2.11:** Simplified and, as it turns out, wrong view of sympathetic cooling of internal degrees of freedom in molecular ions. By modeling the molecular ion as a classical rotating dipole, one should expect that the rotations of the dipole to induce a vibrational motion in a nearby atomic ion due to the Coulomb interaction. From a more thorough consideration, however, it can be understood why this mechanism does not lead to cooling of the rotations.

Coulomb crystals by just 50 laser cooled  $\text{Mg}^+$  ions, demonstrating the strength of the sympathetic cooling [38]. A number of other molecular ions have been cooled sympathetically [39, 89].

### Sympathetic cooling of the ro-vibrational temperature of molecular ions

With relatively simple and very effective cooling of the translational degrees of freedom of molecular ions in a trap well proven, it is natural to turn to the internal degrees of freedom of molecules. From a simple classical consideration, one might think that sympathetic cooling should also work for the rotations and vibrations of a molecular ion in a trap.

If the molecular ion is modeled as a rotating and vibrating classical dipole, next to a cooled atomic ion, one should expect the vibration and rotation to induce motion in the atomic ion as depicted schematically in figure 2.11. Since the atomic ion is cooled continuously, energy should then be removed from the entire system.

From section 2.3 we know that the rotations and vibrations in molecules have frequencies in the range  $10^{11} - 10^{14}$  Hz, while the typical frequency of the harmonic trapping potential is 10 MHz or less. Hence, transfer of energy between these degrees of freedom cannot happen in a low-order process. From this consideration we do not expect the internal and external degrees of freedom to interact and they should therefore not be expected to have the same temperature. It is thus expected, that the internal degrees of freedom of the molecules relax to equilibrium with BBR at  $\sim 300$  K.

In order to establish the internal temperature of sympathetically cooled molecular ions with greater confidence than a simple estimate can provide, it is necessary to obtain experimental data. The resulting rotational temperature of  $\text{MgH}^+$  when subject to a speculative sympathetic cooling  $\dot{\bar{E}}_{\text{rot}} = -\Gamma_c \bar{E}_{\text{rot}}$  is depicted in figure 2.12. Here we used  $\bar{E}_{\text{rot}}$  to denote average rotational energy. It is immediately seen, that even inefficient coupling between internal and external degrees of freedom may lead to a considerably changed population of

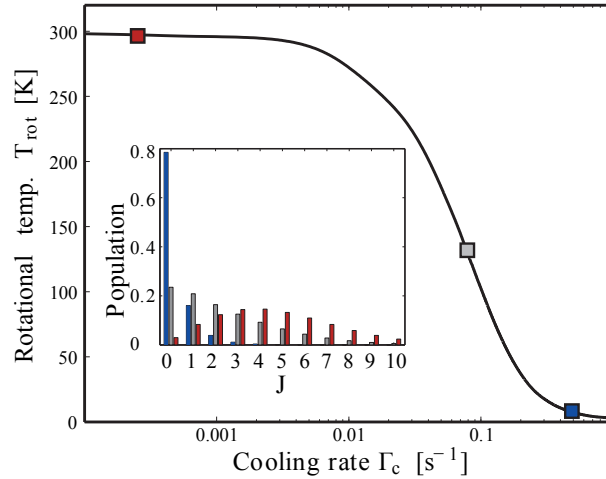


**Figure 2.12:** Steady state rotational temperature,  $T_{\text{rot}}$  of  $\text{MgH}^+$  as function of the effective cooling rate  $\Gamma_c$ . The insert shows the population distribution for three different temperatures, marked on the graph. Red:  $T_{\text{rot}} = 300$  K, Grey:  $T_{\text{rot}} = 120$  K, Blue:  $T_{\text{rot}} = 7$  K. Reproduced from [41].

the rotational energy levels. This can be understood from the long time scale necessary for the molecular ions to relax to equilibrium with BBR ( $\sim 5$  s).

The Aarhus group performed measurements of the rotational temperature of  $\text{MgH}^+$  sympathetically cooled by  $\text{Mg}^+$  [41, 42, 90]. The measurements were done using Resonance-Enhanced Multi-photon Photo-Dissociation (REMPD) [91]. The molecular ions going through REMPD dissociate to neutral  $\text{Mg}^+$  and a proton. The trap is not stable for protons, so ions going through REMPD are lost from the trap, and the rate of REMPD can thus be derived from the rate of loss of ions from the trap. Figure 2.13 shows a pure  $\text{Mg}^+$  crystal, a mixed  $\text{MgH}^+$  and  $\text{Mg}^+$  crystal and the resulting pure  $\text{Mg}^+$  crystal when  $\text{MgH}^+$  has been dissociated from the mixed crystal.

REMPD was made with a Nd:YAG laser delivering  $\sim 5$  ns pulses resonant with a given transition  $R(J) = |\nu = 0, J\rangle_X \rightarrow |\nu = 0, J + 1\rangle_A$ . Here  $\nu$  and  $J$  are the vibrational and rotational quantum numbers, while subscripts  $X$  and  $A$  refers to the  $X^1\Sigma$  and  $A^1\Sigma$  electronic states of  $\text{MgH}^+$ , respectively. From the  $A^1\Sigma$  electronic state the molecular ion can either decay to the ground electronic state or proceed to the dissociating state,  $C^1\Sigma$ , through the absorption of a second photon from the laser field. Molecules undergoing dissociation are detected indirectly as the ions are lost from the trap. Numerical simulations have shown that the ratio of dissociation rates when the laser is resonant with the R(1) and R(6) transitions are highly sensitive to the rotational temperature of the molecule as indicated in figure 2.14. In the experiment these dissociation rates were therefore measured and the range of the ratio which is in accordance with

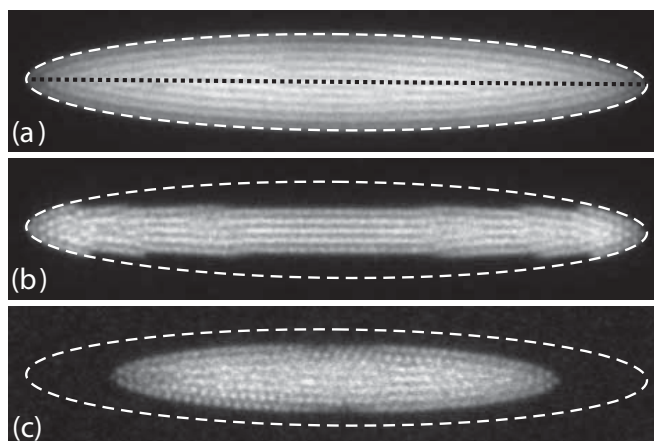


**Figure 2.13:** (a) 2D projection-image of a pure Coulomb crystal of  $\text{Mg}^+$  ions. (b) A two-component crystal ( $\sim 35\% \text{Mg}^+$  and  $\sim 65\%$ ) obtained by letting the  $\text{Mg}^+$  ions in the crystal (a) react with  $\text{H}_2$ . (c) A nearly pure  $\text{Mg}^+$  crystal obtained by applying the ns laser pulses for 60 s to dissociate the  $\text{MgH}^+$  molecules in (b). The dotted line in (a) shows the axis of rotational symmetry, while the dashed ellipses show the outer surface of the original crystal from (a). Reproduced from [41]

these experiments are presented on figure 2.14. By comparing the numerically simulated dissociation rates as function of temperature with the experimentally measured ratio, one finds that the ions are internally warmer than 120 K and probably somewhat higher, i.e. around BBR equilibrium. It can thus be concluded that there is not effective sympathetic cooling of the rotational energy of  $\text{MgH}^+$  in a trap. Since  $\text{MgH}^+$  has a representative dipole moment and rotational frequencies, it is expected that other sympathetically cooled molecular ion species should be internally hot. This is in accordance with results from storage ring experiments [92].

In conclusion we have established that molecular ions in a trap with laser cooled atomic ions undergo very effective sympathetic cooling of the translational degrees of freedom, thus becoming immobile in Coulomb crystals. The internal degrees of freedom are, however, not susceptible to sympathetic cooling in a trap, and the molecular rotations therefore relax to equilibrium with the temperature of the environment.

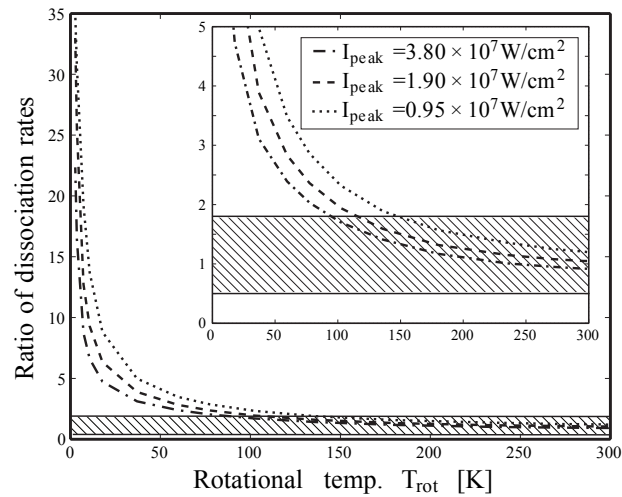


**Figure 2.14:** The ratios between the simulated dissociation rates for REMPD processes via the R(1) and R(6) resonances.  $T_{\text{rot}}$  is connected to a speculative sympathetic cooling rate as illustrated in figure 2.12. The three curves represent simulated ratios for different laser intensities at a given  $T_{\text{rot}}$ , whereas the hatched area represent a conservative estimate of the range which is in agreement with the experimentally measured dissociation rates. Reproduced from [41]



## CHAPTER 3

# Blackbody-Radiation-Assisted Laser Cooling of Molecular Ions

In chapter 2 we set the stage for laser cooling of molecular ions. In section 2.6.3, we saw that molecular ions can be sympathetically cooled when loaded into a trap with laser cooled atomic ions and Coulomb crystallization of the two-component ensembles of molecular and atomic ions was verified. With Coulomb crystals forming when the translational temperature is decreased below  $T < 100$  mK we have thus verified experimental means of preparing targets with translationally cold and spatially localized molecular ions. Furthermore, the significant depth of a typical Paul trap combined with a typical background gas pressure around  $10^{-10}$  Torr ensures that the ions can be trapped for hours or even days. The average interval between inelastic collisions with the background gas at the relevant pressure can furthermore be estimated to several minutes from Langevin theory [93]. We did, however, also see that the internal temperature of the molecular ions remain hot throughout sympathetic cooling of the translational degrees of freedom. This was originally a theoretical expectation resulting from an energy consideration, but it has recently been verified experimentally (see section 2.6.3 and [41]). Since state specific targets are desired, we consider schemes for cooling the ro-vibrational degrees of freedom in molecular ions.

The long trapping times of the ions, combined with long intervals between collisions opens for internal cooling schemes which *rely on* rather than being hampered by blackbody-radiation (BBR), and which are efficient on the timescale of seconds or tens of seconds.

We proceed by first considering the simplest molecular ions, diatomic molecules in the  $^1\Sigma$  electronic ground state, postponing the discussion of more complex molecules to the subsequent chapter. The cooling schemes presented in this and the next chapter have been published in three articles, references [94–96].

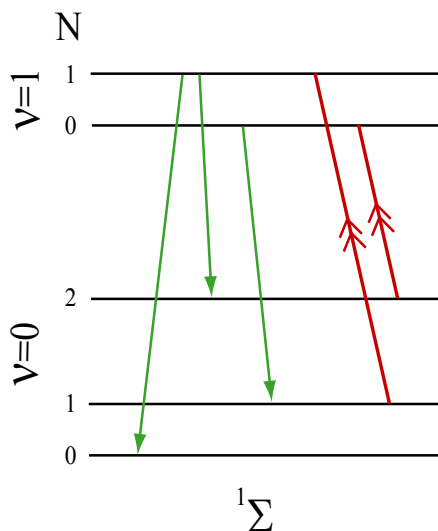


**Figure 3.1:** The lowest rotational states of the two lowest vibrational bands of a diatomic molecule and the transitions needed for the Raman cooling scheme. Red double arrows indicate a Raman type transition via an excited electronic state of the molecular ion, while green arrows denote the subsequent spontaneous decay paths.  $N$  and  $\nu$  denote the rotational and vibrational quantum number, respectively. A detailed explanation of the cooling principle is given in the text.

### 3.1 Cooling Concept

We consider a cooling scheme for the internal degrees of freedom of smaller diatomic molecular ions with  $^1\Sigma$  electronic ground state. At room temperature the vibrational degree of freedom is frozen out for all the lighter species, i.e., the vibrational quantum number is equal to  $\nu = 0$ . It is thus sufficient to establish rotational cooling.

Our concept involves the following processes: Pumping of population from “pump states” ( $\nu = 0, N = 1$ ), and ( $\nu = 0, N = 2$ ), where  $N$  denotes the rotational quantum number, into specific excited ro-vibrational states from which subsequent spontaneous emission brings population back into either one of the “pump states”, or into the ground state ( $\nu = 0, N = 0$ ). The latter is referred to as a “dark state”, since it is not effected by the pumping fields. Finally, BBR is responsible for the feeding of the “pump states” with populations from states with  $N > 2$ . In figure 3.1, a sketch of the cooling concept, realized by utilizing two resonant, dipole allowed Raman transitions ( $\Delta N = 0, \pm 2$ ), is presented. In the absence of BBR any initial population in rotational states with  $N = 1$ , and  $N = 2$  would within a certain time be optically pumped into the “dark state”

( $\nu = 0, N = 0$ ) due to the selection rules  $\Delta N = \pm 1$  for spontaneous emission. In the presence of BBR, effective cooling into the internal ground state is possible from an initial thermal distribution with significant population in states with  $N > 2$  provided the rate of optical pumping and spontaneous emission from the vibrationally excited state are both higher than the redistribution rate among the rotational states due to BBR. The cooling time will in such cases be set by the inverse of the typical rotational redistribution rate.

In an experiment, the Raman transitions will be driven by pulsed lasers. In that case, high population transfer is assured if each Raman pulse saturates its transition. This means the pulse time,  $\tau$ , times the Raman coupling frequency,  $\Omega_R$ , should fulfill (i)  $\tau\Omega_R \gtrsim 10$ , where  $\Omega_R \simeq \Omega^2/\Delta$  with  $\Omega$  being the typical Rabi frequency of the dipole allowed electronic transitions and  $\Delta$  the corresponding detuning<sup>1</sup>. Furthermore, a small incoherent scattering rate is required, leading to (ii)  $\tau\Gamma_{\text{scat}} \lesssim 0.01$ , with  $\Gamma_{\text{scat}} \simeq \Omega_R A/\Delta$ ,  $A$  being the pertaining Einstein coefficient<sup>2</sup>.

## 3.2 Numerical Simulations

In this section, we present a model of the cooling scheme and present details of the numerical simulations. We also derive some fundamental properties of the molecule  $\text{MgH}^+$ , which we will use as our favorite guinea-pig for numerical simulations. We have chosen  $\text{MgH}^+$  because the production and translational cooling of  $\text{MgH}^+$  in a Paul trap has already been established [38], thus making it an attractive candidate for first experimental implementation of the ro-vibrational cooling schemes. The results of the numerical simulations of  $\text{MgH}^+$  are presented in section 3.2.4.

### 3.2.1 Rate equations for the population dynamics

The population dynamics is well-described by rate equations giving the change in population of a given state via Einstein coefficients and frequency-specific radiation intensities. The equation of motion for the molecular population in

---

<sup>1</sup>These estimates are readily derived from the second order term in time-dependent perturbation theory (Dyson series) [44] when  $\Delta$  is large compared to the linewidth of the excited state.

<sup>2</sup>The estimate of the incoherent scattering rate is the amplitude of the Rabi oscillations at detuning  $\Delta$ , c.f. section 2.2, times the decay rate from the excited state,  $A$

state  $i$ ,  $P_i$ , takes the form

$$\begin{aligned} \frac{dP_i}{dt} = & - \sum_{j=0}^{i-1} A_{ij} P_i + \sum_{j=i+1}^M A_{ji} P_j - \\ & \sum_{j=0}^{i-1} P_i B_{ij} W(\omega_{ij}) + \sum_{j=0}^{i-1} P_j B_{ji} W(\omega_{ij}) - \\ & \sum_{j=i+1}^M P_i B_{ij} W(\omega_{ij}) + \sum_{j=i+1}^M P_j B_{ji} W(\omega_{ij}). \end{aligned} \quad (3.1)$$

Here

$$\begin{aligned} \mathbf{P} = & (P_{\nu=0, N=0}, P_{\nu=0, N=2} \dots P_{\nu=0, N=N_{max}}, P_{\nu=1, N=0} \\ & \dots P_{\nu=1, N=N_{max}}, P_{\nu=2, N=0} \dots P_{\nu=2, N=N_{max}}) \end{aligned} \quad (3.2)$$

represents the populations in vector form with  $N_{max}$  chosen so the population in higher-lying rotational states is negligible during the cooling process. In equation (3.1),  $M$  denotes the last element in  $\mathbf{P}$ .  $A_{ij}$  and  $B_{ij}$  are the Einstein coefficients describing spontaneous and stimulated transitions from energy level  $i$  to  $j$ .  $W(\omega_{ij})$  is the cycle averaged radiative energy density present in the trap at the resonant transition frequency,  $\omega = \omega_{ij}$ , between level  $i$  and  $j$ . In equation (3.1), the first term corresponds to spontaneous decay from state  $i$  to states with lower energy, while the second term describes spontaneous decay from levels with higher energy into state  $i$ . Stimulated emission from the  $i$ th state and stimulated absorption from lower-lying states is then described by the third and fourth term, and finally, the last two terms represent transitions due to absorption of radiation from the  $i$ th state and stimulated emission from higher-lying states into the  $i$ th state.

The system of equations (3.1) is conveniently expressed by the matrix equation

$$\frac{d\mathbf{P}}{dt} = \mathbf{K}\mathbf{P}, \quad (3.3)$$

where  $\mathbf{K}$  is an  $(M + 1) \times (M + 1)$  coupling matrix.

### 3.2.2 Calculation of molecular properties

As seen from equation (3.1), it is necessary to know the Einstein coefficients to simulate the population dynamics. For many molecules, the Einstein coefficients are available in the literature. If not, they are evaluated numerically as follows. We use the well-known quantum mechanical expressions for the Einstein coefficients between an upper state  $\Psi_n$  and a lower state  $\Psi_m$  that are both

non-degenerate [97]

$$\begin{aligned} B_{n,m} &= \frac{\pi |\mathbf{D}_{n,m}|^2}{3\epsilon_0 \hbar^2}, \\ A_{n,m} &= \frac{\hbar \omega^3}{\pi^2 c^3} B_{n,m}, \end{aligned} \quad (3.4)$$

where  $\omega$  denotes the transition frequency and  $\mathbf{D}$  the transition dipole moment between the states.

$$\mathbf{D}_{n,m}^{lab} = \int \Psi_n^* \mathbf{M}^{lab} \Psi_m d\tau, \quad (3.5)$$

with  $d\tau$  denoting the volume element corresponding to integration over the complete set of coordinates for all particles involved and

$$\mathbf{M}^{lab} = \sum_k -e\mathbf{r}_k + \sum_{l=1,2} Z_l e \mathbf{R}_l \quad (3.6)$$

the dipole operator.

The equations refer to a laboratory-fixed coordinate system so the molecular wave-functions include the rotational terms. The summation indices,  $k$  and  $l$ , in equation (3.6) refer to the electrons and the involved nuclei, while  $Z_l$  denotes the nuclear charge.

For degenerate states, equation (3.4) is modified to

$$\begin{aligned} B_{n,m} &= \frac{\pi |\mathcal{D}_{n,m}|^2}{3g_n \epsilon_0 \hbar^2} \\ A_{n,m} &= \frac{\hbar \omega^3}{\pi^2 c^3} B_{n,m}, \end{aligned} \quad (3.7)$$

where  $g_n$  is the degeneracy of the upper state. The derivation of the dipole matrix elements connecting ro-vibrational levels,  $\mathcal{D}_{n,m}$  is given in appendix B.

$$|\mathcal{D}_{m,n}|^2 = S_{J_m, J_n} \left| \int f_{\nu_n}(R) D_e(R) f_{\nu_m}(R) R^2 dR \right|^2. \quad (3.8)$$

The Hönl-London factors,  $S_{J_m, J_n}$ , are tabulated in the literature [51, 98–100] and may be evaluated by the expressions given in Appendix A. Both the potential energy curve for the molecule and the electronic dipole moment function,  $\mathbf{D}_e^{mol}(R)$ , is evaluated with *Gaussian* [101]. The ro-vibrational eigenfunctions,  $f_{\nu_n}$ , are readily found from the potential energy curve using the Numerov method. Knowing  $f_{\nu_n}$ , the one-dimensional integral of equation (3.8) can be evaluated. We use the *Level 7.5* program [102] to perform these tasks and to evaluate equation (3.7), leaving us with the desired Einstein coefficients.

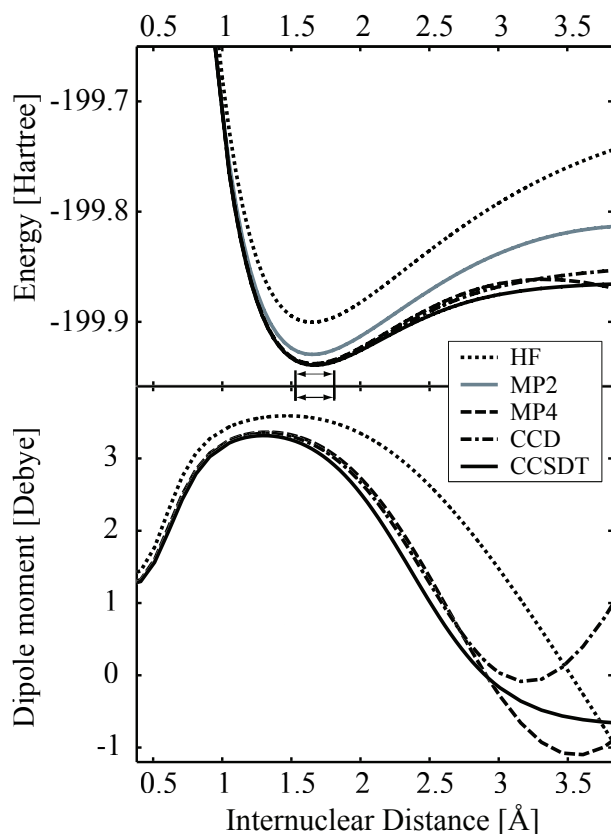


**Figure 3.2:** Top: Born-Oppenheimer electronic potential energy curves of  $\text{MgH}^+$  ( $X^1\Sigma$ ) calculated by *Gaussian* in a 6-311++G basis set [103] using Hartree-Fock (HF) theory, Møller-Plesset  $n$ th order perturbation theory (MPn), coupled cluster theories with single and double excitations (CCD), and single, double and triple excitations (CCSDT). See references [104–108] for descriptions of the methods. The curves for the MP4, CCD and CCSDT calculations are in good agreement close to the equilibrium position,  $1.65 \text{ \AA}$ , indicating that these methods give an accurate description of the problem. Bottom: Corresponding dipole moment functions,  $D_e^{mol}(R)$  of equation (B.3) pointed along the internuclear axis, of  $\text{MgH}^+$  calculated with *Gaussian*. The MPn and coupled cluster theories largely agree around the equilibrium distance, although not as well as for the potential curve due to the dependence on electronic wave functions rather than eigenenergies. The classical turning points for the vibrational ground state are marked on the common abscissa at  $1.5$  and  $1.8 \text{ \AA}$ . The result of the MP2 calculation cannot be discriminated from the MP4 result at the internuclear distances of interest.

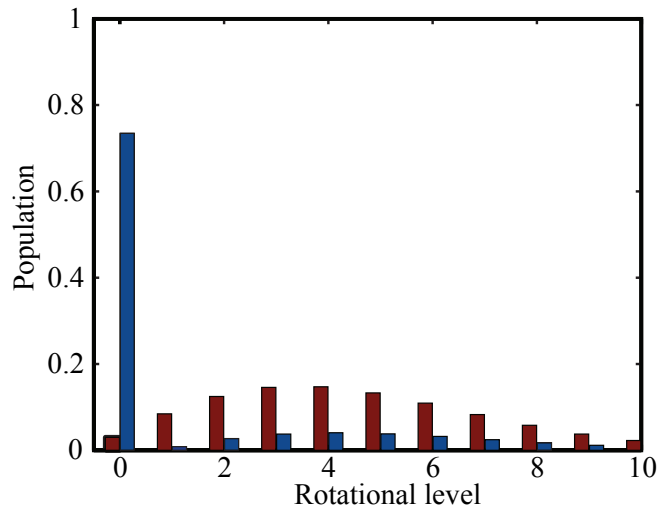
### Einstein coefficients for $\text{MgH}^+$

Since translational cold samples of  $\text{MgH}^+$  have been produced in a trap loaded with laser cooled  $\text{Mg}^+$  atomic ions, cf. section 2.6.3 and [38], this molecular ion is the first choice for an implementation of the presented cooling scheme. To our knowledge, only a few Einstein coefficients for transitions within the electronic ground state have been published [94]. We have re-calculated the coefficients using the approach of the previous section. The potential curves obtained from *Gaussian* [101] using various theoretical approaches on a 6-311++G basis set [103] is given in figure 3.2 together with the corresponding dipole moment functions in the molecular center of mass system. The potential curves show convincing convergence and our derived vibrational transition frequencies and equilibrium distance agree with published data within 1.5% [51]. To compute the accurate electronic dipole moment function is more challenging, since this requires accurate electronic wave functions. Generally the Møller-Plesset fourth-order perturbation theory [107] and the coupled-cluster theories [108] are reliable for the task. The dipole moment functions converge to a unique function as the level of approximation is refined, as shown in figure 3.2, indicating that the highest order CCSDT function is a good approximation to the physical dipole moment function. Furthermore, we have performed equivalent calculations on the isoelectronic molecules  $\text{NaH}$  and  $\text{BeH}^+$  [109–111] to compare our results with other published calculations. The results were in agreement within 5%, a level which is not critical for the simulations of the cooling schemes. The calculated Einstein coefficients are given in appendix A.

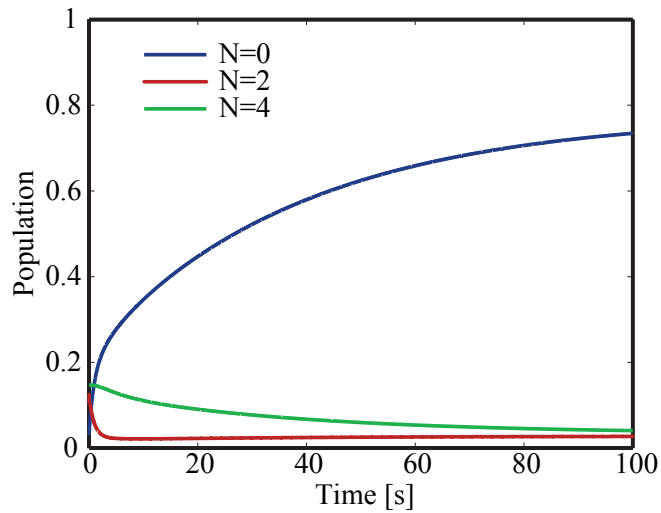
We have now set up the model and acquired the parameters entering the coupling matrix  $\mathbf{K}$  in equation (3.3) and the solution can now be found numerically using standard methods as described below.

### 3.2.3 Solving the population dynamics

We model the dynamics of the cooling on the test case of  $\text{MgH}^+$  by solving equation (3.3) [112]. In the population vector,  $\mathbf{P}$ , of equation (3.2) we use  $N_{max} = 20$  since the population of this and higher-lying levels is effectively zero during the cooling process. The radiation density  $W(\omega)$  at resonance between levels not addressed by lasers has been calculated from a Boltzmann distribution at 300 K. The pulsed lasers are included by saturating the pumped transitions, described in section 3.1, at a repetition rate of 100 Hz. In the simulation, this is done by redistributing the population in the involved ro-vibrational levels at the given repetition rate according to the degeneracy of the levels. All simulations are made with populations which are initially Boltzmann distributed at a temperature of 300 K. All simulations in both this and the following chapter are made with the most abundant isotopes, in this case  $^{24}\text{Mg}^1\text{H}^+$  (79% abundance).



(a) Rotational distribution of MgH<sup>+</sup> before and after cooling



(b) Evolution of the population in selected rotational states during cooling

**Figure 3.3:** (a) Cooling of MgH<sup>+</sup> by the Raman scheme (see figure 3.1). The red columns represent the initial rotational populations corresponding to a thermal distribution at  $T = 300$  K. The blue columns represent the population distribution after 100 s of cooling. See the text for details on the cooling parameters. (b) Evolution of the populations of the rotational levels with quantum numbers  $N = 0, 2, 4$  as a function of cooling time for MgH<sup>+</sup>.



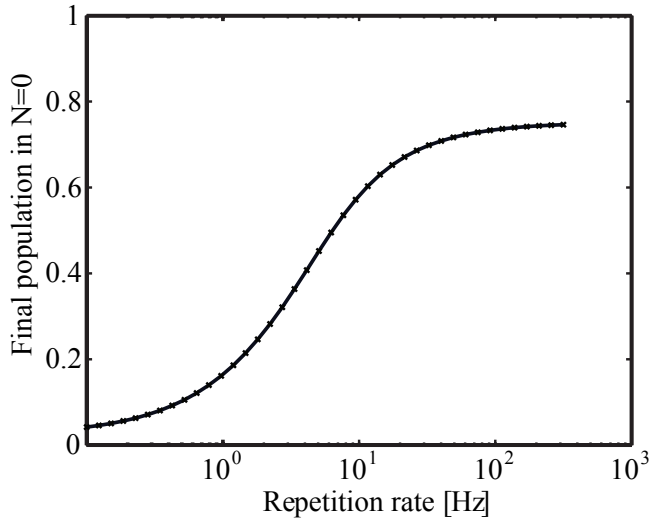


**Figure 3.4:** Population in the ro-vibrational ground state of  $\text{MgH}^+$  after 100 s of cooling as a function of the repetition rate of the pumping lasers. Each laser pulse saturates the transition it pumps.

### 3.2.4 Numerical results

We now turn to present the results of the numerical simulations. In figure 3.3, the simulated rotational distribution of  $\text{MgH}^+$  subject to the cooling scheme of section 3.1 is presented. The red columns represent the initial rotational populations, while the blue columns show the populations after 100 seconds of cooling. In the simulation, Raman pulses couple the vibrational states of the  $X^1\Sigma^+$  potential curve via the electronically excited  $A^1\Sigma^+$  state, using lasers in the wavelength range  $\sim 279$  nm [51]. Using  $A = 10^8$  Hz for the electronic transition and  $\Delta = 10^{11}$  Hz to the red, we find that the saturation and scattering conditions (i) and (ii), discussed in section 3.1, can be fulfilled for the pumped transitions from any rotational sub-state with 10 ns pulses with intensities  $\sim 100$  kW/cm<sup>2</sup>. The repetition rate of the Raman pulses was 100 Hz, which is much higher than the typical rate for rotational transitions due to BBR. The figure shows that more than 70% of the population can be accumulated in the ro-vibrational ground state which is equivalent to the ground state population of a thermal distribution at 8.5 K.

Figure 3.3(b) shows the evolution of the population in three representative rotational levels of  $\text{MgH}^+$  for the Raman scheme discussed above. After 100 s of cooling the system has practically reached steady-state.

Figure 3.4 explores the sensitivity of the cooling efficiency for  $\text{MgH}^+$  on the repetition rate of the Raman pulses for a fixed cooling time of 100 s. Already

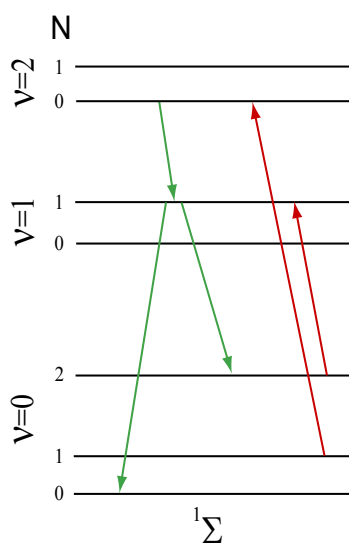


**Figure 3.5:** A variation of the cooling scheme of figure 3.1. Rather than using two-photon transitions via an excited state, this version of the cooling concept is based on two direct vibrational excitations with lasers in the infrared range. One laser couples  $(\nu = 0, N = 1) \leftrightarrow (\nu = 2, N = 0)$ , while the other couples  $(\nu = 0, N = 2) \leftrightarrow (\nu = 1, N = 1)$ . Green arrows depict the subsequent dipole allowed spontaneous decay paths.

for modest repetition rates, say 20–30 Hz, we observe a significant cooling efficiency and repetition rates larger than 100 Hz do not significantly increase the cooling efficiency. This is experimentally very encouraging since laser systems with nanosecond pulses typically have repetition rates in the interval 10 – 100 Hz.

### 3.3 Direct Two-Laser Scheme

The Raman scheme discussed in the previous sections is effective for molecular ions which have an excited electronic state that can be addressed by laser light in the visual or near-visual range. If such excited states are absent, a scheme based on continuous wave near infra-red (IR) sources introducing direct couplings *within* the ground electronic potential curve can be applied. This direct scheme works as follows: One IR source couples  $(\nu = 0, N = 1) \leftrightarrow (\nu = 2, N = 0)$  which, although forbidden in the harmonic approximation of section 2.3.2, is easily saturated due to the anharmonicity of the potential curve of typical molecules. The excited  $(\nu = 2, N = 0)$  cascades down by dipole allowed transitions,

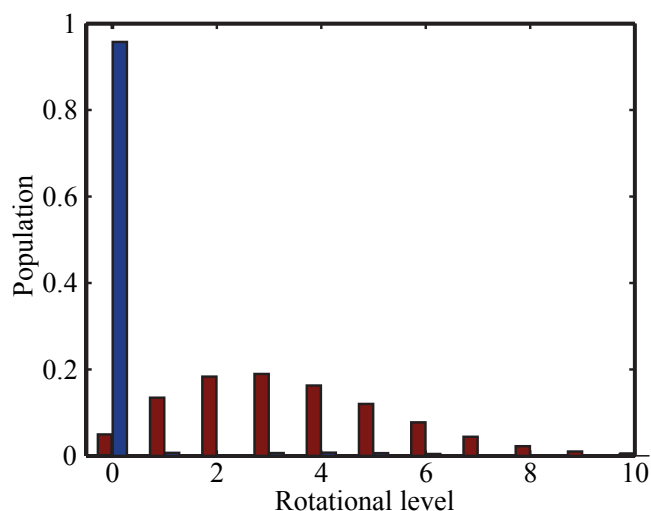


**Figure 3.6:** Cooling of  $\text{ArH}^+$  by the direct scheme. The red columns represent the initial rotational populations corresponding to a thermal distribution at  $T = 300$  K. The blue columns represent the population distribution after 50 s of cooling. See the text for details on the scheme, and the cooling parameters.

first to the  $(\nu = 1, N = 1)$  excited state and then to the  $(\nu = 0, N = 0)$  dark state or the  $(\nu = 0, N = 2)$  state. The latter state is pumped by another laser into the  $(\nu = 1, N = 1)$  state, from which decay into the dark state or back into the  $(\nu = 0, N = 2)$  state will take place.

### Numerical simulations

As an example of the application of this direct scheme we consider  $\text{ArH}^+$  which is supposed to have no stable excited electronic states [113]. Numerical simulations were performed with the approach detailed in section 3.2, but including the  $(\nu = 2, N = 0 \dots 2)$  levels in the simulations. Figure 3.6 shows the initial thermal ( $T = 300$  K) distribution over rotational states for  $\text{ArH}^+$  and the final steady-state distribution after 50 s of cooling. In the cooled distribution, more than 95% of the population is in the  $X^1\Sigma^+$  ro-vibrational ground state, equivalent to the ground state population of a thermal distribution at a temperature of 7 K.  $\text{ArH}^+$  is a strong vibrational infrared emitter [114, 115], and the rotational transition rates are of the same order of magnitude as in  $\text{MgH}^+$  [116] and, consequently, the cooling is very effective. The IR stimulated processes which drives the  $(\nu = 0, N = 1) \rightarrow (\nu = 2, N = 0)$  and  $(\nu = 0, N = 0) \rightarrow (\nu = 1, N = 1)$  transitions, require lasers with wavelengths around  $1.9\mu\text{m}$  and  $3.8\mu\text{m}$ , respectively [117]. These wavelengths are conveniently covered by near-IR continuous-wave optical parametric oscillators (OPO's) [118]. To ensure that the scheme remains

insensitive to the intrinsic linewidth and drifts in the OPO, one should require an effective rate for the pumped transitions of  $\sim 90\%$  of the  $A$ -coefficients, at a detuning of  $\sim 10$  MHz. This is fulfilled at an intensity of a few hundreds of  $W/cm^2$ , which is realistic using a laser beam with a few tens of mW power focused to a beam waist of  $\sim 100\mu m$ . Note that such a waist is much larger than the localization of translationally cold ions [38].

In order to make sure that all magnetic sublevels of the rotational states are addressed by the pump laser fields, the polarization of the pumping radiation must be varied on the time scale of the optical pulses in the case of the Raman scheme and at a rate faster than rotational transition by BBR is the case of the direct scheme. In both cases this can be done by using a modulated Pockels cell.

### 3.4 Laser Cooling of Molecular Rotations Assisted by Incoherent Sources

In the previous sections, we saw that it is possible to utilize BBR to cool molecular rotations by feeding a closed optical pumping cycle with population from states not explicitly included in the cooling cycle. Having established cooling by utilizing BBR, one may consider tailoring incoherent fields to assist cooling further. In particular, it could be experimentally attractive to eliminate one of the pumping lasers in the presented cooling schemes by connecting the two "pump states" with an incoherent field. In the remaining sections of this chapter, we will elaborate further on this idea. For example, the incoherent field is tailored for optimum cooling into the ro-vibrational ground state based on the constraints set by the spectral density profile of a realistic mercury lamp [119]. We find that the timescale for the cooling can be made shorter than the timescale of the cooling schemes of the previous sections.

#### 3.4.1 Cooling schemes

The laser excitations and subsequent spontaneous emission paths for the considered schemes are presented in figure 3.7 with laser-induced transitions being either (a) Raman transitions via an excited electronic state or (b) direct transitions between ro-vibrational levels. The effect of the laser-induced transitions is to pump the molecule into the  $(\nu = 0, N = 0)$  ground state. This is realized by a pumping cycle composed of (i) excitation from the  $(\nu = 0, N = 2)$  state to an excited vibrational level and (ii) subsequent dipole allowed radiative decays. Assuming an initially broad rotational distribution in thermal equilibrium with the environment at 300 K, the repeated depletion of the  $(\nu = 0, N = 2)$  state will then result in a transfer of population towards the rotational ground state by BBR-induced rotational transitions. Due to the nature of BBR, no control of the strength of individual rotational transitions is possible. This can, however, be obtained by introducing an additional incoherent far-infrared radiation field derived from, e.g., a high-pressure mercury lamp and frequency filters. In this way,

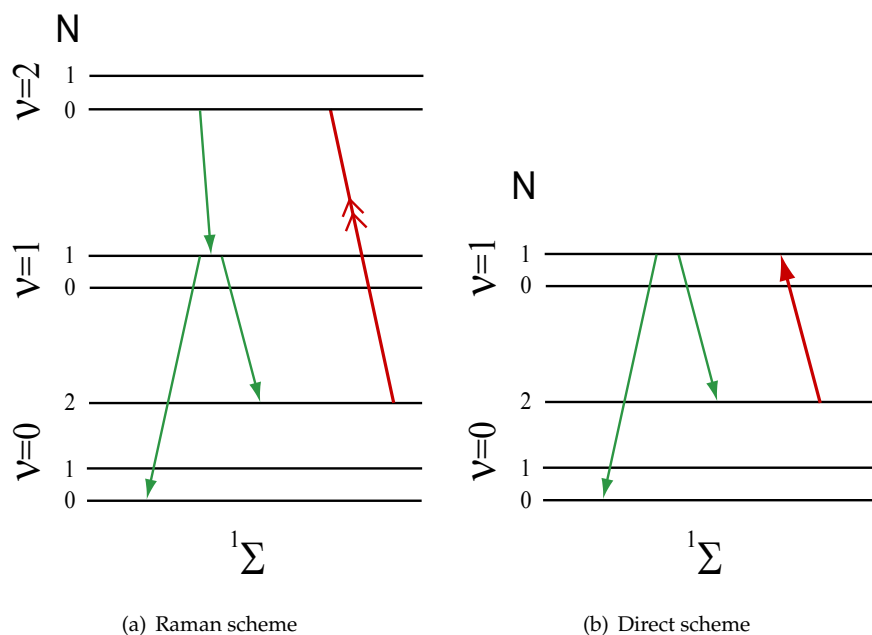


**Figure 3.7:** The variation of the cooling concept, when an incoherent field is used in addition to BBR in order to drive rotational transitions. (a) Scheme based on a Raman transition via an excited electronic state of the molecule. (b) Scheme based on a direct laser transition between vibrational states. On the figure, Red Line with double-arrow represents a transition between ro-vibrational states driven by Raman pulses, the Red Line with single-arrow represents a direct dipole allowed laser excitation. Finally, Green arrows denote the dipole allowed spontaneous decay paths.

it is possible to tailor the radiation intensity around the individual rotational transitions. One can for instance use a dichroic filter as a high-pass filter [120] such that the rate of the  $(\nu = 0, N = 1) \leftrightarrow (\nu = 0, N = 2)$  cooling transition will be enhanced without effecting the rate of the  $(\nu = 0, N = 0) \leftrightarrow (\nu = 0, N = 1)$  heating transition.

### Experimental considerations

Though the cooling schemes should work for a large variety of ions and neutrals, we again focus on implementations in the particular case of  $\text{MgH}^+$ . In section 3.1 we saw that the laser intensities needed to saturate the Raman transition depicted in figure 3.7(a) in  $\text{MgH}^+$  are readily obtained by standard pulsed laser systems. For the direct scheme (figure 3.7(b)), the infrared field could be obtained by difference-frequency generation or by applying an optical parametric

oscillator based on the beam of a pulsed Nd:YAG laser [121, 122]. At the wavelength  $\simeq 5.9 \mu\text{m}$  needed to drive the  $(\nu = 0, N = 2) \leftrightarrow (\nu = 1, N = 1)$  transition in  $\text{MgH}^+$  [51], infrared-light generating nonlinear crystals can typically deliver an energy of  $\sim 10 \mu\text{J}$  per 10 ns pulse. Given the Einstein A-coefficient of  $\simeq 20 \text{s}^{-1}$  for the relevant transition [94] and assuming a maximum detuning of 1 GHz due to fluctuations in the frequency of the laser light, saturation of the transition during a 10 ns pulse requires an averaged intensity of  $100 \text{W}/\text{mm}^2$ , corresponding to a  $1 \mu\text{J}$  pulse focused to a realistic beam spot size of  $1 \text{mm}^2$ . Another option is to apply a quantum-cascade laser [123, 124], available at the relevant wavelength and intensities [125]. Quantum-cascade lasers are particularly attractive due to high cost-effectiveness and the fact that they can be designed to emit radiation with wavelengths ranging from  $\sim 3.5 - 25 \mu\text{m}$ . Significant technological efforts are ongoing to further widen the wavelength range.

Turning to the lamp, the presence of such an incoherent far-infrared source may improve the cooling rate by speeding up the feeding of the  $(0, 2)$  pump state from higher-lying states. The transfer of population away from the pump state is, however, inevitable and it may thus be expected that a certain spectral density distribution of the incoherent radiation will be optimal for the cooling schemes. In the following we investigate this hypothesis under the experimental constraints given by available incoherent sources and possible filtering and focusing systems. To estimate the energy density at the molecular target, we note that the output of a standard mercury lamp at a wavelength of  $\sim 500 \mu\text{m}$  corresponding to low-lying rotational transitions in  $\text{MgH}^+$  is similar to a BBR source at a temperature of 4000 K [119]. We assume unit magnification of the light source and  $2\pi$  solid angle pickup of radiation. This is reasonable since a setup with a reflector and with large aperture molded lenses, which are available in this wavelength regime, would ideally give  $\sim 4\pi$  pickup. Allowing for some additional losses from absorption and scattering we use  $\rho_{lamp} = 5\rho_{300K}$  as the maximum achievable spectral energy density from the lamp at the molecular ions [126].

### 3.4.2 Numerical simulations

We model the cooling dynamics by rate equations as outlined in section 3.2, but with the incoherent radiation densities,  $W(\omega_{ij})$ , determined by the applied incoherent field as well as BBR. Again, we assume 100 Hz repetition rate of pulsed lasers saturating the transitions addressed in every pulse.

We maximize the final population in the ground state as function of the incoherent radiation density at the individual rotational transition frequencies for specific cooling times by the downhill simplex method [127]. It is found that the density distribution should be the maximum attainable for the  $(\nu = 0, N = 1) \leftrightarrow (\nu = 0, N = 2)$ ,  $(\nu = 0, N = 2) \leftrightarrow (\nu = 0, N = 3)$ , and  $(\nu = 0, N = 3) \leftrightarrow (\nu = 0, N = 4)$  transitions, but zero otherwise. This rather simple shape may be understood by first noting that for a molecule subject to BBR, stimulated processes will dominate at low frequencies while spontaneous

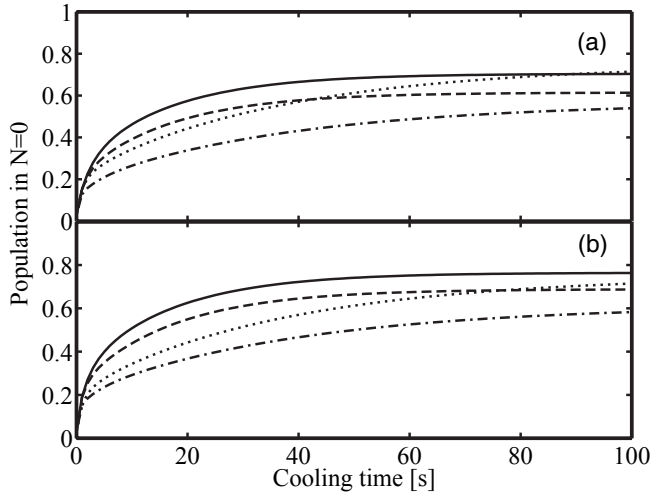


**Figure 3.8:** Ground state population of  $\text{MgH}^+$  vs. cooling time for **(a)** Raman and **(b)** direct schemes with the optimized distribution of incoherent radiation (solid), “quartz-filtered” distribution (dashed) and no incoherent source (dashed-dotted). The result of the scheme of figure 3.1 is depicted for comparison (dotted).

emission will do so at high frequencies. As a result the highest populated state is to be found where spontaneous and stimulated transition rates are balanced (see the red columns in figure 3.10). The BBR density is low and transition rates are small for rotational states lying below the state which is maximally populated in thermal equilibrium (300 K). However, introducing additional incoherent radiation to drive transitions between these low-lying states will accelerate the process of refilling the  $(\nu = 0, N = 2)$  pump state, and thereby increase the cooling rate. Radiation which couples states above the peak in the 300 K BBR population distribution, would heat the distribution as would any radiation in addition to BBR at the  $(\nu = 0, N = 0) \leftrightarrow (\nu = 0, N = 1)$  transition frequency.

Figure 3.8 shows simulations of the ground state population as a function of time for various incoherent fields. The solid curves are the results with the optimized field. While it is critical to keep the  $(\nu = 0, N = 0) \leftrightarrow (\nu = 0, N = 1)$  transition rate low (which can be achieved by introducing a sharp high-pass filter [120]), simulations show that the results are less sensitive to the actual shape of the frequency cut-off at the higher rotational transitions. In figure 3.8 this latter point is illustrated by comparing the results for the optimal source with the results for an incoherent field distribution corresponding to maximum attainable intensities at all transitions from  $(\nu = 0, N = 1) \leftrightarrow (\nu = 0, N = 2)$  to  $(\nu = 0, N = 7) \leftrightarrow (\nu = 0, N = 8)$ , roughly equivalent to introducing a piece of quartz in the beam path. We have also included calculations without the incoherent source to show that the effectiveness of the cooling scheme depends

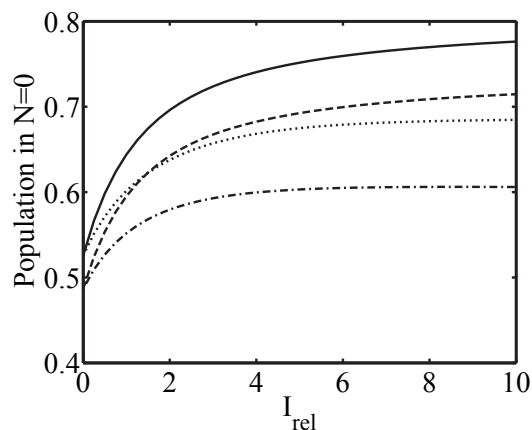


**Figure 3.9:** Ground state population of  $\text{MgH}^+$  after 60 s of cooling vs. relative intensity of incoherent radiation from a lamp. The schemes are: Direct scheme with optimal incoherent radiation distribution (solid) and direct scheme with “quartz-filtered” distribution (dotted), Raman scheme with optimal incoherent radiation distribution (dashed), and Raman scheme with “quartz-filtered” incoherent radiation distribution (dashed-dotted). Note scale of the ordinate.

critically on the rotational transitions induced by the lamp. For comparison, the results of the Raman scheme simulation of section 3.2.4, where the ( $\nu = 0, N = 1$ ) state is depleted by a second Raman transition, is shown.

For very short cooling times ( $< 1$  s) essentially no differences between the schemes can be observed since the relatively slow rotational transitions are not yet important. On intermediate timescales ( $\sim 10$  s), however, the effect of the added incoherent field is evident and the optimized scheme has an advantage over the scheme of section 3.1. Finally, at longer times the laser-depletion of the ( $\nu = 0, N = 1$ ) state as well as the additional heat introduced by the incoherent source, make the cooling scheme of section 3.1 slightly more efficient.

For a fixed cooling time of 60 s, figure 3.9 shows the dependence of the cooling efficiency on the intensity,  $I_{rel}$ , of the incoherent source relative to BBR at 300 K in the frequency range of interest. The influence of the incoherent field on the cooling process is seen to increase significantly up to  $I_{rel} \approx 5$ , from where only minor improvements may be obtained.

In figure 3.10, the population distribution after 60 s of cooling for the case of  $I_{rel} = 5$  is compared with the initial Boltzmann distribution for the four schemes considered in figure 3.9. With the optimized spectral distribution we obtain 68 % and 74 % in the ground state with the Raman and direct scheme, respectively, corresponding to temperatures of  $\sim 7$  K, which is of astrophysical relevance [128, 129]. In both schemes, the depletion of the rotational levels above the  $N = 2$  pump state is evident. Compared to the optimized case, one observes



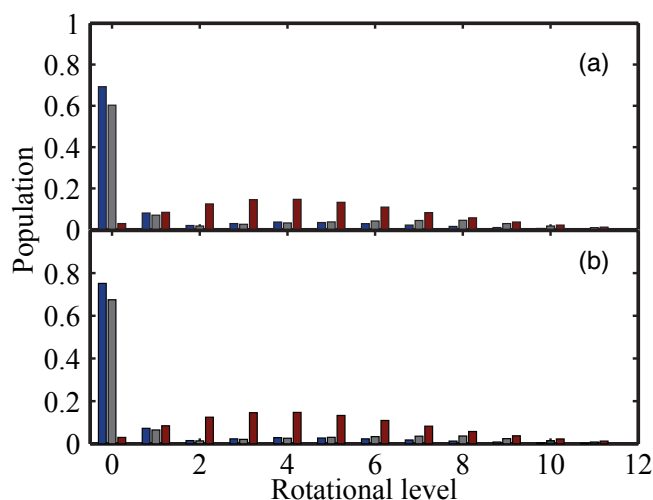


**Figure 3.10:** Rotational population distribution for  $\text{MgH}^+$  after 60 s of cooling using (a) Raman and (b) direct schemes with optimized energy distribution of the incoherent source (blue), “quartz-filtered” energy distribution (grey), compared to the initial population distribution at 300 K (red).

slightly larger populations in the rotational states above  $N = 5$  for the “quartz-filtered” source due to the heating effect of the high frequency components in this distribution.

Above we only considered time-independent incoherent sources, but since the cooling time is 10 – 100 s, it would be possible to change the shape of the incoherent field during cooling and hence look for improvements of the schemes by optimizing a time-dependent spectral distribution of the lamp. In order to investigate this point, we estimated the maximal attainable cooling efficiency using an arbitrary time-dependent incoherent source, by optimizing the system at steady state. It was found that in the case of  $\text{MgH}^+$  a ground state population of 75 % (Raman) and 79 % (direct) could be obtained which corresponds to an increase by 7 % and 5 %, respectively, compared to the result with the optimum static spectral distribution. Furthermore, in order to gain information on a possible optimized time-dependent field, we did a calculation where the field was optimized after 5, 10, 15, . . . , 60 s. At each instant of time we then compared the population in the ground state with that from the time-independent lamp-field considered above. The differences in cooling were marginal and could not be observed at the scale of figure 3.10.

We have tested the schemes on ionic molecules with other ro-vibrational transition properties. In the case of  $\text{ArH}^+$ , which is known to be a fast infrared emitter, ground state population of 80 % can be achieved after only 10 s of cooling, which should be compared with the steady-state value of 90 %.

### 3.5 Conclusion

Here, we have focused on the description of schemes for cooling the rotational degree of freedom of molecular ions with the ground state symmetry,  $^1\Sigma^+$  and without hyperfine splittings. Such splittings are, however, typically much smaller (e.g.  $\sim 1$  MHz in  $\text{BeH}^+$  [130]) than the bandwidth ( $\sim 1 - 30$  GHz) of typical pulsed laser systems applicable in the Raman scheme and, consequently, all hyperfine levels will be addressed by the pump fields.

Furthermore, we have demonstrated the surprising result that polar molecules trapped in a room temperature environment can be rotationally cooled by the combination of a lamp inducing rotational transitions and a laser driving a single ro-vibrational transition. Under experimentally realistic constraints, we have shown that there exists a specific tailored incoherent frequency distribution which optimizes the cooling process when considering time-independent fields. We estimated that an optimized time-dependent incoherent field will only lead to a minor increase in the ground state population. The considered schemes are very simple from an experimental point of view, and hence very attractive for sympathetically cooled target molecular ions, and potentially also for trapped neutral molecules and molecular ions in storage rings.

If one considers an implementation of the schemes in connection with cooling in storage rings [92, 131], a larger focal spot of the laser would be required in order to obtain overlap with the ion beam. This significantly increases the laser power requirements and leads us to conclude that the pulsed Raman scheme could be considered while the direct scheme would probably not be possible due to the limited power of present day OPO systems, although the application of a quantum cascade laser may circumvent this problem. Also, the schemes assisted by additional incoherent radiation may be difficult to implement in storage rings, since the incoherent sources offer very limited power. The application of a backwards wave oscillator [132] to saturate the  $(\nu = 0, N = 1) \leftrightarrow (\nu = 0, N = 2)$  is, however, expected to give results comparable to the schemes assisted by incoherent radiation sources, thus mitigating the problem of limited power from incoherent sources.

The schemes may be extended to molecular ions with more complicated ground state configurations at the cost of more detailed considerations of the laser systems used. We shall elaborate further on this in the following chapter.

To summarize, we have shown how initially translationally cold, trapped molecular ions can be internally cooled by simple optical pumping schemes when assisted by the black-body-radiation. The schemes are simple, and robust, and the light source requirements are modest compared to state-of-the-art laser systems.

# CHAPTER 4

## Cooling of Molecular Ions with Rotational Substructure

In the previous chapter, we discussed cooling schemes applicable to molecular ions with their ro-vibrational energy levels determined by molecular rotation and vibration only. This will be the case if the relevant electronic state has vanishing total spin and if the projection of the orbital angular momentum of the electronic state along the internuclear axis is zero, i.e., in  $^1\Sigma$  states. We now turn to the other electronic ground states found in lighter diatomic hydride ions:  $^2\Sigma$ ,  $^3\Sigma$  and  $^2\Pi$

A range of quantum numbers will be needed to describe the rotational sub-states of the molecules to be discussed. We follow the notation of Herzberg [51] designating the quantum numbers as indicated in Table 4.1. The meaning of the coupled angular momenta is explained below.

We now treat Hunds coupling case (a) and (b) separately and study cooling schemes for both cases.

### 4.1 $(2S+1)\Pi$ -states; Hunds Case (a)

An interaction term of the form  $H^{so} = AL \cdot S$  will appear in the Hamiltonian if the projection on the internuclear axis of both electronic spin,  $S$ , and electronic orbital angular momenta,  $L$ , are nonzero. For moderate rotational excitations,  $H^{so}$  will normally dominate over terms from the rotational Hamiltonian,  $H^{rot} = B \cdot N^2$ . It is therefore convenient to choose the Hunds case (a) basis set, consisting of basis functions  $|n, S^2 J^2 M_J \Lambda \Sigma \Omega\rangle$  where  $n$  is collecting the quantum numbers defining the molecular state but not mentioned in Table 4.1. In this basis set, the unperturbed Hamiltonian<sup>1)</sup> is diagonal and the main per-

---

<sup>1)</sup>The unperturbed Hamiltonian refers to the Hamiltonian of the molecule, neglecting both  $H^{so}$  and  $H^{rot}$  as well as the nuclear spins

Label	Definition
<b>L</b>	Total electronic orbital angular momentum
$\Lambda$	Projection of <b>L</b> on internuclear axis
<b>N</b>	Angular momentum of molecular rotation
<b>S</b>	Total electronic spin
$\Sigma$	Projection of <b>S</b> on internuclear axis
$M_S$	Projection of <b>S</b> on laboratory Z-axis
$\Omega$	$\Lambda + \Sigma$
<b>K</b>	Sum of <b>N</b> and $\Lambda \cdot \hat{\zeta}$
<b>J</b>	Total angular momentum of molecule neglecting nuclear spin
$M_J$	Projection of <b>J</b> on laboratory Z-axis

**Table 4.1:** Overview of quantum numbers describing the rovibrational state of a molecule, neglecting nuclear spin.  $\hat{\zeta}$  denotes a unit vector along the internuclear axis.

turbation term,  $H^{so}$ , is nearly diagonal with the off-diagonal terms satisfying  $\Delta\Omega = 0$ . The  $|n, \mathbf{S}^2 \mathbf{J}^2 M_J \Lambda \Sigma \Omega\rangle$  basis states are therefore a good approximation to eigenfunctions with good quantum numbers if  $|A| \gg B \cdot J$ , known as the Hunds case (a) limit. We restrict the calculation to the pure Hunds case (a) limit in the following section,  $^2\Pi$  states are often close to this limit at low rotational excitations and they form the most interesting example of Hunds case (a) coupling for our purpose, as they appear as ground states of a number of molecules interesting for cooling, including  $\text{NH}^+$  and  $\text{FH}^+$ .

### 4.1.1 Energy levels and selection rules

The first order effect of  $H^{so}$  is to split the electronic ground state into states according to the value of  $\Omega$ . For each of these states there will be a set of rovibrational sub-states arising from  $H^{rot}$ .

In Hunds case (a), the molecule is well-described as a rotating symmetric top, for which the rotational energies are expressed by [51]

$$F_\nu(J) = B_\nu(J(J+1) - \Omega^2). \quad (4.1)$$

Here  $J$  must take values greater than  $|\Omega - N|$  and the lowest rotational state will therefore, in general, have  $J \neq 0$ . The overall structure of the molecular energy levels can be seen from the sketch of the modified cooling scheme in figure 4.1 for  $S = \frac{1}{2}$ .

The case (a) basis state in the laboratory frame can be written as a Wigner

rotation of the corresponding wave function in the molecular rest frame [133]

$$\begin{aligned} \langle \{\mathbf{r}_i\} \mathbf{R} | nJM_J\Omega S\Sigma \rangle = \\ \sqrt{\frac{2J+1}{8\pi^2}} \langle \{\mathbf{r}'_i\} R | n \rangle | S\Sigma \rangle \mathcal{D}_{M_J\Omega}^{J*}(\alpha\beta\gamma), \end{aligned} \quad (4.2)$$

where  $\{\mathbf{r}_i\}, \mathbf{R}$  ( $\{\mathbf{r}'_i\}, R$ ) are the electronic and internuclear coordinates in the laboratory (body-fixed) frame. Finally  $\mathcal{D}_{M\Omega}^{J*}(\alpha\beta\gamma)$  is an element of the Wigner rotation matrix evaluated at the given Euler angles,  $\alpha\beta\gamma$  [134]. As in the previous chapter, we postpone the rather technical derivation of the Hönl-London factors  $S(J', J'')$  to appendix C. Here, we just present the result,

$$\begin{aligned} S(J', J'') = (2J'' + 1) \times \\ | \langle J''\Omega''1(\Omega' - \Omega'') | J'\Omega' \rangle |^2 \delta_{S', S''} \delta_{\Sigma', \Sigma''}, \end{aligned} \quad (4.3)$$

where  $\langle J''\Omega''1(\Omega' - \Omega'') | J'\Omega' \rangle$  is a Clebsch-Gordan coefficient. This result immediately gives us the following dipole selection rules

$$\begin{aligned} \Delta J &= 0, \pm 1, \quad \text{but } J = 0 \leftrightarrow J = 0 \\ \Delta \Lambda &= 0, \pm 1, \\ \Delta S &= \Delta \Sigma = 0, \end{aligned} \quad (4.4)$$

which can also be combined to  $\Delta \Omega = 0$ .

### 4.1.2 Cooling schemes

For  ${}^2\Pi$  molecules we propose the cooling scheme depicted in figure 4.1, where we distinguish between  $\Omega = \frac{1}{2}$  and  $\Omega = \frac{3}{2}$ . Since only transitions with  $\Delta J = 0, \pm 1$  are allowed, we can pump population from the first excited rotational state in the vibrational ground state to the rotational ground state of the first excited vibrational level, ( $\nu = 1, J = \Omega$ ). The former is denoted the "pump state" in analogy with the nomenclature in chapter 3. From ( $\nu = 1, J = \Omega$ ), spontaneous emission brings population either back to the pump state or down to the ro-vibrational ground state. The cooling scheme must be applied for each populated  $\Omega$  state individually. In figure 4.1 we have assumed population of both  $\Omega = \frac{1}{2}$  and  $\Omega = \frac{3}{2}$ . In the absence of incoherent radiation this forms a pumping cycle where population initially in the ( $\nu = 0, J = \Omega + 1$ ) state is transferred to the ro-vibrational ground state. As in the singlet case, the presence of BBR and possibly additional incoherent radiation from a lamp, will induce rotational transitions and thereby feed the pump state with population from higher-lying states. The entire population is therefore cooled.

Cooling schemes for other Hunds case (a) molecules may be derived from straightforward generalization of the  ${}^2\Pi$  scheme.

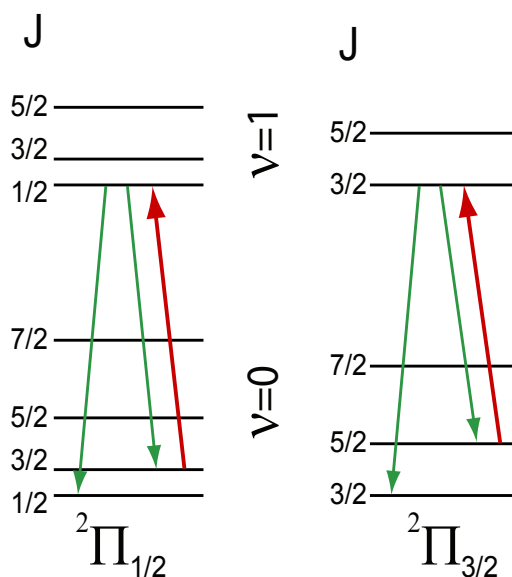


**Figure 4.1:** Cooling scheme for  ${}^2\Pi$ -states. Each of the two possible values of  $\Omega$  results in a series of energy levels and it is necessary to cool the  ${}^2\Pi_{\frac{1}{2}}$  and  ${}^2\Pi_{\frac{3}{2}}$  separately if both are populated. Population is pumped from the first excited rotational state in the  $\nu = 0$  vibrational ground state to the ro-vibrational ground state by a laser induced vibrational transition and subsequent spontaneous decays. All the involved transitions are dipole allowed, cf. equation (4.4). Red arrows indicate laser pumped transitions while green arrows indicate spontaneous decay paths. The  $\Lambda$  doubling is not shown in the figure.

### 4.1.3 Numerical simulations

The simulations are done using the approach described in section 3.2.3, but with the dipole transition matrix elements calculated using the Hönl-London factors of equation (4.3). We have chosen the molecule  $\text{FH}^+$  as an example of a  ${}^2\Pi$  ground state molecule.

Since the spin-orbit coupling parameter,  $A = -292 \text{ cm}^{-1}$ , is much larger in magnitude than the rotational constant,  $B = 17 \text{ cm}^{-1}$ ,  $\text{FH}^+$  is best described in the Hund's case (a) scheme [135]. The appropriate cooling scheme is depicted in figure 4.1, although it should be noted that, for  $\text{FH}^+$ ,  $\Omega = \frac{3}{2}$  is the lower state. To model the cooling scheme, we use the dipole moment functions in reference [136] and the accurate spectroscopic data of reference [135].

The pumping is done from the first excited rotational level in the cooling scheme of figure 4.1. This fact, combined with a large permanent dipole moment and hence rotational transition rate of  $\text{FH}^+$  (2.57 Debye), makes the effect of the broadband incoherent radiation marginal. We have therefore performed

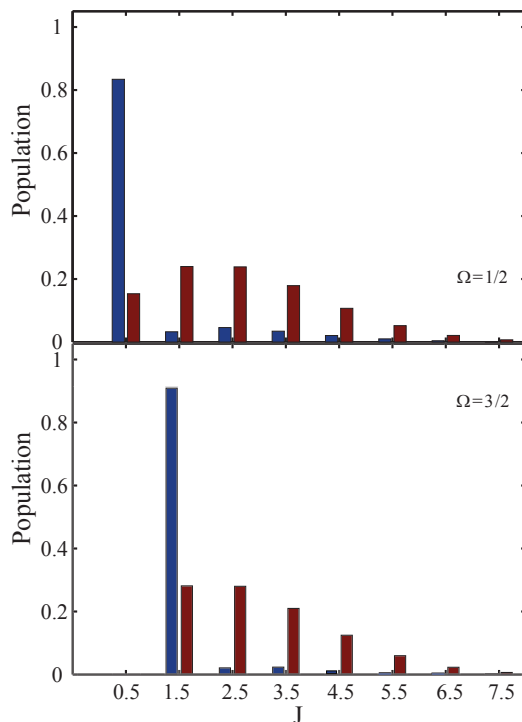


**Figure 4.2:** Cooling efficiency of  $\text{FH}^+$  ( $X^2\Pi$ ) in the two  $\Omega$  sub-states. In the dipole approximation the two sub-states are uncoupled if pure Hunds case (a) applies. The cooling scheme will therefore be significantly simplified if one can design the experiment such that only the lowest  $\Omega = \frac{3}{2}$  state is populated in the cooling scheme. As in the previous figures, the red columns represent the initial BBR distribution of population, while the blue columns represent the population distribution after cooling.

the simulations without the inclusion of an incoherent source. Results of the simulations are given for both the  $^2\Pi_{1/2}$  and  $^2\Pi_{3/2}$  states in Figs. 4.2 and 4.3.

Further splitting of the levels indicated in figure 4.1 will appear due to  $\Lambda$  doubling. The effect is largest in the  $^2\Pi_{\frac{1}{2}}$  state where it has a magnitude on the order of 10 GHz, which is more than one can expect to cover with the bandwidth of a single pulsed laser. Therefore the laser transitions indicated for the  $^2\Pi_{\frac{1}{2}}$  scheme needs to be divided into two. The splitting of the lowest  $^2\Pi_{\frac{3}{2}}$  state is an order of magnitude smaller, so it is not necessary to split that laser transition if a pulsed laser system is used. This leaves us with three laser frequencies to use for the cooling scheme if we assume that both  $\Omega = \frac{1}{2}$  and  $\Omega = \frac{3}{2}$  are populated.

Complications arise if we are not in the pure Hunds case (a) scheme. This occurs if the rotational part of the Hamiltonian cannot be neglected compared

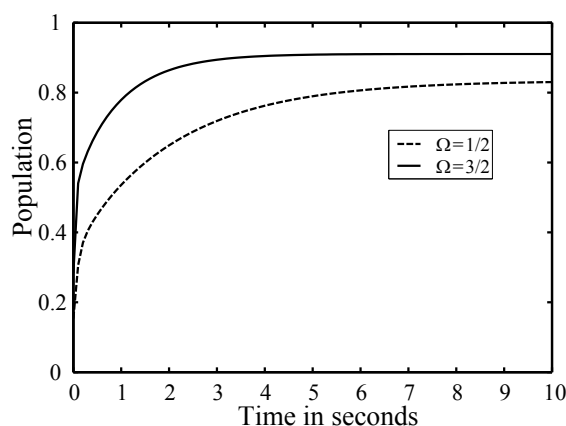


**Figure 4.3:** Cooling efficiency as function of cooling time for the two  $\Omega$  sub-states of the  $^2\Pi$  electronic ground state of  $\text{FH}^+$ . The cooling is seen to reach steady-state after  $\lesssim 10$  s without the inclusion of an incoherent source, largely due to the large permanent dipole moment of  $\text{FH}^+$ .

to the spin-orbit part. Treated in the case (a) basis, the rotational part will produce non diagonal perturbations [53]. This would allow a coupling from  $(\nu = 1, J = \Omega) \rightarrow (\nu = 0, J = \Omega + 2)$  (the introduction of quadrupole couplings would have a similar effect). We do not expect this effect to be significant given the difference between  $|A|$  and  $B$ . We did, however, check the stability of the scheme when introducing such couplings and found that due to the fast rotational redistribution rates, the population that was coupled out of the cooling cycle by  $\Delta J = 2$  transitions would rapidly be taken back. The negative effect of such couplings is small (less than 10% decrease in cooling efficiency) if the  $\Delta J = \pm 2$  couplings are less than 20% of the  $\Delta J = 0$  coupling strength.

It should be noted that since coupling between states with different  $\Omega$  is absent in the pure case (a) coupling, it may be possible to prepare the sample so that only the  $\Omega = \frac{3}{2}$  sub-state is populated. This would make the lasers addressing the  $\Omega = \frac{1}{2}$  level superfluous. In that case only a single laser frequency is needed to cool the molecule.

## 4.2 $(2S+1)\Sigma$ -states; Hunds Case (b)

If  $B \gtrsim |A|$  or at high rotational excitations the Hunds case (a) basis functions will no longer be approximate energy eigenfunctions. If  $H^{rot}$  dominates, the Hunds case (b) basis,  $|nJ^2M_JN^2S^2\Lambda\rangle$  is convenient since the total Hamiltonian is nearly diagonal in this basis. In particular, this is fulfilled for  $^{2S+1}\Sigma$  states, which are common as electronic ground states of light diatomic molecular ions



including  $\text{BH}^+$  ( $X^2\Sigma$ ) and  $\text{OH}^+$  ( $X^3\Sigma$ ). Below, we treat the  $^2\Sigma$  and  $^3\Sigma$  cases separately.

### 4.2.1 Energy levels of doublet states

The sub-states of a rotational level in a molecule in a  $^2\Sigma$  state are split due to the interaction of the spin of the unpaired electron and the molecular rotational angular momentum. This is due to the spin-rotation Hamiltonian  $H^{sr} = \gamma \mathbf{N} \cdot \mathbf{S}$  where  $\gamma$  denotes the spin-rotation coupling constant. The resulting energies in the doublet are given by [51]

$$F_1(N) = BN(N+1) + \frac{1}{2}\gamma N, \quad (4.5)$$

$$F_2(N) = BN(N+1) - \frac{1}{2}\gamma(N+1), \quad (4.6)$$

and the sub-states are denoted  $F_1$  and  $F_2$  for  $J = N + \frac{1}{2}$  and  $J = N - \frac{1}{2}$  respectively.

### 4.2.2 Energy levels of triplet states

Molecular ions in  $^3\Sigma$  electronic states will, apart from the spin-rotation splitting discussed above, have an additional splitting from the coupling of the electronic spin of the two unpaired electrons. Such states are relatively rare, as pairing of the electronic spins is usually favored. Nevertheless, the ionic hydrides in the 16th group of the periodic table, including  $\text{OH}^+$  and  $\text{SH}^+$ , have such electronic ground states. We therefore consider the applicability of the cooling schemes to such states here. The energies of the three spin sub-states are given by [51]

$$F_1(N) = BN(N+1) + \frac{2\lambda(N+1)}{2N+3} + \gamma(N+1), \quad (4.7)$$

$$F_2(N) = BN(N+1), \quad (4.8)$$

$$F_3(N) = BN(N+1) - \frac{2\lambda N}{2N-1} - \gamma N. \quad (4.9)$$

In analogy with the doublet case,  $F_1$ ,  $F_2$ , and  $F_3$  denotes the sub-states with  $J = N + 1$ ,  $J = N$ , and  $J = N - 1$ , respectively. In the expression,  $\gamma$  is the spin-rotation coupling constant and  $\lambda$  is the spin-spin-splitting constant. The latter is normally an order of magnitude or more larger than  $\gamma$  and, consequently, the multiplet splitting of triplet states at moderate rotational excitations are much greater than the corresponding splittings of a doublet electronic states.

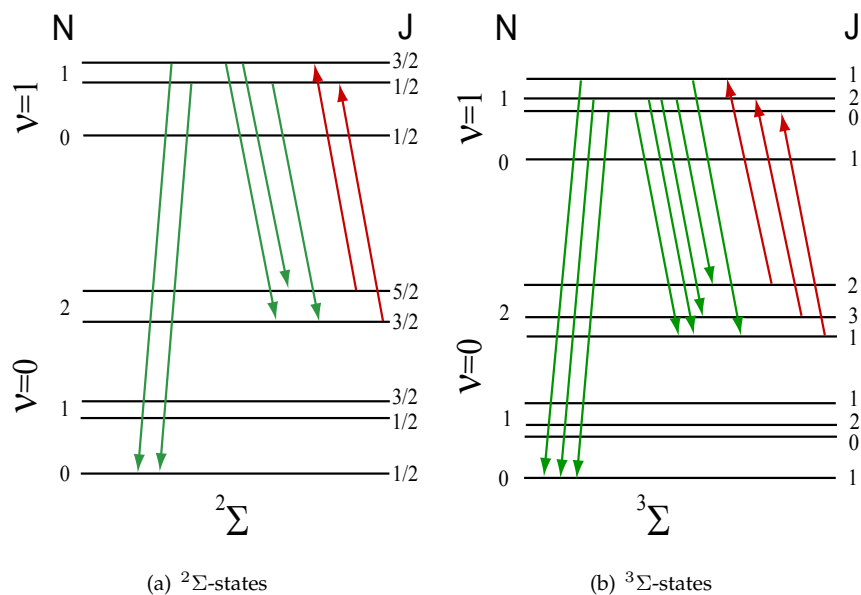


**Figure 4.4:** (a) Cooling scheme for  ${}^2\Sigma$ -states. Due to the spin-rotation coupling each rotational quantum state,  $N$ , splits into two sub-levels with  $J = |N + \frac{1}{2}|, |N - \frac{1}{2}|$ . (b) Cooling scheme for  ${}^3\Sigma$ -states. Due to spin-spin and spin-rotation coupling each rotational quantum state  $N$  split into sub-levels with  $J = |N + 1|, N, |N - 1|$ . In both (a) and (b), the dipole-allowed vibrational transitions are shown on the figure with red lines to indicate laser pumped transitions and green lines to indicate the subsequent spontaneous decay paths.

### 4.2.3 Selection rules

In Hunds case (b), the good quantum numbers are  $N, S, J, M_J$  and  $\Lambda$ . We therefore write the eigenfunctions in the laboratory frame as

$$\begin{aligned} \langle \{\mathbf{r}_i\}, \mathbf{R} | n, J, M_J, N, S, \Lambda \rangle &= \sqrt{\frac{2N+1}{8\pi^2}} \times \\ &\sum_{M_S=-S}^S \sum_{M_N=-N}^N \langle \{\mathbf{r}'_i\}, R | n \rangle \langle N, M_N, S, M_S | J, M_J \rangle \times \\ &|S, M_S\rangle \mathcal{D}_{M_N, \Lambda}^{N*}(\alpha, \beta, \gamma), \end{aligned} \quad (4.10)$$

where  $\{\mathbf{r}_i\}, \mathbf{R}$  ( $\{\mathbf{r}'_i\}, R$ ) are the electronic and internuclear coordinates in the laboratory (body-fixed) frame. We then follow the approach of appendix C to

get the Hönl-London factors

$$S(J', J'') = (2N'' + 1)(2J' + 1)(2J'' + 1) \times \langle N'' \Lambda'' 1(\Lambda' - \Lambda'') | N' \Lambda' \rangle^2 \left\{ \begin{matrix} S' & N'' & J'' \\ 1 & J' & N' \end{matrix} \right\}^2 \delta_{S'S''}, \quad (4.11)$$

where  $\left\{ \begin{matrix} S' & N'' & J'' \\ 1 & J' & N' \end{matrix} \right\}$  is a 6j symbol [134]. The following selection rules are extracted

$$\begin{aligned} \Delta J &= 0, \pm 1 \quad \text{but} \quad J = 0 \leftrightarrow J = 0 \\ \Delta N &= 0, \pm 1 \quad \text{but} \quad \Delta N \neq 0 \quad \text{if} \quad \Lambda' = \Lambda'' = 0 \\ \Delta \Lambda &= 0, \pm 1, \\ \Delta S &= 0. \end{aligned} \quad (4.12)$$

#### 4.2.4 Cooling scheme

The cooling scheme proposed for Hunds case (b) molecules closely resembles the singlet cooling scheme. It is depicted in figure 4.4(a) for  ${}^2\Sigma$  molecules and in figure 4.4(b) for  ${}^3\Sigma$  molecules. The optical pumping is done from the  $(\nu = 0, N = 2, J)$  set of states to  $(\nu = 1, N = 1, J')$ . Then dipole allowed spontaneous decay will result in transitions back to the "pump states" or to the non-degenerate ro-vibrational ground state. The only change to the scheme when compared to the singlet case is to assure the addressing of all sub-states in the  $N$  multiplet. This is possible because the  $\Delta N = \pm 1$  selection rule for  $\Sigma$  states from equation (4.12) is the same as in the singlet case. The role of BBR and additional incoherent radiation is the same as in the previous schemes.

The number of transitions to be pumped is three for the  ${}^3\Sigma$  states and two for the  ${}^2\Sigma$  states. The splitting of the levels in the former is expected to be much larger than for the  ${}^2\Sigma$  case, since the spin-spin coupling parameter,  $\lambda$ , is much greater than the spin-rotation parameter,  $\gamma$ , as mentioned in section 4.2.

#### 4.2.5 Numerical simulations

We now proceed with numerical simulations of the presented cooling schemes. The simulations will be made with  $\text{BH}^+$  as an example of a molecular ion with the  ${}^2\Sigma$  ground state, while  $\text{OH}^+$  is used as an example of a molecule with a  ${}^3\Sigma$  ground state.

##### $\text{BH}^+ ({}^2\Sigma)$

Here, we treat  $\text{BH}^+$  as an example of a  ${}^2\Sigma$  ground state molecule and discuss the molecule specific parameters and their implications on the cooling schemes.

The numerical simulation is done for  ${}^{11}\text{B}^1\text{H}^+$  which is the dominant isotope (80%). We use the potential energy and dipole moment functions of reference [137]. With those functions, we use the approach of section 4.2.3 to

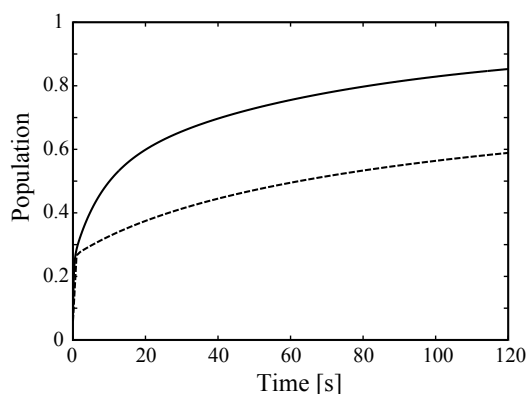


**Figure 4.5:** Population in the lowest rotational state of  $\text{BH}^+$  ( $X^2\Sigma$ ) as function of cooling time. Simulations are made using the scheme of figure 4.4(a) with BBR only (dashed line) and with the inclusion of the field from an incoherent source addressing the  $N = 1 \rightarrow N = 2$  and  $N = 2 \rightarrow N = 3$  transitions (solid line). We see that a significant improvement is obtainable using the incoherent source. In line with our experience from  $\text{MgH}^+$  there is only a couple of percent loss of cooling efficiency when using a softer low-frequency pass filter, for example, letting the broadband incoherent radiation extend to include transitions up to and including  $N = 4 \rightarrow N = 5$ .

calculate the matrix of Einstein coefficients between rotational and vibrational states. Finally, we make the simulation as described in section 3.2.3, but with the modified energy level structure. If one neglects fine-structure, the laser wavelength for the two, then identical, pump transitions depicted in figure 4.4(a) is  $\Lambda_0 = 4.17\mu\text{m}$ . The real resonant transition frequencies are shifted from this central frequency through equation (4.5), where  $\gamma = -0.014\text{ cm}^{-1}$  [51]. This gives a splitting of laser frequencies of  $\pm 0.007\text{ cm}^{-1} \simeq \pm 210\text{ MHz}$ . This difference is comfortably smaller than the typical bandwidth of a pulsed laser system. The hyperfine coupling coefficient has, to our knowledge, not been calculated. Typical values are, however, on the order tens to hundreds of MHz, allowing us to address all hyperfine substates with the same pulsed laser system. Hence, it is reasonable to expect that for practical implementations only a single pulsed laser frequency is needed.

The results of a numerical simulation are given in figure 4.5 and 4.6. We note that the convergence is quite slow compared to what we saw from  $\text{MgH}^+$  and  $\text{FH}^+$ . Optimal cooling is not obtained until after  $\sim 2$  minutes. This is not too critical as 60% of the population is in the ground state after 20 s. As expected from the discussion in the previous chapter, we find that the optimized distribution of the incoherent source addresses the transitions  $(\nu = 0, N = 1) \leftrightarrow (\nu = 0, N = 2)$  and  $(\nu = 0, N = 2) \leftrightarrow (\nu = 0, N = 3)$ . Similarly, it is confirmed that the cooling efficiency has little sensitivity towards the high frequency cutoff of

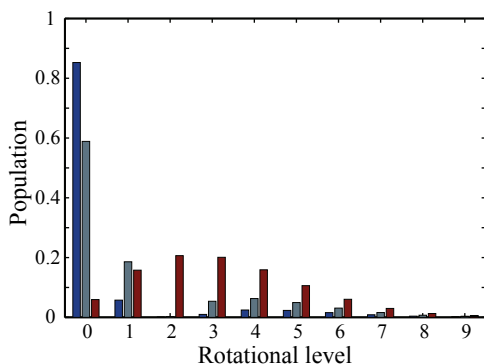


**Figure 4.6:** Population in the lowest rotational states of  $\text{BH}^+$  ( $X^2\Sigma$ ) after cooling in 120 s using the incoherent radiation from a lamp addressing the  $N = 1 \rightarrow N = 2$  and  $N = 2 \rightarrow N = 3$  transition (blue columns) and in BBR only (grey columns). The initial 300K Boltzmann distribution is included for comparison (red columns). We note that slightly better cooling efficiency should can be obtained using longer cooling times, cf. figure 4.5. This is, however, impractical and the obtainable improvements would be rather small. The substructure of the rotational levels is included in the simulation but omitted on the figure.

the incoherent field.

### $\text{OH}^+$ ( $^3\Sigma$ )

We have chosen  $\text{OH}^+$  as an example of a molecule with the  $^3\Sigma$  ground state. This molecule plays an important role in the chemistry in comet tails [138], the upper earth atmosphere, and interstellar clouds [139]. The electronic ground state of  $\text{OH}^+$  is  $^3\Sigma^-$ . The effect of hyperfine splittings is expected to be much smaller than the bandwidth of a typical pulsed laser system due to the nuclear spins  $I = 0$  and  $I = \frac{1}{2}$  of O and H respectively. Hence the molecule is well-described by the level scheme of figure 4.4(b). The frequencies of the three laser beams required are found from equation (4.7) and the constants  $\gamma = -0.0147 \text{ cm}^{-1}$  and  $\lambda = 2.13 \text{ cm}^{-1}$  [51]. The wavelength of the un-split transition is  $3.3 \mu\text{m}$  with the three sub-transitions shifted -3.2 GHz, 0 and -12 GHz with respect to it. This splitting is too large to be covered by a single broad laser unless one finds a way to generate shorter and thereby broader and more intense pulses in this wavelength regime. This is an obvious experimental complication that will often arise in the case of  $^3\Sigma$  states due to the generally large value of the spin-spin splitting constant  $\lambda$ . It should, however, be noted that the 3 GHz may be covered by a single pulsed laser, leaving only two laser frequencies in the cooling scheme. We have calculated the dipole moment functions of  $\text{OH}^+$  and compared our results to reference [140] in figure 4.7. In the simulations, we use the function obtained in the CCSDT (aug-cc-pVTZ) calculation.

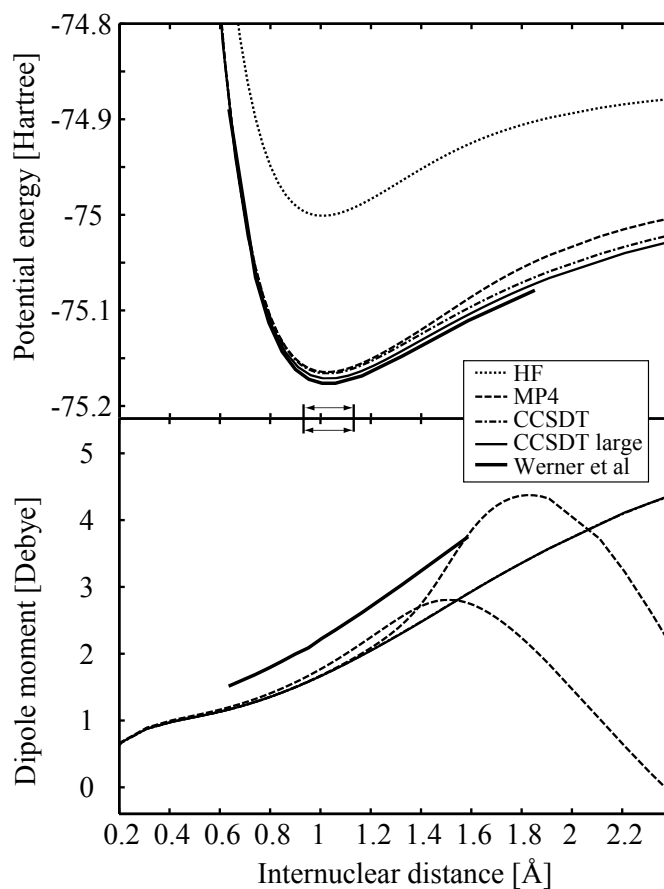


**Figure 4.7:** Top: Born-Oppenheimer potential curves for  $X^3\Sigma$   $\text{OH}^+$  calculated by *Gaussian* with various theoretical models compared to the calculation of reference [140]. All our calculations are done in a 6-311++G basis set except the solid black line which is made in the generally more accurate aug-cc-pVTZ basis [103]. The curves agree close to the equilibrium,  $1.03\text{\AA}$ , for the MP4 (Fourth order Møller-Plesset perturbation theory) and Coupled Cluster approaches (CCD, CCSDT) indicating an accurate level of theory. The different methods are described in Refs. [104–108]. Bottom: Dipole moment function calculated with *Gaussian* using similar levels of theory and basis sets. The agreement between the calculations is reasonable and the effect of using the larger basis set for the CCSDT theory is not visible on the given scale, but our results show some discrepancy with the results of reference [140]. This small discrepancy, however, has very little effect on the cooling scheme. The classical turning points for the vibrational ground state are marked on the common abscissa at  $0.95$  and  $1.15\text{\AA}$ . The dipole moment functions are given in center of mass coordinates.

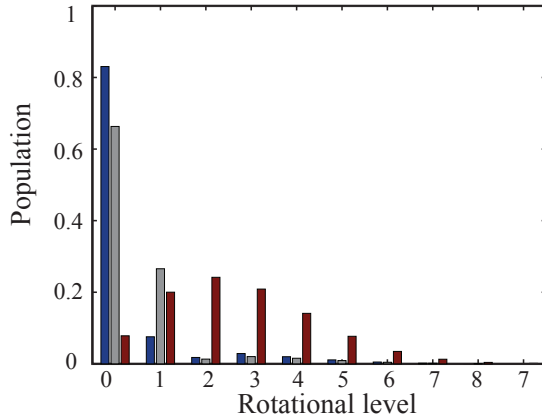


**Figure 4.8:** Population in the lowest rotational states of  $\text{OH}^+$  ( $X^3\Sigma$ ) after cooling in 10 s using the incoherent radiation from a lamp addressing the  $N = 1 \rightarrow N = 2$  and  $N = 2 \rightarrow N = 3$  transition (blue columns) and in BBR only (grey columns). The initial 300K Boltzmann distribution is included for comparison (red columns). The spin substructure of the rotational levels is included in the simulation but omitted on the figure.

The final population distribution in the numerical simulation is given in figure 4.8. The scheme is both faster and more effective than what was found for  $\text{MgH}^+$ . This can be understood from comparison of the figures 3.2 and 4.7. Recalling equation (2.20) we expect the larger gradient of the dipole moment function of  $\text{OH}^+$  to result in a higher effective pump rate from  $N = 2$  to  $N = 0$ . As with  $\text{MgH}^+$ , we see a significant increase in the cooling efficiency when introducing broadband radiation from an incoherent source to deplete the  $N = 1$  population.

The simulation shows the efficiency of the rotational redistribution in the  $^3\Sigma$  state. Considering the nonzero line strengths for transitions between the  $F_i, F_j$ , ( $i \neq j$ ) series of states, provided  $\Delta N = \pm 1$ , one could be tempted to omit one or more laser frequencies expecting rotational redistribution to empty the remaining substates by rotational transitions through neighboring  $N$ -levels. Unfortunately, such redistribution rates, requiring two or more rotational transitions through specific substates, are much too slow to have a significant effect on the cooling scheme. Therefore, each of the three laser frequencies are needed to make the cooling scheme effective. We find that the optimized distribution of incoherent radiation from a lamp addresses only the  $(\nu = 0, N = 1) \leftrightarrow (\nu = 0, N = 2)$  transition in accordance with the previous results

Finally, it should be noted that  $^{2S+1}\Sigma$ -states are always cases of pure case (b) coupling due to the vanishing orbital angular momentum and the selection

rule in  $N$  is close to exact. This stands in contrast to  $^{2S+1}\Pi$  states which often have effects of intermediate coupling which will complicate the suggested case (a) cooling scheme further.

### 4.3 Conclusion

We have presented cooling schemes for rotational cooling of translationally cold molecular ions in the  $^1\Sigma$  electronic ground state in the previous chapter and in this chapter we have expanded the scheme to the  $^2\Sigma$ ,  $^3\Sigma$  and  $^2\Pi$  electronic ground states. For all but the relatively rare  $^3\Sigma$  electronic state, the schemes can be realized by optical pumping with a single pulsed laser beam, possibly combined with the inclusion of a broad-band incoherent source. The schemes are therefore experimentally attractive and preliminary experiments are presently under way with  $\text{MgH}^+$ .



# CHAPTER 5

## Quantized Motion of Charged Particles in a Trap

In this chapter, we introduce a quantized description of translational eigenstates of charged particles in a harmonic trap. Furthermore, induced transition amplitudes between the eigenstates are discussed and notation to be used in the remainder of the thesis is established. We begin the discussion by considering a single ion in a harmonic trapping potential, followed by a generalization to several particles. Most of the qualitative features are, however, almost identical regardless of the number of ions involved.

### 5.1 A Single Ion in a Harmonic Trap

In section 2.5 we saw that the trapping potential for charged particles in a Paul trap is harmonic. We thus consider a single harmonically trapped ion in the following.

#### 5.1.1 Energy eigenstates

The total Hamiltonian of the system will be given by  $H_0 = H_{\text{ion}} + H_{\text{trap}}$ , where  $H_{\text{ion}}$  refers to the internal Hamiltonian of the ion and  $H_{\text{trap}}$  is the Hamiltonian of the external motion in the trapping potential. We may readily write the quantized Hamiltonian of the trap

$$H_{\text{trap}} = \hbar\Omega_{\text{trap}}\left(a_+a_- + \frac{1}{2}\right), \quad (5.1)$$

where  $\Omega_{\text{trap}}$  denotes harmonic trapping frequency and  $a_+$  and  $a_-$  are the step up and step down ladder operators. We denote the energy eigenstates  $|n\rangle_{\text{Tr}}$ , so  $H_{\text{trap}}|n\rangle_{\text{Tr}} = \hbar\Omega_{\text{trap}}\left(n + \frac{1}{2}\right)|n\rangle_{\text{Tr}}$ .

Let us furthermore assume that the ion has two internal states,  $|g\rangle$  and  $|e\rangle$ , i.e.,

$$H_{\text{ion}} = \hbar\omega_g |g\rangle \langle g| + \hbar\omega_e |e\rangle \langle e|, \quad (5.2)$$

where  $\omega_g$  and  $\omega_e$  denote the eigenfrequencies of the states. For most relevant transitions, the transition frequency,  $\omega_{ge} \equiv \omega_e - \omega_g$ , will be much larger than obtainable trapping frequencies in linear Paul traps.

### 5.1.2 Transition matrix elements

Consider interaction with a laser field resonant with the transition between  $|g\rangle$  and  $|e\rangle$ . The total Hamiltonian of the system is then  $H = H_{\text{trap}} + H_{\text{ion}} + H_I$ , with the interaction Hamiltonian,  $H_I$  in RWA given by

$$H_I = \frac{\hbar\Omega}{2} |e\rangle \langle g| \exp\{i[\eta(a_+ + a_-) - \omega_{ge}t]\} + c.c. \quad (5.3)$$

Here we have defined the *Lamb-Dicke-parameter*,  $\eta = k\sqrt{\hbar/(2M\Omega_{\text{trap}})}$ , with  $k$  denoting the wave number of the light field and  $M$  the mass of the trapped ion. Furthermore, we have written the rotating factor of the electromagnetic field  $e^{ikx}$  in terms of the harmonic oscillator ladder operators using  $x = \sqrt{\hbar/(2M\Omega_{\text{trap}})}(a_+ + a_-)$ .

We are interested in the transition matrix elements between quantum states,  $|g\rangle|n\rangle$  and  $|e\rangle|n'\rangle$ . By equations (5.1-5.3), the transition matrix elements are given by

$$\langle e| \langle n'|_{\text{Tr}} H |n\rangle_{\text{Tr}} |g\rangle = \frac{\hbar\Omega}{2} e^{-\omega_{ge}t} \langle n'|_{\text{Tr}} e^{i\eta(a_+ + a_-)} |n\rangle_{\text{Tr}}. \quad (5.4)$$

We proceed by investigating the matrix elements  $\langle n'|_{\text{Tr}} e^{i\eta(a_+ + a_-)} |n\rangle_{\text{Tr}}$  in two ways; a full analytical description, particularly useful for numerics, and a Taylor expansion in  $\eta$ , useful to gain physical insight.

#### Analytical expression for the transition matrix elements

We begin by writing the matrix elements in terms of the associated Laguerre polynomials [141].

As can be seen from equation (2.2), the ladder operator fulfill the commutation relation  $[a_+, [a_+, a_-]] = [a_-, [a_-, a_+]] = 0$ , which implies that we may write  $e^{i\eta(a_+ + a_-)} = e^{i\eta a_+} e^{i\eta a_-} e^{-\eta^2/2}$  [141].

We may then write the transition matrix element of equation (5.4) as

$$\begin{aligned} \langle n'|_{\text{Tr}} e^{i\eta(a_+ + a_-)} |n\rangle_{\text{Tr}} &= e^{-\eta^2/2} \langle n'|_{\text{Tr}} e^{i\eta a_+} e^{i\eta a_-} |n\rangle_{\text{Tr}} \\ &= e^{-\eta^2/2} (i\eta)^{\Delta n} \sqrt{n'!n!} \sum_m^{n_<} \frac{(-1)^m \eta^{2m}}{m!(\Delta n + m)!(n' - m)!} \\ &= e^{-\eta^2/2} (i\eta)^{\Delta n} \frac{\sqrt{n'!n!}}{n_< + \Delta n} L_{n_<}^{\Delta n}(\eta^2). \end{aligned} \quad (5.5)$$

Here,  $\Delta n = |n - n'|$  and  $n_{<} = \min(n, n')$ . Furthermore, the *associated Laguerre polynomials*,  $L_n^\alpha(x) = \sum_{m=0}^n (-1)^m \binom{n+\alpha}{n-m} \frac{x^m}{m!}$  [142] were introduced. It is now straight forward to find the entire transition matrix elements between all states in the system in the rotating wave approximation

$$\langle e | \langle n' |_{\text{Tr}} H_I | n \rangle_{\text{Tr}} | g \rangle = \frac{\hbar\Omega}{2} e^{-\eta^2/2} (i\eta)^{\Delta n} \frac{\sqrt{n'!n!}}{n_{<} + \Delta n} L_{n_{<}}^{\Delta n}(\eta^2). \quad (5.6)$$

It should be noted that these matrix elements are not equal to the free-space matrix elements between  $|g\rangle$  and  $|e\rangle$ , even if there is no change of the motional state,  $|n\rangle_{\text{Tr}}$ .

While equation (5.6) solves the problem of finding the transition matrix elements between the motional states in the trap potential for a single ion, it does not provide overwhelming physical insight. To gain a basic understanding of general features of transitions between motional states in the harmonic trapping potential, it can be useful make a Taylor expansion of the vibrational matrix elements.

### Taylor expansion of the transition matrix elements

We begin by an expansion of the vibrational transition matrix elements to third order in  $\eta$ .

$$\begin{aligned} e^{i\eta(a_+ + a_-)} &\simeq 1 + i\eta(a_+ + a_-) - \frac{1}{2}\eta^2[(a_-a_+ + a_+a_-) + a_-^2 + a_+^2] \\ &- i\frac{\eta^3}{6}(a_+^3 + a_-^3 + a_+a_-a_+ + a_-a_+a_- + a_+^2a_- + a_-^2a_+ + a_+a_-^2 + a_-a_+^2) \end{aligned} \quad (5.7)$$

Thus, by applying equation (2.4) we find the lengthy

$$\begin{aligned} e^{i\eta(a_+ + a_-)} |n\rangle_{\text{Tr}} &\simeq [1 - \frac{1}{2}\eta^2(2n+1)] |n\rangle_{\text{Tr}} \\ &+ [i\eta\sqrt{n+1} - i\frac{\eta^3}{6}\sqrt{n+1}(3n+3)] |n+1\rangle_{\text{Tr}} + [i\eta\sqrt{n} - i\frac{\eta^3}{6}3n\sqrt{n}] |n-1\rangle_{\text{Tr}} \\ &- \frac{1}{2}\eta^2\sqrt{n+1}\sqrt{n+2} |n+2\rangle_{\text{Tr}} - \frac{1}{2}\eta^2\sqrt{n^2-n} |n-2\rangle_{\text{Tr}} \\ &- i\frac{\eta^3}{6}\sqrt{(n+1)(n+2)(n+3)} |n+3\rangle_{\text{Tr}} - i\frac{\eta^3}{6}\sqrt{n(n-1)(n-2)} |n-3\rangle_{\text{Tr}}, \end{aligned} \quad (5.8)$$

from which the transition matrix elements are trivially found.

For now, we focus on the first orders in the expansion. In the limit of small  $\eta$ , denoted the *Lamb-Dicke Limit*, we see that, for single photon reactions, transitions without change of vibrational quanta (carrier transitions) are dominant, followed by transitions between  $|n\rangle_{\text{Tr}}$  and  $|n \pm 1\rangle_{\text{Tr}}$  (first sideband)<sup>1)</sup>. Furthermore it is noticed that excitations of more than one vibrational quantum will

<sup>1)</sup>Interference between reaction channels can make higher-order transitions dominant in a Raman process as discussed in section 7.3

be increasingly likely with higher initial excitation. These fundamental features are a cornerstone of a number of proposals and experiments in sideband cooling, discussed in section 2.6, and quantum optics with trapped ions [143, 144]. We will later see that they can be used to derive a method for state preparation of molecular ions in an ion trap.

## 5.2 Strings of Ions in a Trap

The main advantage of utilizing ion traps to study and control molecular ions is the effective sympathetic cooling of the external motion of the molecular ions. The expressions of the previous section need to be generalized to more than one ion in a trap in order to take advantage of the sympathetic cooling on the level of quantized motion in the trap. We begin by deriving equilibrium positions of the ions and eigenfrequencies of the collective vibrational motion in the trap.

### 5.2.1 Equilibrium positions and vibrational modes

We focus on ions on a string, which is later to be restricted to a string consisting of one atomic and one molecular ion. The potential energy of a string of  $N$  ions of mass  $M_m$ ,  $m = 1 \dots N$  in a confining electrostatic potential of  $\phi = \phi_0 \frac{q}{2} x^2$  is given by [145, 146]

$$V = \sum_{m=1}^N \phi_0 \frac{q}{2} x_m^2 + \sum_{m \neq l}^N \frac{q^2}{8\pi\epsilon_0} \frac{1}{|x_m - x_l|}. \quad (5.9)$$

Here,  $x_m$  denotes the position of particle  $m$  and the ions are assumed to have identical charge  $q$ , while  $\phi_0$  is a constant given by the strength of the confining potential, cf. section 2.5. The equilibrium positions of the ions in the confining potential can then be found by minimizing equation (5.9) with respect to  $x_l$ .

After Doppler cooling of the ions, the displacement of the ions from the equilibrium positions is small, so we may write  $x_m = x_m^0 + q_m(t)$ , where  $x_m^0$  is the equilibrium position of the  $m$ th ion and  $|q_m(t)| \ll |x_{m+1}^0 - x_m^0|$ . The ions are numbered as  $m = 1 \dots N$  with the ion being molecular with mass  $M_{\text{mol}}$  if  $m \in \mathfrak{M}$  and an atomic ion with mass  $M_{\text{atom}}$  if  $m \in \mathfrak{A}$ . Thus we have assumed a two component crystal of molecules and atoms. Following James and Kielpinski [145, 146], we now use the second order expansion of the potential around the

equilibrium positions to write an approximate expression for the Lagrangian,

$$\begin{aligned}
 L &\approx \frac{1}{2} \sum_{m=1}^N M_m \dot{q}_m^2 - \frac{1}{2} \sum_{m,l=1}^N q_m q_l \left( \frac{\partial^2 V}{\partial x_m \partial x_l} \right) \\
 &= \frac{1}{2} \sum_{m=1}^N M_m \dot{q}_m^2 - \frac{1}{2} \phi_0 q \sum_{m,n=1}^N A_{n,m} q_n q_m \\
 &= \frac{1}{2} \sum_{m=1}^N \left( \frac{dQ_m}{dT} \right)^2 - \frac{1}{2} \sum_{m,n=1}^N A'_{n,m} Q_n Q_m.
 \end{aligned} \tag{5.10}$$

Where we used that the equilibrium positions minimize the potential, resulting in a vanishing linear term in the Taylor expansion, and then neglected the constant term. Furthermore, we defined

$$A_{n,m} = \begin{cases} 1 + 2 \sum_{p \neq m}^N \frac{1}{|u_m - u_p|^3} & \text{if } n = m \\ \frac{-2}{|u_m - u_n|^3} & \text{if } n \neq m, \end{cases}$$

with  $u_m = x_m^0 / \sqrt[3]{q/4\pi\epsilon_0\phi_0}$ , and evaluated the quadratic term in the expansion of the potential. In writing the final expression of equation (5.10), we introduced  $\mu = \frac{M_{\text{mol}}}{M_{\text{atom}}}$ , the normalized time,  $T = \sqrt{\phi_0 q / M_{\text{atom}}} t$ , and the normalized displacement coordinates,  $Q_m = q_m \sqrt{\phi_0 q}$ . The matrix  $A'_{n,m}$  is then given by

$$A'_{n,m} = \begin{cases} A_{n,m} & \text{if } n, m \in \mathfrak{A} \\ \frac{A_{n,m}}{\sqrt{\mu}} & \text{if } n \in \mathfrak{M}, m \in \mathfrak{A} \vee m \in \mathfrak{M}, n \in \mathfrak{A} \\ \frac{A_{n,m}}{\mu} & \text{if } n, m \in \mathfrak{M}. \end{cases}$$

We find the eigenmodes of collective vibrations expressed in terms of  $Q_m$  by diagonalizing  $A'$ . Define the eigenvectors and -energies by  $A' \mathbf{v}_k = \xi_k^2 \mathbf{v}_k$ , where  $\mathbf{v}_k$  are properly normalized. Now, by expanding  $Q_m$  on the eigenvectors  $\mathbf{v}_k$  we may write the Lagrangian of equation (5.10) in the basis of the eigenmodes, in which case it takes the form

$$L = \frac{1}{2} \sum_{p=1}^N \left( \frac{dQ'_p}{dT} \right)^2 - \frac{1}{2} \sum_{p=1}^N \xi_p^2 Q_p'^2, \tag{5.11}$$

where  $Q'_k = \mathbf{v}_k \cdot \mathbf{Q}$ .

Equation (5.11) is immediately recognized as the Lagrangian of a superposition of  $N$  harmonic oscillators with frequencies  $\xi_p$  and unit mass. We may then proceed to the quantization of the vibrational motion following a procedure similar to the quantization of the one-dimensional harmonic oscillator presented in section 2.1.

### 5.2.2 The quantized vibrational motion

From equation (5.11), the Hamiltonian of the system is found to be

$$H = \frac{1}{2} \sum_{p=1}^N (P_p)^2 + \frac{1}{2} \sum_{p=1}^N \xi_p^2 Q_p'^2, \quad (5.12)$$

with the  $P_p$  being the canonical momentum conjugate to  $Q_p'$ , i.e.  $P_p = \dot{Q}_p'$ . We make the operator substitution  $P_p \rightarrow -i\frac{d}{dQ_p'}$  and find  $[Q_p', P_q] = i\delta_{pq}$ . Defining ladder operators  $a_{\pm}^p = \frac{1}{\sqrt{2}}(\sqrt{\xi_p}Q_p' \mp \frac{iP_p}{\sqrt{\xi_p}})$  we find

$$H = \sum_p \xi_p (a_+^p a_-^p + \frac{1}{2}) \quad (5.13)$$

$$[a_-^p, a_+^q] = \delta_{pq}.$$

As expected, the quantized Hamiltonian is a superposition of independent harmonic oscillator Hamiltonians. The physical eigenfrequencies of the vibrational modes are found by transforming  $T \rightarrow t$  giving  $\Omega_p = \xi_p \Omega_{\text{trap}}$ . Similarly, the physical position coordinates of the ions can be found by transforming  $Q_p' \rightarrow q_m$ .

We can now recycle much of the formulations in the previous section in order to evaluate the transition matrix elements.

### 5.2.3 Transition matrix elements

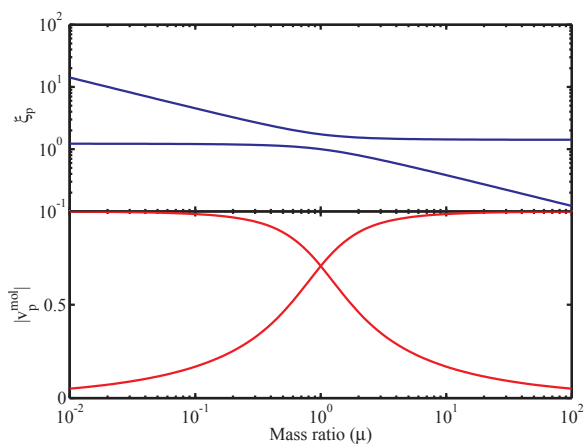
For a monochromatic laser field of frequency  $\omega$  resonant with the  $i$ th ion with free ion Rabi frequency,  $\Omega_{\text{Rabi}}$ , the transition matrix elements from  $|g\rangle |\nu\rangle_p$  to  $|e\rangle |\nu'\rangle_p$  are

$$\frac{\hbar}{2} \Omega_{\text{Rabi}} \prod_p \left\{ \langle \nu' | \nu \rangle_p e^{i(kx - \omega t)} \right\}. \quad (5.14)$$

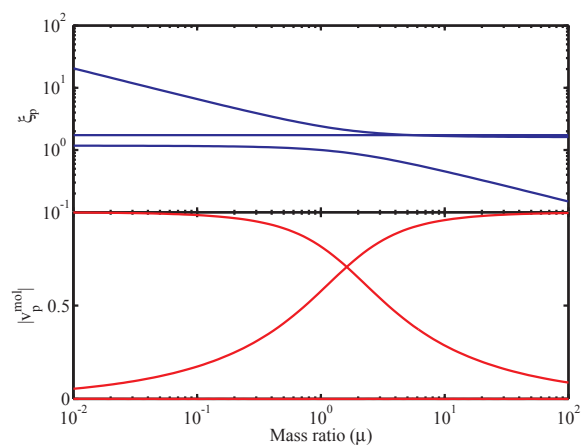
From the definition of the ladder operators,  $\frac{1}{\sqrt{2\xi_p}}(a_-^p + a_+^p) = Q_p' = \sum_{m=1}^N \mathbf{v}_p^m \mathbf{q}$ , where  $\mathbf{q}$  is the vector of ion displacements and  $v_p^m$  is the  $m$ th component of  $\mathbf{v}_p$ . Multiplying by the  $i$ th component of  $\mathbf{v}_p$ , summing over vibrational modes and using orthonormality of eigenvectors it is found that  $q_i = \sum_p v_p^i \frac{1}{\sqrt{2\xi_p}}(a_-^p + a_+^p)$ .

Transforming back to the physical coordinates, the matrix elements can be written

$$\frac{\hbar}{2} \Omega_{\text{Rabi}} e^{ikx_0} \prod_p \langle \nu' | \nu \rangle_p \exp \left\{ i \left[ \sum_{p'} \eta_p^i (a_+^{p'} + a_-^{p'}) \right] - \omega t \right\} | \nu \rangle_p, \quad (5.15)$$



(a) 2 ions



(b) 3 ions

**Figure 5.1:** Blue lines: Normalized mode eigenfrequencies,  $\xi_p$ , for two and three ions in a harmonic trap as function of the mass ratio,  $\mu$ , between two particle species. Results are given for **a)** two ions and **b)** three ions. The mass ratio is defined  $\mu = \frac{M_{\text{mol.}}}{M_{\text{atom}}}$ , where the second ion in the chain for both two and three ions is assumed to have mass  $M_{\text{mol}}$  and the remaining particle(s) are assumed to have mass  $M_{\text{atom}}$ . The red lines show the second component of the normalized mode eigenvectors, thus illustrating the amplitude of translational motion of the molecular ion as function of  $\mu$ .

where we introduced  $\eta_p^i = k\sqrt{\hbar/(2M_i\xi_p\Omega_{\text{trap}})}v_p^i$ . Thus, the transition matrix elements have been written as a product of  $N$  independent matrix elements – the same form as the single ion matrix elements derived in equation (5.6), albeit with a modified Lamb-Dicke parameter. The analogy to the single trapped ion is thus completed, and it has been shown that for ions on a string, the structure of energy levels as well as optical transition matrix elements can be treated as a series of  $N$  harmonic oscillators, greatly reducing the complexity of the problem.

The importance of the vibrational states in the trap being collective cannot be overestimated. The Hamiltonian of the system cannot be written as a sum of *single-particle* Hamiltonians, and translational excitation of one ion will therefore be accompanied by translational excitations of the other ions in the chain. A motional sideband transition on a molecular ion is therefore also a sideband transition for a simultaneously trapped atomic ion, a phenomenon we will use in two proposals in the following chapters.

In chapter 6, we propose to excite the collective vibrational motion by a Raman transition in a molecule, followed by Doppler cooling of the collective vibrational state through the atomic ion. The technique will be shown to cool the molecule despite of the absence of a dissipative process in the molecular transition. The necessary dissipative process is, of course, the well known Doppler cooling of the atomic ion.

In chapter 7, we show that selective sideband transitions in the molecule, followed by a detection of the collective motional state by the shelving technique on the atomic ion allows state preparation of molecular ions through the projection measurement. The technique requires sub-Doppler cooling and will only work for a single molecular ion at a time. There are, however, very few constraints on the size, structure and dynamics of the molecular ion so the scheme is very versatile.



# CHAPTER 6

## Internal Cooling of Molecules Through Atomic Cooling Cycles

In the previous chapter, we investigated aspects of the motion of simultaneously trapped ions. In particular, we saw that the motion of the ions can be described as independent modes of collective motion in a harmonic trap. In this chapter, we will use the collective character of the motion to propose a new cooling scheme for molecular ions. The cooling scheme is based on coupling of the molecular internal state to the collective motional state with a Raman transition. The atomic cooling cycles, damping the collective motion in the trap potential, will then be shown to cool the internal molecular state indirectly under appropriate conditions on the molecular Raman transitions. In contrast to the cooling schemes presented in chapter 3 and 4, the present cooling scheme does not rely on spontaneous transitions in the molecular ion and, consequently, the scheme is independent of molecular vibrational structure and dynamics and thus applicable to a larger variety of molecules, including polyatomic molecules.

### 6.1 Sympathetic Cooling of the Axial Modes

We consider the motion of a laser cooled atomic ion and a sympathetically cooled molecular ion along one dimension of a harmonic trap with frequency  $\Omega_{\text{trap}}$ . We assume that the dynamics of the ions in the two other dimensions of the trap is decoupled from the motion considered here, thereby reducing the system to one dimension. In section 5.2 we saw that the equation motion can be written as a sum of two independent harmonic oscillator equations, each representing a mode of collective motion in the trap. We will denote the modes the center of mass (CM) mode and the breathing (BR) mode, with  $|\nu_{\text{CM}}\rangle$  and the  $|\nu_{\text{BR}}\rangle$  being the corresponding motional states.

In the following, the the system is assumed cooled to the Doppler limit. In section 2.6.1 we found the semiclassical expression for the Doppler cooling rate of an atom, which can be written  $\dot{E} = -\frac{4\alpha}{M_{\text{at}}}\langle E_{\text{kin}}\rangle$ . Here  $M_{\text{at}}$  denotes the atomic mass,  $\langle E_{\text{kin}}\rangle$  the mean kinetic energy of the atom and  $\alpha$  is defined in section 2.6.1. The Doppler cooling thus work as a function of the kinetic energy of the atom. For the two component ion string, it is necessary to evaluate the Doppler cooling rate of each of the axial modes separately, since the kinetic energy of the atom will depend on both the collective mode and the mass ratio,  $\mu$ . The Doppler cooling rate will depend on the mean kinetic energy of the atom,  $\langle E_{\text{kin}}^{\text{atom}}\rangle$ , only. That is,  $\dot{E} = -\frac{4\alpha}{M_{\text{at}}}\langle E_{\text{kin}}^{\text{atom}}\rangle$ . Using equation (5.12) and taking appropriate advantage of  $Q'_p$  and  $P_p$ , an expression for the kinetic energy of the atom is found,

$$\langle E_{\text{kin}}^{\text{atom}}\rangle = \frac{1}{2}\hbar\Omega_{\text{trap}}\sum_p(\nu_p + \frac{1}{2})v_{\text{at}}^{p2}\xi_p. \quad (6.1)$$

Here,  $v_{\text{at}}^p$  denotes the component of the  $p$ th eigenvector  $\mathbf{v}^1$ ) corresponding to the atom, and the summation is over the collective modes,  $p = BR, CM$ . Combining equation (6.1) with the expression for the total energy of the system we find a differential equation for the motional quanta,  $\nu_p$ ,

$$\dot{\nu}_p^{\text{cool}} = -\frac{\alpha}{M_{\text{at}}}v_{\text{at}}^{p2}(\nu_p + \frac{1}{2}). \quad (6.2)$$

We evaluate the laser heating rate in the same way as in section 2.6.1, but assuming that the photon energy is divided equally between the axial modes. We find

$$\dot{\nu}_p^{\text{Heat}} = \hbar k_z^2 \frac{\gamma_{\text{atom}}}{NM_{\text{at}}\xi_p\Omega_{\text{trap}}}\frac{s}{s+1}. \quad (6.3)$$

Here,  $\gamma_{\text{atom}}$  is the linewidth of the atomic transition,  $s$  is the saturation parameter,  $k_z$  is the wave number of the incident photons and  $N = 2$  accounts for the momentum being distributed over the motional modes of the ion string. The equilibrium vibrational state of the  $p$ th mode,  $\bar{\nu}_p$ , is found from equation (6.2) and (6.3). We find a Doppler cooling limit of  $\bar{\nu}_p^{\text{min}} = \frac{\gamma_{\text{atom}}}{2N\xi\Omega_{\text{trap}}v_{\text{at}}^{p2}} - 0.5$ , which should be compared to the single ion doppler cooling limit  $\bar{\nu}_{\text{single ion}}^{\text{min}} \simeq \frac{\gamma_{\text{atom}}}{2\Omega_{\text{trap}}}$ . We note that for the two-component ion chain, the equilibrium motional state decreases with increasing  $v_{\text{at}}^p$ , i.e. the collective temperature decrease when the amplitude of the atomic motion increase. This is not unexpected from the theory of Doppler cooling, since the cooling mechanism is represented by a friction term on the atomic ion only. The factor of  $\frac{1}{N}$  in the expression for the equilibrium motional state of the ion chain accounts for the mean energy being split between two motional modes.

The motional redistribution rates,  $\{\Gamma_{\text{atom}}\}$ , are found by converting equation (6.2) and (6.3) to discrete equations for the motional states.  $\{\Gamma_{\text{atom}}\}$  thus rep-

<sup>1)</sup>See section 5.2.1 for definitions of  $\mathbf{v}$  and  $\xi_p$

resent the equation of motion for the motional states in the trap as a result of cooling with Doppler lasers.

## 6.2 Internal Cooling

The cooling concept is illustrated in figure 6.1. In addition to the states of collective motion in the trap discussed above, the cooling scheme involves the molecular electronic ground state,  $|g\rangle_{\text{mol}}$ , an optically accessible excited electronic state of the molecule,  $|e\rangle_{\text{mol}}$ , and a number of rotational sub-states of the electronic molecular states,  $|J\rangle_{\text{rot}}$ , with  $J$  being the rotational quantum number. We assume that the state of the system can be written as a product of these molecular states and the states of collective motion in the trap,  $|\Psi\rangle = |\psi_{\text{el}}\rangle_{\text{mol}} |J\rangle_{\text{rot}} |\nu_{\text{CM}}\rangle |\nu_{\text{BR}}\rangle$ ,  $\psi_{\text{el}} = (e, g)$ .

Since  $\frac{BJ(J+1)}{\hbar} \equiv \omega_{\text{rot}} \gg \bar{\nu}_i \Omega_i$ ,  $B$  being the rotational constant of the molecule, the system can be considered a collection of rotational molecular states with sub-states of collective motion in the trap. These external motional states of one of the modes are shown in figure 6.1 as solid horizontal lines and the molecular part of the wave-function is also indicated on the figure. The molecular rotational energy levels decouple from the motional states in the trap without the application of an explicit coupling mechanism, as explained in section 2.6.3, and the total population is therefore distributed over rotational levels as a Boltzmann distribution at room temperature. The equilibrium distribution of population for the lowest rotational states is schematically depicted as a filled blue area plot superimposed on the states in figure 6.1 with the total area in each of the molecular rotational states proportional to the population in that state. The atomic Doppler cooling rates between motional states in the trap,  $\{\Gamma_{\text{atom}}\}$ , result in an equilibrium distribution over external motional levels in the trap potential with a temperature in the mK regime, in contrast to the room temperature distribution over rotational levels. The distribution of population over the motional sub-states is thus peaked at a low quantum number as shown in the figure.

Coupling between the external modes and the internal rotations of the molecule is achieved by addressing states,  $|\Psi_i\rangle = |g\rangle_{\text{mol}} |J=2\rangle_{\text{rot}} |\nu_{\text{CM}}\rangle |\nu_{\text{BR}}\rangle$ , with a Raman transition which couples to  $|\Psi_f\rangle = |g\rangle_{\text{mol}} |J=0\rangle_{\text{rot}} |\nu'_{\text{CM}}\rangle |\nu'_{\text{BR}}\rangle$  with  $\nu'_i > \nu_i$  ( $i = \text{CM}, \text{BR}$ ) via the excited electronic molecular state,  $|\Xi_m\rangle = |e\rangle_{\text{mol}} |1\rangle_{\text{rot}} |\nu''_{\text{CM}}\rangle |\nu''_{\text{BR}}\rangle$ . If we choose the Raman transition resonant with  $\nu'_i - \nu_i \gg \bar{\nu}_i$ , where  $\bar{\nu}_i$  is the mean quantum number of the  $i$ th collective mode, the population in  $|J=2\rangle_{\text{rot}}$  can be transferred to high-lying external states in  $|0\rangle_{\text{rot}}$ . Population within the equilibrium distribution over motional states with  $|0\rangle_{\text{rot}}$  can, however, not be transferred to  $|2\rangle_{\text{rot}}$  as the Raman transition will be detuned below the motional ground state  $|g\rangle_{\text{mol}} |2\rangle_{\text{rot}} |\nu_{\text{CM}}=0\rangle |\nu_{\text{BR}}=0\rangle$ . We then conclude that population transferred from  $|2\rangle_{\text{rot}}$  to  $|0\rangle_{\text{rot}}$  will relax to the equilibrium distribution over motional levels in  $|0\rangle_{\text{rot}}$  from where it cannot be transferred back to  $|2\rangle_{\text{rot}}$ . We have then established unidirectional pumping between the two molecular states where the only dissipative term originates in the spontaneous

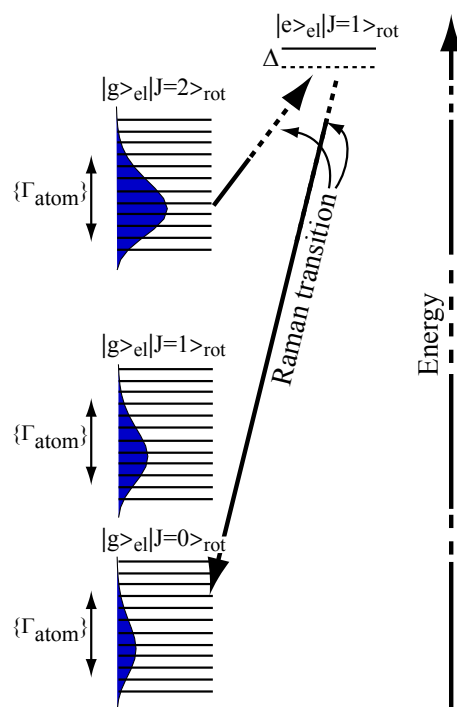


**Figure 6.1:** The proposed scheme is based on a Raman transition between two rotational states of the molecule,  $|J = 2\rangle_{\text{rot}}$  and  $|J = 0\rangle_{\text{rot}}$ , both in the molecular electronic ground state,  $|g\rangle_{\text{mol}}$ . The sub-states of collective motion in the trap potential are depicted as solid horizontal lines. The equilibrium distribution without molecular cooling is a Boltzmann distribution over the sub-states of collective motion with mK temperature superimposed on a distribution over rotational levels at room temperature as explained in the text. The resulting distribution without molecular cooling is schematically shown as a blue area plot with the population along the horizontal axis. The Raman laser is chosen to be resonant with states of collective motion in  $|J = 2\rangle_{\text{rot}}$  and higher-lying motional states in  $|J = 0\rangle_{\text{rot}}$  via an excited electronic state of the molecule  $|e\rangle_{\text{mol}}$  with detuning  $\Delta$ . It should be noted, that the continuous distribution depicted in the blue area plot is schematic only. The physical distribution is, of course, discrete.

decay of the atomic cooling cycle. We have previously shown that with unidirectional pumping established, Black-body-radiation (BBR) can be used to cool the remaining rotational degrees of freedom in the molecule, cf. chapter 3 and 4. Unfortunately, the coupling matrix elements for  $\nu'_i - \nu_i \gg \bar{\nu}_i$  are extremely small under realistic conditions. We will thus, through numerical simulations, show that effective unidirectional pumping is possible with  $\nu'_i - \nu_i \sim \bar{\nu}_i$ . The coupling matrix elements are maximized if the lasers in the Raman process are

chosen counterpropagating to ensure maximal momentum transfer.

The scheme can be represented by a rate equation,  $\frac{d\mathbf{P}}{dt} = K\mathbf{P}$ , where  $\mathbf{P}$  is a vector with population in the states  $|g\rangle_{\text{mol}} |J\rangle_{\text{rot}} |\nu_{\text{CM}}\rangle |\nu_{\text{BR}}\rangle$  and  $K$  is a coupling matrix determined by  $\{\Gamma_{\text{atom}}\}$  and the set of coupling rates between internal molecular states and external motion in the trap,  $\{\Gamma_{\text{mol}}\}$ .  $\{\Gamma_{\text{atom}}\}$  was evaluated in the previous section, but it remains to evaluate  $\{\Gamma_{\text{mol}}\}$ . Define the interaction Hamiltonian,  $V = \mathbf{d} \cdot \mathbf{E}_1(x, t) + \mathbf{d} \cdot \mathbf{E}_2(x, t) = \frac{1}{2}V^{(1)}(e^{ik_1\hat{x}} + e^{-ik_1\hat{x}}) + \frac{1}{2}V^{(2)}(e^{ik_2\hat{x}} + e^{-ik_2\hat{x}})$  with  $\mathbf{d}$  the dipole operator and  $\mathbf{E}_l(x, t)$  the electric field from laser  $l = (1, 2)$  with frequency  $\omega_l$  and wave number  $k_l$ . Assume  $\omega_1 + \Delta$  resonant with the molecular transition  $|g\rangle_{\text{mol}} |2\rangle_{\text{rot}} \rightarrow |e\rangle_{\text{mol}} |1\rangle_{\text{rot}}$  and  $\omega_2 + \Delta$  resonant with the molecular transition  $|e\rangle_{\text{mol}} |1\rangle_{\text{rot}} \rightarrow |g\rangle_{\text{mol}} |0\rangle_{\text{rot}}$ . The transition rate from an initial state,  $|\Psi_i\rangle = |g\rangle_{\text{mol}} |2\rangle_{\text{rot}} |\nu_{\text{CM}}\rangle |\nu_{\text{BR}}\rangle$ , to a final state,  $|\Psi_f\rangle = |g\rangle_{\text{mol}} |0\rangle_{\text{rot}} |\nu'_{\text{CM}}\rangle |\nu'_{\text{BR}}\rangle$ , via a collection of intermediate states,  $|\Xi_m\rangle = |e\rangle_{\text{mol}} |1\rangle_{\text{rot}} |\nu''_{\text{CM}}\rangle |\nu''_{\text{BR}}\rangle$ , when interacting through  $V_I$  is then given by

$$\Gamma_{i \rightarrow f} = \frac{1}{4\hbar^4} \left| \sum_m \frac{\langle \Psi_f | V_I^{(2)} e^{-ik_2\hat{x}} |\Xi_m\rangle \langle \Xi_m | V_I^{(1)} e^{ik_1\hat{x}} |\Psi_i\rangle}{\frac{E_m - E_i}{\hbar} - \omega_1 - \frac{1}{2}i\gamma_m} \right|^2 \mathcal{L}(\Gamma, \delta), \quad (6.4)$$

where  $E_i$ ,  $E_m$  and  $E_f$  denote the energy of  $|\Psi_i\rangle$ ,  $|\Xi_m\rangle$  and  $|\Psi_f\rangle$ , respectively.  $\gamma_m$  is the line width of the intermediate state and we have applied RWA by ignoring far off-resonant terms. Furthermore, a Lorentzian,  $\mathcal{L}(\Gamma, \delta) = \frac{1}{\pi} \frac{\Gamma}{\delta^2 + \Gamma^2}$  with  $\delta = \omega_1 - \omega_2 - \frac{E_f - E_i}{\hbar}$  has been used in order to describe the effect of a laser with bandwidth  $\Gamma$ . The expression can be simplified by denoting  $\Omega_{\text{mol}_l}^\pm = \frac{1}{\hbar} \langle e |_{\text{mol}} \langle J = 1 |_{\text{rot}} V_I^{(l)} | J = 1 \pm 1 \rangle_{\text{rot}} | g \rangle_{\text{mol}}$  and extracting it from the sum. In RWA we find

$$\Gamma_{i \rightarrow f} = \frac{1}{4} |\Omega_{\text{mol}_2}^+|^2 |\Omega_{\text{mol}_1}^-|^2 \left| \sum_{\nu''_{\text{CM}}, \nu''_{\text{BR}}} \prod_{i=(\text{CM}, \text{BR})} \frac{\langle \nu'_i | e^{-ik_2\hat{x}} |\nu''_i\rangle \langle \nu''_i | e^{ik_1\hat{x}} |\nu_i\rangle}{\frac{E_m - E_i}{\hbar} - \omega_1 - \frac{1}{2}i\gamma_m} \right|^2 \mathcal{L}(\Gamma, \delta). \quad (6.5)$$

$|\Omega_{\text{mol}_l}^\pm|^2$  can be expressed in terms of the Einstein A coefficient between the molecular states and the intensity and frequency of laser  $l$ . All other molecular coupling matrix elements are expected to be negligible from selection rules. It remains to calculate the transition matrix elements between collective motional states in the trap.

The transition matrix elements  $\langle \nu'_i | e^{-ik_2\hat{x}} |\nu''_i\rangle$  and  $\langle \nu''_i | e^{ik_1\hat{x}} |\nu_i\rangle$  can be written in terms of the generalized Laguerre polynomials,  $L_n^\alpha(x)$ , and the Lamb-Dicke parameter, as demonstrated in section 5.2. Equation (6.5) can then be evaluated numerically for a given number of included motional states.

The computational task can be made considerably less demanding by making approximations as follows. The eigenenergies of  $|\Xi_m\rangle$  are given by  $E_m = \hbar\omega_{ge} + \hbar\Omega_{\text{CM}}(\nu''_{\text{CM}} + \frac{1}{2}) + \hbar\Omega_{\text{BR}}(\nu''_{\text{BR}} + \frac{1}{2})$ , where  $\omega_{ge}$  denotes the free molecule transition frequency. For reasonable detuning from the excited electronic molecular state,

$\Omega_{CM}(\nu''_{CM} + \frac{1}{2}) + \Omega_{BR}(\nu''_{BR} + \frac{1}{2}) \ll \omega_{ge} - \omega_1$ . Furthermore, we assume that the linewidth of  $|\Xi_m\rangle$  is independent of the motional excitations, i.e.  $\gamma_m \simeq \gamma$ . Under these assumptions, the denominator in equation (6.5) is independent of  $m$ . We may then use completeness of the collective motional states,  $\sum_{\nu_p} |\nu_p\rangle \langle \nu_p| = 1$ , to completely eliminate the sum over intermediate states, thus reducing equation (6.5) to

$$\Gamma_{i \rightarrow f} = \frac{1}{4} |\Omega_{\text{mol}_2}^+|^2 |\Omega_{\text{mol}_1}^-|^2 \left| \prod_{i=(CM, BR)} \frac{\langle \nu'_i | e^{ik_1 x - ik_2 \hat{x}} | \nu_i \rangle}{\Delta - \frac{1}{2} i \gamma} \right|^2 \mathcal{L}(\Gamma, \delta). \quad (6.6)$$

Here,  $\Delta = \omega_{ge} - \omega_1$  denotes the single photon detuning from the intermediate state.

With the molecular-motional transition rates,  $\{\Gamma_{\text{mol}}\}$ , established through equation (6.5) or (6.6) and the previously used transition rates for BBR-induced transitions, we proceed to numerical simulations.

First, we will present numerical simulations of  $\text{MgH}^+$  trapped with  $^{40}\text{Ca}^+$  using an excited electronic state as intermediate state in the Raman transition. This will establish a basic proof of principle for the cooling scheme. Thereafter, we will discuss the parameters of the simulation, as they turn out to be problematic. Methods to circumvent the problems are then proposed and some preliminary results are given.

### 6.3 Numerical Simulations

We have simulated the cooling scheme of figure 6.1 for  $\text{MgH}^+$  and  $^{40}\text{Ca}^+$  using  $\Omega_{\text{trap}} = 50$  MHz and evaluated the transition rates in both equation (6.5) and (6.6) with  $\nu_i, \nu'_i, \nu''_i = 0 \dots 40, i = (\text{CM}, \text{BR})$ . The oscillation frequencies of the two external modes are  $\Omega_{\text{CM}} \simeq 50$  MHz and  $\Omega_{\text{BR}} \simeq 100$  MHz. We use the linewidth and transition frequencies of the primary doppler cooling transition in  $^{40}\text{Ca}^+$ , shown in figure 2.9. The Rabi frequency of the atomic cooling transition is chosen to 50 MHz. The lasers in the Raman process were tuned to resonance when  $\nu'_i - \nu_i = 2$ . The coupling rate  $\Omega_{\text{mol}_i}^\pm$  was chosen to 3 GHz for both transitions and the detuning from the excited state was 750 GHz. The width of the Lorentz function was chosen to  $\Gamma = 1$  KHz, and the Raman coupling lasers were assumed pulsed width 1 ms pulse length. The Lorentz function was cut off 70 MHz from the center frequency in the numerical simulations.

The initial distribution over collective motional states was the equilibrium distribution resulting from  $\{\Gamma_{\text{atom}}\}$  alone, while the molecule was assumed to be in  $|2\rangle_{\text{rot}}$ . We propagated the rate equations with this initial distribution of population for 1 ms. This corresponds to solving a system of 3362 coupled differential equations which took  $\sim 8$  minutes on a 3.2 GHz Pentium 4 system.

Population distributions at representative times during cooling are depicted in figure 6.2 together with the corresponding distribution without Raman coupling. We see that the Raman transition results in effective population transfer

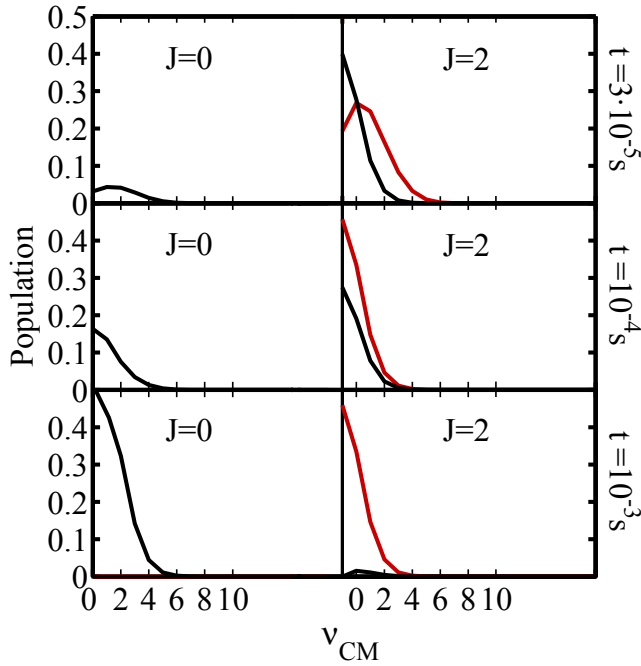


**Figure 6.2:** Population distribution in the CM mode of collective motion in the trap potential at representative times during cooling. Population in  $|0\rangle_{\text{rot}}$  is shown in the left half, while population in  $|2\rangle_{\text{rot}}$  is depicted in the right. The simulation was started with the entire population in  $|2\rangle_{\text{rot}} |\nu_{\text{CM}} = 40\rangle |\nu_{\text{BR}} = 40\rangle$ . Red lines depict distributions without the Raman transition shown in figure 6.1, while black lines represent population distributions with the Raman transition. Results for the BR mode are very similar, except the equilibrium distribution is shifted to the left due to the higher eigenfrequency of this mode.

from the initial  $|2\rangle_{\text{rot}}$  molecular state to  $|0\rangle_{\text{rot}}$ . We fit the evolution of population to the solution of a system of two coupled differential equations corresponding to an effective pumping rate,  $\gamma_{\text{cool}}$ , pumping from  $|2\rangle_{\text{rot}}$  to  $|0\rangle_{\text{rot}}$  and another effective rate,  $\gamma_{\text{heat}}$ , representing heating from  $|0\rangle_{\text{rot}}$  to  $|2\rangle_{\text{rot}}$ . This gives a near-perfect fit with  $\gamma_{\text{cool}} = 5.3 \cdot 10^3 \text{ s}^{-1}$  and  $\gamma_{\text{heat}} = 0.18 \cdot 10^3 \text{ s}^{-1}$ , hence the effective rate model accurately describes the cooling mechanism. The data and fits are shown in figure 6.3 when using both equation (6.5) and (6.6) to evaluate  $\{\Gamma_{\text{mol}}\}$ . The two equations give essentially the same result, leading us to conclude that equation (6.6) is an adequate description of the process <sup>2)</sup>.

The rates  $\gamma_{\text{cool}}$  and  $\gamma_{\text{heat}}$  are now used to propagate rate equations representing a system of the lowest 12 rotational states of  $\text{MgH}^+$  when interacting with the

<sup>2)</sup>While the two methods give very similar results, equation (6.5) takes approximately ten hours to evaluate for the given parameters, while (6.6) takes less than three minutes.

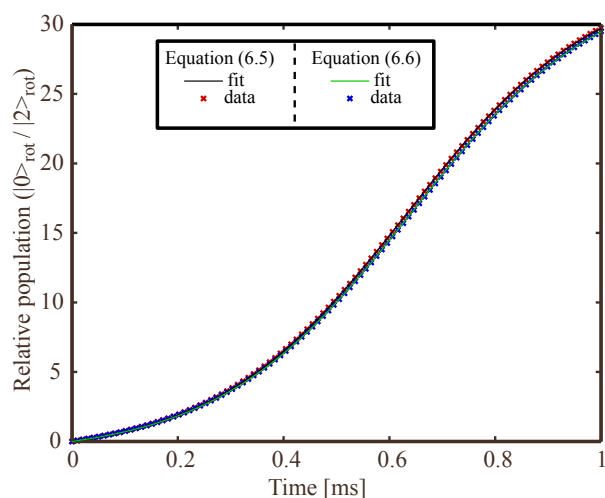


**Figure 6.3:** Relative population in  $|0\rangle_{\text{rot}} / |2\rangle_{\text{rot}}$  during the 1 ms Raman pulse when the molecule is assumed to be in  $|2\rangle_{\text{rot}}$  at time  $t = 0$ . Red marks represent simulated data using equation (6.5) and black line shows a fit to these data points. Blue markers show simulated data when calculating  $\{\Gamma_{\text{atom}}\}$  using equation (6.6) and the green line represents a fit to these data points. The two equations are seen to give essentially the same result, and the quality of the fits is equally convincing.

300 K BBR field present in the trap and subject to the presented cooling mechanism. The result of these simulations is shown in figure 6.4. The simulation is performed with continuous pumping, which is a good approximation provided the repetition frequency of the Raman lasers is much faster than the BBR rotational redistribution rate.

The  $J = 2$  level is emptied immediately due to the comparatively large  $\gamma_{\text{cool}}$ . The remaining rotational levels of the molecule are redistributed due to transitions mediated by BBR and spontaneous decays. After  $\sim 60$  s just above 60 % of the distribution is found in the ground state. The only excited rotational state, which is not emptied by  $\gamma_{\text{cool}}$  and BBR induced rotational redistribution, is  $|1\rangle_{\text{rot}}$ . This is explained as rotational heating from the highly populated  $|0\rangle_{\text{rot}}$  in the presence of BBR at a timescale so fast that rotational heating from  $|1\rangle_{\text{rot}}$  to  $|2\rangle_{\text{rot}}$  cannot compensate. This effect can be somewhat reduced by the introduction of tailored incoherent fields [96]. Even without the use of such fields we notice that more than 80 % of the total population is in the two lowest rotational states, roughly corresponding to a rotational temperature of  $\sim 8$  K.



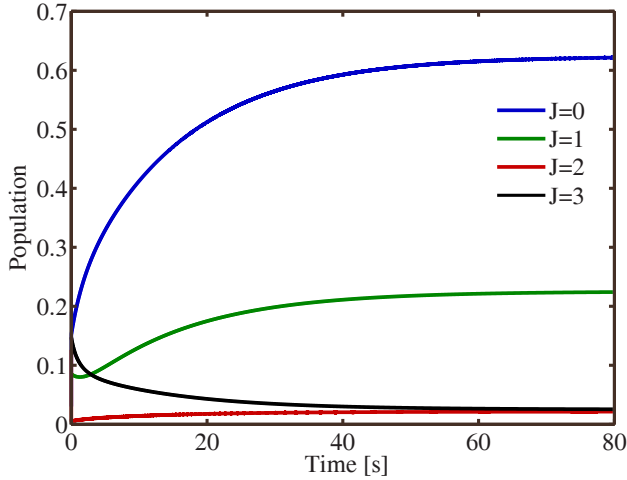


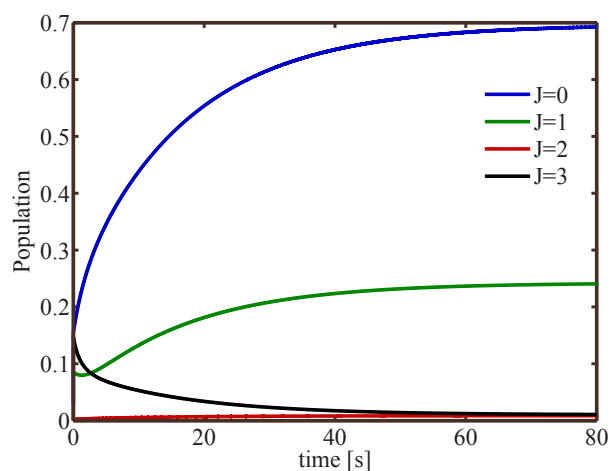
**Figure 6.4:** Population in the four lowest rotational states of  $\text{MgH}^+$  as function of time, when subject to the 300 K BBR field present in the trap and the cooling scheme shown in figure 6.1. The simulation was performed using effective rates for the pumping of population between  $|0\rangle_{\text{rot}}$  (blue line) and  $|2\rangle_{\text{rot}}$  (red line) as explained in the text. The population in  $|2\rangle_{\text{rot}}$  is rapidly emptied as a result of the large effective pumping rate  $\gamma_{\text{cool}}$ , while the population in  $|3\rangle_{\text{rot}}$  (black line) is removed somewhat slower as the result of BBR redistributions. Finally, the population in  $|1\rangle_{\text{rot}}$  (green line) increases as a result of rotational heating from the ground state. The population in the rotational ground state after 60 s is  $\sim 60\%$ , while the population in  $|0\rangle_{\text{rot}}$  and  $|1\rangle_{\text{rot}}$  combined is greater than 80 %.

### 6.3.1 Complications and prospects for improvement

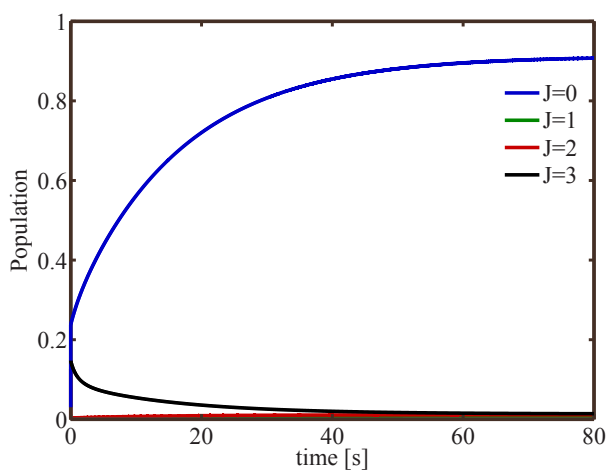
It is necessary to consider the parameters used in the numerical simulations carefully. In the previously presented cooling schemes of this thesis, emphasis has been given to experimental feasibility. However, the parameters used in the previous section are problematic in several ways. Most importantly, the assumed linewidth of the laser is very small. Furthermore, incoherent scattering on an intermediate state with linewidth of more than 10 MHz will be a problem.

The achilles' heel of the scheme is incoherent scattering on the intermediate state, since scattering will take place on the dominant carrier transition, while the Raman transition must take place on sideband transitions for the scheme to be effective. The disadvantage was minimized by cooling with  $^{40}\text{Ca}^+$ , which results in a motionally colder sample, cf. section 2.6.1.

A modification of the cooling concept may circumvent the problems with incoherent scattering on the intermediate state. First, the Raman transition could be changed to a STIRAP type transition. STIRAP transitions are generally robust, but driving selective sideband transitions in a trap with STIRAP is not



(a) BBR at 300 K

(b) BBR and microwave pump on  $|1\rangle_{\text{rot}} \leftrightarrow |2\rangle_{\text{rot}}$ 

**Figure 6.5:** (a) Population in the four lowest rotational states of  $\text{MgH}^+$  as function of time, when subject to the 300 K BBR field present in the trap and the cooling scheme shown in figure 6.1 and using an internal molecular state as intermediate state in the Raman transition. The simulation was performed using effective rates for the pumping of population between  $|0\rangle_{\text{rot}}$  (blue line) and  $|2\rangle_{\text{rot}}$  (red line) as explained in the text. (b) Population in the four lowest rotational states of  $\text{MgH}^+$  as function of time when the  $|1\rangle_{\text{rot}} \leftrightarrow |2\rangle_{\text{rot}}$  transition in  $\text{MgH}^+$  is saturated by a microwave source, e.g. a Backward wave oscillator [132].

straight-forward. STIRAP on sideband-transitions are discussed in another context in chapter 7. Also, sideband cooling could be applied to narrow the thermal distribution over motional states so the Raman transition can occur on the first motional sideband. Another approach would be to use an internal state of the molecule as intermediate state. The narrow linewidth of such states would allow for smaller detunings and higher free-molecule Rabi frequencies in the Raman transition without inducing incoherent scattering. The trade-off would be that internal transitions typically have infrared transition frequencies, thus resulting in a very small Lamb-Dicke parameter.

We have performed preliminary investigations using the first excited vibrational state of  $\text{MgH}^+$  as intermediate state. The parameters are not optimized, but the preliminary results indicate that this approach is more feasible. We assume the intermediate state has an Einstein coefficient for spontaneous decay of 50 Hz and a transition wavelength of  $4\ \mu\text{m}$ . The detuning from the excited state in the Raman process is 500 MHz, the free molecule Rabi frequencies are 800 MHz, and the lasers in the Raman process were tuned to resonance when  $\nu'_i - \nu_i = 3$ . The linewidth,  $\Gamma$ , of the Lorentzian in equation (6.6) is a challenging, but less frightening, 100 kHz. The remaining parameters are identical to the previously used. With these parameters, the rate of inhomogeneous scattering on the intermediate state is acceptable at 30 Hz. Figure 6.5 shows the cooling efficiency with these parameters. We have also included a simulation, where the  $|1\rangle_{\text{rot}} \leftrightarrow |2\rangle_{\text{rot}}$  rotational transition is saturated with a microwave source [132]. The simulations represent preliminary investigations, but it appears that cooling using the scheme of figure 6.1 may be possible if the intermediate state in the molecular transition is long-lived.

## 6.4 Conclusion

We have shown a proof-of-principle of using internal-external state couplings to rotationally cool molecules confined in harmonic trap with a laser-cooled atomic ion. The only dissipative term in the cooling cycle stems from the spontaneous decay in the translational cooling of the atomic ion and it makes no reference to molecular vibrational structure, decay rates or selection rules. The scheme is hence fundamentally different from our previously proposed schemes in which the dissipative process was spontaneous decay from an excited molecular vibrational state.

The cooling scheme relies on cooling of the collective translational state through the atomic cooling cycle and pumping between an excited rotational molecular state and the molecular ground state with effective pumping rates faster than rotational redistribution mediated by BBR. The fundamental requirement of the scheme can therefore be summarized as  $\gamma_{\text{cool}} \gg \gamma_{\text{BBR}}$ , where the last rate is the rotational redistribution rate in BBR and  $\gamma_{\text{cool}}$  is found from the rates of external cooling,  $\{\Gamma_{\text{atom}}\}$ , and rates of the individual Raman transitions,  $\{\Gamma_{\text{mol}}\}$ . Finally,  $\gamma_{\text{BBR}}$  must be much greater than the rate of trap loss. The method is very

versatile and may be readily adapted to polyatomic molecules, provided the rotational and, if relevant, vibrational redistribution due to BBR can occur from any populated state to the state addressed by the Raman laser on the required timescale.

While complications appeared during our work with this scheme, it may be worth investigating the cooling concept further, considering the relative simplicity and versatility of the cooling concept.

# CHAPTER 7

## State Preparation by Projection Measurement

### 7.1 Introduction

In chapter 3 and 4 we demonstrated methods to rotationally cool molecular ions that are initially in equilibrium with BBR at room temperature. The cooling schemes were relatively simple and capable of rotational cooling of many different diatomic molecular ions.

In this chapter, we focus on an alternative route to the production of molecular ions in specific states. The physical system used for this purpose consists of one trapped molecular ion sympathetically cooled by a simultaneously trapped atomic ion. Such a situation has been realized in experiments, and it has been shown to be possible to determine the molecular ion species non-destructively by a classical resonant excitation of one of the two axial collective modes of the two-ion system [40]. With this setup, we now propose to exploit the quantum aspect of the same collective modes to create correlations between the internal state of the molecular ion and the collective motional state in the trap potential. Previously, correlations in two-ion systems were essential in, e.g., demonstrations of quantum logical gates [147] and in a proposal for high-resolution spectroscopy [148]. The proposal presented in this chapter has been published in [149].

We thus consider the translational motion of one atomic ion and one molecular ion along one dimension of a harmonic trapping potential of frequency  $\Omega_{\text{trap}}$ . In section 5.2, we demonstrated that the resulting equation of motion conveniently can be written as a sum of two harmonic oscillator equations, each representing a normal mode of collective vibrations in the trapping potential. The system is assumed to be cooled to sub-Doppler temperatures for example by resolved sideband cooling [80].

In accordance with our previous estimates, the molecular ion is initially in internal equilibrium with the 300 K BBR of the trap environment. Again, for

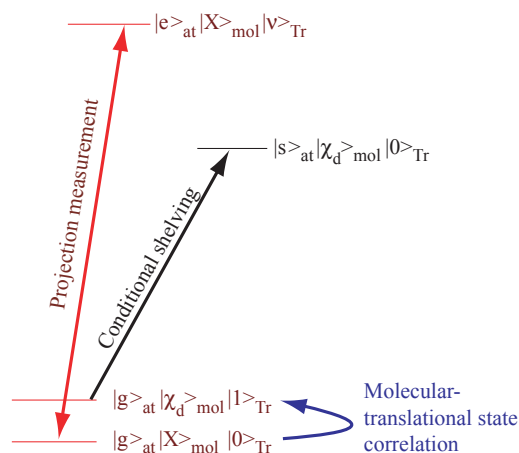


**Figure 7.1:** Idealized sketch of the state-selection sequence. The first step is cooling to the ground state of the collective translational mode,  $|0\rangle_{\text{Tr}}$ , with the molecule in the electronic ground state and with the internal ro-vibrational states characterized by a statistical ensemble  $|X\rangle_{\text{mol}}$ . The second step is to correlate the collective mode of the two-ion system with the internal state of the molecule by exciting the collective mode to  $|1\rangle_{\text{Tr}}$  if the molecule is in a specific internal state,  $|\chi_d\rangle_{\text{mol}}$ . Next, if the collective mode is excited, conditional shelving transfers the atom to the long-lived metastable state,  $|s\rangle_{\text{at}}$ . Finally, the projection measurement proceeds by exposing the atomic ion to light which is resonant with the transition between the atomic ground state,  $|g\rangle_{\text{at}}$ , and an excited state,  $|e\rangle_{\text{at}}$ . Re-scattered light will then be absent only if the atom is in the shelved state and hence the molecule in the desired internal state.

lighter molecular species, BBR equilibrium implies that the internal molecular state is found from a statistical ensemble over many rotational eigenstates, but only the vibrational ground state.

## 7.2 Selection Sequence

We proceed by describing the sequence of manipulations that allows preparation of molecular ions in a given internal state,  $|\chi_d\rangle_{\text{mol}}$ .

The scheme requires the presence of a closed optical pumping cycle in the atomic ion, used for cooling, combined with a metastable state which is not resonant with the cooling lasers, used for detection by the ion shelving technique.  $^{40}\text{Ca}^+$  is one example of such a system (cf. figure 2.9) [150, 151].

As depicted in figure 7.1, the state preparation of the molecular ion ideally involves the following steps. First, the two-ion system is cooled to its collective motional ground state [72, 80] with the molecule in the electronic ground state and with a Maxwell-Boltzmann distribution over ro-vibrational states. We con-

Vibrational ground state		
IE	$ g\rangle_{\text{at}}  X\rangle_{\text{mol}}  0\rangle_{\text{Tr}}$	
CEI	$ g\rangle_{\text{at}}  \chi_d\rangle_{\text{mol}}  1\rangle_{\text{Tr}}$	$ g\rangle_{\text{at}}  X'\rangle_{\text{mol}}  0\rangle_{\text{Tr}}$
CS	$ s\rangle_{\text{at}}  \chi_d\rangle_{\text{mol}}  0\rangle_{\text{Tr}}$	$ g\rangle_{\text{at}}  X'\rangle_{\text{mol}}  0\rangle_{\text{Tr}}$
PM	dark	fluorescent

**Table 7.1:** The evolution of the system through the state-selection sequence depicted in figure 7.1. IE: Initialization of the External state of the two-ion system by cooling the collective mode to the ground state. CEI: Correlation of collective External modes and Internal molecular state. CS: Conditional Shelving. PM: Projection Measurement. In the table,  $|X'\rangle_{\text{mol}}$  denotes the modified statistical ensemble of internal molecular states when the desired state,  $|\chi_d\rangle_{\text{mol}}$ , has been removed from  $|X\rangle_{\text{mol}}$ . The portion of the ensemble of ro-vibrational states that was initially in the desired molecular state  $|\chi_d\rangle_{\text{mol}}$  is conditionally shelved and unaffected by the projection measurement. The remaining ro-vibrational states, on the other hand, are unaffected by the conditional shelving and therefore lead to fluorescence upon projection measurement.

sider only one of the two independent axial modes of the two-ion system and refer to it as the collective mode. Second, laser fields are applied to induce transitions between the ground and the first excited motional states conditioned on the specific ro-vibrational state of the molecular ion. This procedure creates correlations between the motional state of the two-ion system and the internal state of the molecular ion. Next, conditioned on an excitation of the collective mode, an atomic shelving transition to a metastable state is driven by another laser field. Finally, laser fields are applied to project the atomic ion on the shelved (non-fluorescing) or non-shelved (fluorescing) state. If no fluorescence is observed, we conclude that the molecular ion is in the internal state of interest. Contrary, if fluorescence is present, the ion is not in the desired state. In the latter case, the procedure is repeated after a duration of time sufficiently long to bring the molecule back in thermal equilibrium, typically through interaction with BBR. Eventually, no fluorescence is detected in the final step and the molecular ion is known to be in the desired quantum state. A state-to-state analysis of the procedure is presented schematically in Table 7.1.

### 7.3 Efficiency of the CEI and CS Steps

Step 1, sideband cooling to the motional ground state, is well established both theoretically and experimentally [72, 79–81, 83]. Similarly, projection measurement (step 4), has been thoroughly verified in different experiments [150–152]. In this section we discuss a number of approaches to CEI and CS and present some numerical simulations.

### 7.3.1 Correlation of external motion and the internal molecular state (CEI)

We have investigated several approaches to CEI. Table 7.2 gives an overview of the approaches and some basic characteristics. First, one may use a  $\pi$ -pulse to transfer population to  $|\chi_d\rangle_{\text{mol}} |1\rangle_{\text{Tr}}$  from a different molecular state,  $|\chi''\rangle_{\text{mol}}$ , via an excited molecular state  $|\chi'\rangle_{\text{mol}}$ . The  $\pi$ -pulse approach has been experimentally demonstrated for atomic ions [153], and should work for molecular ions, albeit it will not be equally efficient for all substates of the rotational state of the molecule. Additionally, it should be noted that it can be challenging to meet the requirements to the stability and bandwidth of the light source. As an alternative, a STIRAP process between the same molecular states should be more attractive experimentally, as STIRAP is generally more robust than  $\pi$ -pulses, cf. section 2.4. However, the two-photon detuning,  $\delta$  should still be much smaller than the spacing between the motional levels,  $\Omega_{\text{trap}}$ , which can be difficult to achieve using two different lasers.

Technically, it is significantly simpler to ensure stable two-photon resonance at the required level ( $\delta \ll \Omega_{\text{trap}}$ ) if the two laser frequencies are similar. The advantage of using similar frequencies is that the two frequencies can be generated by acousto-optical modulation of a single pump beam. Fluctuations in the frequencies of the two beams will then coincide, i.e. fluctuations in the pump beam will lead to fluctuations in the single photon detuning,  $\Delta$ , rather than the more critical two-photon detuning,  $\delta$ . As a consequence, we considered the adiabatic transfer process depicted in Table 7.2(c). First, a pulse couples the final state,  $|\chi_d\rangle_{\text{mol}} |1\rangle_{\text{Tr}}$ , and intermediate states,  $|\chi'\rangle_{\text{mol}} |\nu\rangle_{\text{Tr}}$ , with a coupling strength characterized by the free molecule Rabi frequency,  $\Omega_s(t)$ , while a delayed pulse couples the initial state,  $|\chi_d\rangle_{\text{mol}} |0\rangle_{\text{Tr}}$ , to  $|\chi'\rangle_{\text{mol}} |\nu\rangle_{\text{Tr}}$  with free molecule Rabi frequency  $\Omega_p(t)$ . Here,  $|\chi_d\rangle_{\text{mol}}$  and  $|\chi'\rangle_{\text{mol}}$  denote the desired and intermediate molecular state, respectively.

Though the pulse sequence resembles a STIRAP process, there is an important difference since the two laser pulses, that are only shifted in frequency by the collective mode frequency ( $\simeq 10$  MHz), interact with same internal transitions of the molecule. The similar frequencies of  $\Omega_p$  and  $\Omega_s$  thus makes it easier to achieve two-photon resonance, but invalidates the rotating wave approximation used to derive equation (2.21). As a consequence, it is necessary to modify equation (2.21) to include terms where

- $\Omega_s$  and  $\Omega_p$  both couple  $|g\rangle - |i\rangle$  and  $|f\rangle - |i\rangle$
- Several motional states have to be included in the simulation.



## Approaches to CEI

System	Method	Characteristics
<p>a)</p>	$\pi$ -pulse	<ul style="list-style-type: none"> <li>- Experimentally demonstrated with atomic ions</li> <li>- Address a selection of sub-states</li> <li>- Requires very stable light source</li> </ul>
<p>b)</p>	STIRAP	<ul style="list-style-type: none"> <li>- Address a selection of sub-states</li> <li>- Requires less stable light source compared to <math>\pi</math>-pulse</li> </ul>
<p>c)</p>	Adiabatic transfer	<ul style="list-style-type: none"> <li>- Address all substates</li> <li>- Good performance in simulations</li> <li>- Several motional states are populated</li> </ul>
<p>d)</p>	Driven, non-adiabatic	<ul style="list-style-type: none"> <li>- Simple; one laser frequency</li> <li>- Destructive interference between reaction channels makes it difficult to get motional excitation without scattering</li> <li>- Several motional states are populated</li> </ul>
<p>e)</p>	Rayleigh scattering	<ul style="list-style-type: none"> <li>- Rayleigh scattering dominant only at large detunings; cannot, in general, be made state selective</li> </ul>

**Table 7.2:** Five methods to achieve CEI. The individual methods are discussed in detail in the text.

The inclusion of several motional states is necessary, since transitions to higher excited motional levels also will be near-resonant with  $\Omega_{p,s}$ <sup>1)</sup>. Including only the motional states  $|0\rangle_{\text{Tr}}$  and  $|1\rangle_{\text{Tr}}$  and choosing the basis  $\{|\chi_d\rangle_{\text{mol}}|0\rangle_{\text{Tr}}, |i\rangle|0\rangle_{\text{Tr}}, |i\rangle|1\rangle_{\text{Tr}}, |\chi_d\rangle_{\text{mol}}|1\rangle_{\text{Tr}}\}$ , the interaction picture Hamiltonian,  $H_I$ , becomes

$$\frac{1}{2} \begin{bmatrix} 0 & \Omega_p(1-\frac{1}{2}\eta^2)+ & -i\Omega_p\eta- & 0 \\ +\Omega_s(1-\frac{1}{2}\eta^2)e^{-i\Delta\omega t} & 2\Delta & -i\Omega_s\eta e^{-i\Delta\omega t} & 0 \\ i\Omega_s\eta+ & 0 & 2(\Delta + \Omega_{\text{trap}}) & \Omega_s(1-\frac{3}{2}\eta^2)+ \\ +i\Omega_p\eta e^{i\Delta\omega t} & & +\Omega_p(1-\frac{3}{2}\eta^2)e^{-i\Delta\omega t} & \\ 0 & i\Omega_s\eta+ & \Omega_s(1-\frac{3}{2}\eta^2)+ & 2\delta \\ +i\Omega_p\eta e^{i\Delta\omega t} & +\Omega_p(1-\frac{3}{2}\eta^2)e^{i\Delta\omega t} & & \end{bmatrix}$$

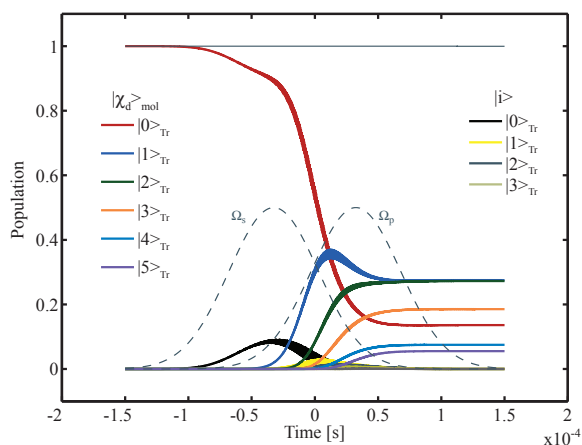
where  $\Delta\omega = \omega_p - \omega_s$  is the difference between the laser frequencies, while  $\Delta$  and  $\delta$  are the single-photon and two-photon detunings, respectively. Furthermore, the matrix elements were entered to second order in  $\eta$  according to equation (5.8). The rotating phases on the off diagonal matrix elements distinguish this interaction Hamiltonian from that of section 2.4. Fortunately, since  $\Delta\omega \simeq \Omega_{\text{trap}} \sim 10$  MHz, the rotating phase on the off-diagonal matrix elements can be averaged to zero (RWA), provided the interaction time is significantly longer than  $0.1 \mu\text{s}$ . We also require the process to be much faster than the motional heating time in the trap, which is on the order of 10 motional quanta per second [80].

To obtain reliable numerical results, it turns out to be insufficient to include only  $|0\rangle_{\text{Tr}}$  and  $|1\rangle_{\text{Tr}}$  in the Hilbert space. For reliable results, we expand the state of the two-ion system as  $|\Psi(t)\rangle = \sum_{\nu_{\text{Tr}}=0}^{\nu_{\text{Tr,max}}} c_{\nu_{\text{Tr}}}(t) |\chi_d\rangle_{\text{mol}} |\nu\rangle_{\text{Tr}} + b_{\nu_{\text{Tr}}}(t) |\chi'\rangle_{\text{mol}} |\nu\rangle_{\text{Tr}}$  with  $\nu_{\text{Tr,max}} = 5$  for convergence. The initial condition is  $c_0(t=0) = 1$  and the desired final state is  $|\chi_d\rangle_{\text{mol}} |1\rangle_{\text{Tr}}$ . In figure 7.2(a) we present the results of a numerical simulation of CEI. In the simulation, both laser pulses are assumed to be Gaussian in time with a width  $\tau = 50 \mu\text{s}$  (FWHM) and separated by  $1.3\tau$ . We assume maximum free molecule Rabi frequencies of 6.7 MHz for both pulses<sup>2)</sup>, and a detuning from the intermediate state of  $\delta = 10$  MHz. A transient population of the intermediate states,  $|i\rangle$ , is noted in figure 7.2(a).

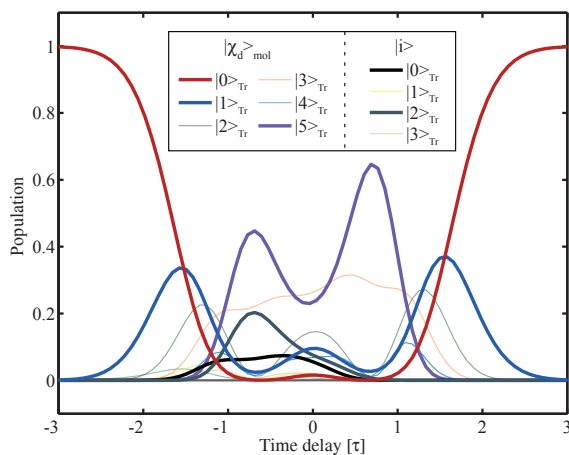
We investigated the consequences of the transient population by introducing an imaginary terms on the diagonal of  $H_I$ , representing spontaneous decay out of the system. Our simulations showed that decay rates well over 10 kHz can be accepted. Since electronically excited states of molecules typically are short-lived, we used a vibrational level of the molecule in the simulation and

<sup>1)</sup>In general, it is also necessary to include several motional states in the simulation of conventional STIRAP in the trap potential

<sup>2)</sup>The assumed Rabi frequency of 6.7 Mhz can be achieved by focusing CW laser beams with a modest power of  $\sim 10$  mW to spot sizes of  $\sim 1\text{mm}^2$ .



(a) Population evolution during CEI



(b) Final population versus pulse delay

**Figure 7.2:** Numerical simulations of the CEI process using the approach of Table 7.2(c). **(a)** Population in the states  $|\chi_d\rangle_{\text{mol}} |0\rangle_{\text{Tr}} \dots |\chi_d\rangle_{\text{mol}} |5\rangle_{\text{Tr}}$  and the intermediate states  $|i\rangle$  as function of time during the CEI process. The population initially in  $|\chi_d\rangle_{\text{mol}} |0\rangle_{\text{Tr}}$  branches out to several motional states. Transient population in the intermediate state is observed (compare with figure 2.3), which led us to use a long-lived vibrational state of the molecule as intermediate state. The pulse envelopes are shown as dashed lines on the figure. **(b)** Population distribution after the CEI process as function of the pulse time delay in units of the pulse width,  $\tau$ . It is noticed that the excitation to higher-lying motional states clearly depends on the pulse time delay, and that nonzero population of the excited state is found if the time delay is negative, i.e. if the pulses are reversed.

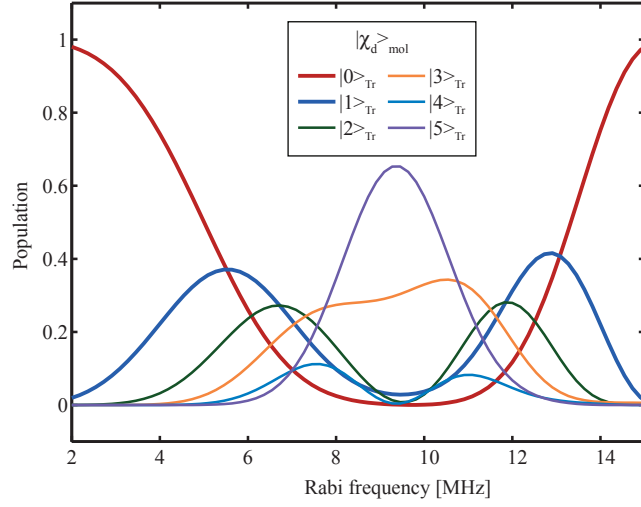


**Figure 7.3:** Final population distribution after CEI as function of the maximal Rabi frequencies of  $\Omega_p$  and  $\Omega_s$ . Like it was the case with the pulse delay, the Rabi frequencies can also be used to control the distribution over motional states in the trap. It should be noted that the effect of truncating the Hilbert space at  $|5\rangle_{\text{Tr}}$  will be significant when the population in  $|5\rangle_{\text{Tr}}$  state becomes appreciable, so the quantitative results with Rabi frequencies of 8 – 10 MHz should not be relied upon.

assumed a transition wavelength of  $4\ \mu\text{m}$ . The simulation shows that more than 80% of the population is transferred to excited motional states, but rather than ending in the desired state,  $|\chi_d\rangle_{\text{mol}} |1\rangle_{\text{Tr}}$ , the population is transferred to a superposition of the states  $|\chi_d\rangle_{\text{mol}} |1\rangle_{\text{Tr}} \dots |\chi_d\rangle_{\text{mol}} |5\rangle_{\text{Tr}}$ . This can be understood from the equidistance of the energy levels in the harmonic trap. If adiabatic transfer is energetically allowed from  $|\chi_d\rangle_{\text{mol}} |0\rangle_{\text{Tr}}$  to  $|\chi_d\rangle_{\text{mol}} |1\rangle_{\text{Tr}}$ , then it is also allowed from  $|\chi_d\rangle_{\text{mol}} |1\rangle_{\text{Tr}}$  to  $|\chi_d\rangle_{\text{mol}} |2\rangle_{\text{Tr}}$  etc. The consequences of CEI leading to population of several excited states is discussed in the next section, where we consider the subsequent step, CS, in more detail. We note that in the simulation, the transfer efficiency was stable when varying the detuning a few MHz, which is of experimental importance. The effect of the rotating phases in  $H_I$  can be seen as small oscillations in the resulting populations during CEI (on the scale of figure 7.2(a), the oscillations are seen as thickening of the lines). As expected from the previous argument, the oscillations become dominant when the interaction time approaches  $1/\Omega_{\text{trap}}$ .

Figure 7.2(b) depicts the final population distribution after CEI, when the delay between the pulses is varied from  $-3\tau$  to  $3\tau$ . The population in higher excited states increase with the pulse overlap, since larger pulse overlap allow the system to go through more motional excitations. We thus conclude that the time delay between the pulses offers some control over the motional excitations.

It should be noted that the quantitative results of the simulation in figure 7.2(b) is unreliable when the population in  $|\chi_a\rangle_{\text{mol}}|5\rangle_{\text{Tr}}$  becomes dominant, since the effect of truncating the Hilbert space can be critical. The qualitative result of increased motional excitation with increased pulse overlap is, however, reliable. Similarly, we note that the excited state of the molecule is populated after CEI for negative time delays, i.e. when reversing the pulse sequence with respect to conventional STIRAP.

Figure 7.3 explores the final population after CEI when varying the Rabi frequencies. We note that the Rabi frequencies influence not only the transfer efficiency, but also the distribution over motional states. When increasing the Rabi frequency beyond the scale of figure 7.3, the population distribution displays a very complex dependence of the Rabi frequency, mostly with very efficient motional excitations to the higher-lying states. This is not unexpected since increasing pulse height should allow more motional excitations, but the effect of truncating the Hilbert space in the simulation could be significant. We therefore use Rabi frequencies of 6.7 MHz in the following discussion.

We now proceed by considering two intuitively appealing methods to achieve CEI by using a single laser frequency, which is of obvious experimental convenience. The approaches are depicted in Table 7.2(d) and (e). We will show that neither of the methods are as attractive as the previously mentioned processes, but we have chosen to include them in the discussion for completeness and because their experimental simplicity makes them very tempting.

The approach in table 7.2(d) represents an off-resonant stimulated excitation-decay process with a pulse duration less than  $1/\Omega_{\text{trap}}$ , thus making motional excitations energetically allowed. Unfortunately, the reaction channels  $|\chi_a\rangle_{\text{mol}}|0\rangle_{\text{Tr}} \leftrightarrow |\chi_a\rangle_{\text{mol}}|n\rangle_{\text{Tr}} \leftrightarrow |\chi_a\rangle_{\text{mol}}|1\rangle_{\text{Tr}}$  interfere destructively with each other, canceling the transition to fourth order in the Lamb-Dicke parameter  $\eta$ . The destructive interference originates in the  $\pi$  phase shift between motional transition matrix elements for absorption and emission of a photon, which can be seen from equation (5.8). As a result of the weak coupling, it will be difficult to excite the collective motional states without scattering on the intermediate state.

In table 7.2(e), we consider using Rayleigh scattering on an excited molecular state. From classical radiation theory, valid for a far-off resonant incident field, it can be shown that Rayleigh scattering normally dominates rotational and vibrational Raman scattering, since Rayleigh scattering is proportional to the polarizability of the molecule, while Raman scattering is proportional to the anisotropy of the polarizability (rotational Raman) and the change of polarizability with internuclear distance (vibrational Raman) [50]. In the presented selection sequence, however, the motional excitations must be state-selective, thus requiring the incident laser light to be close to resonance with one transition in the molecule. As a consequence, a quantum-mechanical description is needed. Unfortunately, a quantum mechanical description of near-resonant scattering does not allow for such easy classification of Rayleigh and Raman scattering amplitudes, and Rayleigh scattering cannot, in general, be assumed

to dominate [154].

To conclude, we have shown several ways of achieving CEI. Which approach to use will depend on the particular system in question and experimental constraints, but it appears that the adiabatic transfer method, depicted in table 7.2(c) and simulated in figure 7.2 and 7.3, is experimentally attractive. We showed that an excitation efficiency better than 80% is feasible. We proceed by discussing the CS step and the consequences of the final population being distributed over several motionally excited states.

### 7.3.2 External state conditional shelving (CS)

As with CEI, external state conditional shelving can be achieved with various approaches. However, we will later show that the confidence of the state preparation is largely insensitive to the efficiency of CS, so the discussion of CS will not be quite as detailed as CEI. Additionally, CS has previously been demonstrated experimentally.

In quantum logic experiments, atomic shelving conditioned on the external motional state has previously been demonstrated experimentally using  $\pi$ -pulses [153, 155]. The method is very efficient, but requires the use of very stable light source, and it will not, in general, be possible to effectively empty more than one excited motional state, since the effective Rabi frequencies for  $|n\rangle_{\text{Tr}} \rightarrow |n-1\rangle_{\text{Tr}}$  transitions depend on  $n^3$ ). The  $\pi$ -pulse approach is therefore not ideal if the adiabatic transfer process of table 7.2(c) is used in the CEI step, since the population will be distributed over several motional states.

As an alternative, we consider the STIRAP type process on the red sideband of translational motion from the atomic ground state,  $|g\rangle_{\text{at}}$  to the shelved atomic state,  $|s\rangle_{\text{at}}$  via an intermediate state,  $|i\rangle_{\text{at}}$ . We expand the state of the combined system as  $|\Psi(t)\rangle = \sum_{\nu_{\text{Tr}}=0}^{\nu_{\text{Tr,max}}} c_{\nu(t)} |g\rangle_{\text{at}} |\chi d\rangle_{\text{mol}} |\nu\rangle_{\text{Tr}} + b_{\nu(t)} |i\rangle_{\text{at}} |\chi d\rangle_{\text{mol}} |\nu\rangle_{\text{Tr}} + a_{\nu(t)} |s\rangle_{\text{at}} |\chi d\rangle_{\text{mol}} |\nu\rangle_{\text{Tr}}$ . The STIRAP interaction hamiltonian is derived by straight-forward generalization of equation (2.25).

The conditions for adiabatic following in a STIRAP process were given in equation (2.29). In order to obtain CS, it is furthermore necessary that the power broadening of the individual levels is smaller than  $\Omega_{\text{trap}}$ , since the motional ground state  $|0\rangle_{\text{Tr}}$  would otherwise interfere in the process. The additional constraint

$$\frac{\Omega_s \Omega_p}{\Delta} \ll \Omega_{\text{trap}} \quad (7.1)$$

is thus inferred.

A numerical simulation of the process is shown in figure 7.4. The simulation confirms the ability to perform CS with a STIRAP type process. Furthermore, we see that it is possible to empty all the states populated after CEI using the adiabatic transfer method discussed in the previous section. The numerical simulations show that with the final population after the CEI process of figure

<sup>3)</sup>Since the Rabi frequencies are known functions of  $n$ , it is, to a certain extent, possible to adjust the pulse area to tailor the transition probability[155]

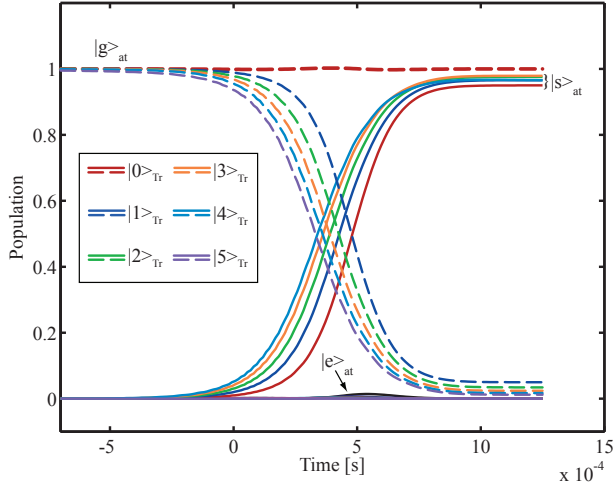


**Figure 7.4:** Population evolution during the atomic STIRAP type process proposed in the text. Solid lines depict the population in the shelved atomic state,  $|s\rangle_{at}$ , while dashed lines show the population in the atomic ground state,  $|g\rangle_{at}$ . The motional states of the trap potential are distinguished by the color codes as shown on the figure. As initial conditions we have chosen unit population of  $|g\rangle_{at} |\nu\rangle_{Tr}$ ,  $\nu = 0 \dots 5$  to explore the performance of the sideband transitions for the motional states on equal terms. Note that with this choice of initial condition, the population is not normalized. The simulation is performed with gaussian pulses of  $500 \mu\text{s}$  width and maximum Rabi frequencies of 500 kHz. We chose  $\Omega_{\text{trap}} = 10 \text{ MHz}$ , and a detuning from the excited state,  $|e\rangle_{at}$ , of 500 kHz. With the given parameters, minor transient population of the excited atomic state is seen (black on figure).

7.2(a) as initial condition, more than 95% of the population in motionally excited states can be transferred to the shelved state. The simulation also shows slight transient population of the excited atomic state, which can be problematic depending on the particular system in question. Our simulations indicate that the transient population is due to incomplete satisfaction of equation (7.1), and may thus be minimized by increasing the trapping frequency or decreasing the Rabi frequencies, the latter at expense of the transition probability. Furthermore, we expect STIRAP on the second motional sideband to be more robust, since the ground state would be separated twice as far from the states undergoing STIRAP. Performing CS on the second sideband of external motion will have the added benefit of mitigating uncertainties induced by thermal population of  $|1\rangle_{Tr}$  after imperfect cooling of the system in the external state initialization process, as discussed in the subsequent sections.

## 7.4 Imperfections in the Individual Steps

The proposed selection sequence should result in a 100 % certain preparation of the molecule if the atom is found in the shelved state at the end of the sequence, provided that the external motion of the system is cooled to the ground state. In the case of zero temperature of the external motion, the efficiency of correlation of external motion and molecular state and the efficiency of conditional shelving affects the number of measurements required to achieve state preparation, but not the confidence of the state preparation. While this is very promising, we must consider the effect of imperfections of the individual steps when the temperature of external motion is finite. In the following, we discuss the imperfections in the various steps of the procedure.

### 1) Initialization of the external state of the two-ion system (IE)

Cooling of a two-ion system completely to the motional ground state,  $|0\rangle_{\text{Tr}}$ , is unrealistic, but several experiments show that it is feasible to achieve  $W_0 = 95\%$  population in  $|0\rangle_{\text{Tr}}$  in the case of two atomic ion species [72, 80]. The same degree of cooling is expected for an atomic-molecular ion system. We therefore use a Boltzmann distribution with  $W_0 = 0.95$ , and this results in  $W_1 \simeq 0.047$  and  $W_2 \simeq 0.003$  for the populations in  $|1\rangle_{\text{Tr}}$  and  $|2\rangle_{\text{Tr}}$ , respectively.

### 2) Correlation of external motion and the internal molecular state (CEI)

We discussed this part of the procedure in detail in the previous section, where we proposed several approaches to CEI. In the following, we consider the adiabatic passage approach of table 7.2(c), which was simulated numerically. We found, that more than 80 % of the population in  $|\chi_d\rangle_{\text{mol}}$  can be excited translationally. In the following, we use a slightly more conservative estimate of the transfer efficiency,  $\wp_{\text{CEI}} = 0.7$ .

### 3) External state conditional shelving (CS)

Conditional shelving of the collective motion was also discussed in some detail in the previous section. With the  $\pi$ -pulse approach, demonstrated in quantum logic experiments [153], very high transfer efficiency is expected, but the method will only be able to effectively empty one motional state. As an alternative, we considered CS with a STIRAP type process and demonstrated shelving probabilities exceeding 0.95 in a numerical simulation. In the following, we will use the somewhat more conservative estimate of the shelving probability,  $\wp_{\text{CS}} = 0.7$ .

### 4) Projection measurement (PM)

The final step, projection measurement on the atomic ion, can be made very efficient. With a typical exposure time  $T = 5$  ms, one should be able to determine the projected atomic state with a confidence exceeding 95 % [79, 152].



## 7.5 Over-all Confidence of Steps 1-4

The probability of being in the ideal initial state,  $|g_{\text{at}}, \chi_d, 0_{\text{Tr}}\rangle$ , is  $P_{\chi_d} W_0$ , where  $P_{\chi_d}$  denotes the initial population in  $|\chi_d\rangle_{\text{mol}}$  and  $W_0$  the initial population in the collective motional state  $|0\rangle_{\text{Tr}}$ . Since this state has to go through both CEI and CS to reach the shelved state, the probability of finding the molecule in the shelved state after the selection sequence is  $S_{\text{prep}} = P_{\chi_d} W_0 \wp_{\text{CEI}} \wp_{\text{CS}}$ . Unfortunately, a false positive result occurs if the system is initially in the state  $|g\rangle_{\text{at}} |X'\rangle_{\text{mol}} |\nu\rangle$  with  $\nu \geq 1$  since the system may proceed through CS without exciting the motional state during CEI (see table 7.3). The probability of a false positive measurement is then  $E = (1 - P_{\chi_d})(1 - W_0) \wp_{\text{CS}}$ , where the first two factors account for the initial population in the excited states of the collective motion and the last factor accounts for the necessary application of CS. We define the confidence of a measurement as  $F = S_{\text{prep}} / (S_{\text{prep}} + E)$ .

Excited vibrational state	
IE	$ g\rangle_{\text{at}}  X\rangle_{\text{mol}}  1\rangle_{\text{Tr}}$
CEI	$ g\rangle_{\text{at}}  \chi_d\rangle_{\text{mol}}  0\rangle_{\text{Tr}}$ $ g\rangle_{\text{at}}  X'\rangle_{\text{mol}}  1\rangle_{\text{Tr}}$
CS	$ g\rangle_{\text{at}}  \chi_d\rangle_{\text{mol}}  0\rangle_{\text{Tr}}$ $ s\rangle_{\text{at}}  X'\rangle_{\text{mol}}  0\rangle_{\text{Tr}}$
PM	fluorescent                      dark

**Table 7.3:** The evolution of the system through the state selection sequence of figure 7.1 if the translational motion is excited due to finite translational temperature of the two-ion system. For simplicity, both CEI and CS is assumed to have unit efficiency. CEI is furthermore assumed to work equally well in the reverse direction, transferring  $|g\rangle_{\text{at}} |\chi_d\rangle_{\text{mol}} |1\rangle_{\text{Tr}}$  to  $|g\rangle_{\text{at}} |\chi_d\rangle_{\text{mol}} |0\rangle_{\text{Tr}}$ . Since population initially in  $|g\rangle_{\text{at}} |X'\rangle_{\text{mol}} |1\rangle_{\text{Tr}}$  is unaffected by CEI, that population will remain in the excited motional state after CEI, thus being susceptible to the CS process. As a result, population initially in  $|g\rangle_{\text{at}} |X'\rangle_{\text{mol}} |1\rangle_{\text{Tr}}$  will be shelved after CEI and CS, and thus result in a false positive measurement after PM, cf. table 7.1.

As a test case we assume  $P_{\chi_d} = 5\%$  and use a thermal distribution over external vibrational states determined by letting  $W_0 = 95\%$ . Non-fluorescence in the final stage of the state preparation then give a confidence of the molecule be in  $|\chi_d\rangle_{\text{mol}}$  of about  $F \simeq 0.4$  which is too marginal for the procedure to be useful.

On the basis of these considerations we turn to consider a general maneuver capable of distinguishing the two dark states in the selection sequence of Table 7.1 and 7.3.

## 7.6 State Purification (SP)

The principal source of error is false positive detections stemming from the initial population in  $|1\rangle_{\text{Tr}}$ . These errors are excluded by use of the state-purification procedure of Table 7.4. If no fluorescence is detected after the state preparation process, CEI is reapplied. The second step is another CS process transferring  $|s\rangle_{\text{at}}$  to  $|g\rangle_{\text{at}}$  on the red sideband of the collective motion. Finally PM is repeated. The desired final state is now fluorescent while other states are dark.

State purification		
Start	$ s\rangle_{\text{at}}  \chi_d\rangle_{\text{mol}}  0\rangle_{\text{Tr}}$	$ s\rangle_{\text{at}}  X'\rangle_{\text{mol}}  0\rangle_{\text{Tr}}$
CEI	$ s\rangle_{\text{at}}  \chi_d\rangle_{\text{mol}}  1\rangle_{\text{Tr}}$	$ s\rangle_{\text{at}}  X'\rangle_{\text{mol}}  0\rangle_{\text{Tr}}$
CS	$ g\rangle_{\text{at}}  \chi_d\rangle_{\text{mol}}  0\rangle_{\text{Tr}}$	$ s\rangle_{\text{at}}  X'\rangle_{\text{mol}}  0\rangle_{\text{Tr}}$
PM	dark	fluorescent

**Table 7.4:** State Purification (SP). Start: The states of the system ending in the shelved atomic state after the state preparation process 1)-4) when assuming finite temperature of the collective mode. SP proceeds by a second Correlation of the External mode and Internal molecular state (CEI), exciting the collective mode if the molecule is in  $|\chi_d\rangle_{\text{mol}}$ . Then Conditional Shelving (CS) transfers the atom back to the ground state  $|g\rangle_{\text{at}}$  if the collective mode is excited. Finally, a second Projection Measurement (PM) detects the atom in  $|g\rangle_{\text{at}}$  if the molecule is in  $|\chi_d\rangle_{\text{mol}}$ .

### 7.6.1 Confidence of the selection sequence after SP

The probability of a successful detection after the SP procedure is estimated by  $S_{\text{pur}} = S_{\text{prep}} \rho_{\text{CEI}} \rho_{\text{CS}}$ , as the population has to go through both CEI and CS after the state preparation. The probability of a false positive detection caused by population initially in excited motional states is now given by  $E1 = W_{l \geq 2} (1 - P_{\chi_d}) \rho_{\text{CS}}^2$ , since the system must start in the second excited state or higher to pass CS twice without being excited during CEI. Another source of false positive measurements appears due to stochastic heating during the relatively slow PM process. Assuming a heating rate of  $\Gamma = 10$  vibrational quanta per second [80], the error induced by stochastic heating is  $E2 = T\Gamma(1 - P_{\chi_d}) W_1 \rho_{\text{CS}}^2$ , since only population initially in  $|1\rangle_{\text{Tr}}$  will introduce error which is not accounted for in  $E1$ .

The confidence of state preparation after SP is defined as  $F' = S_{\text{pur}} / (S_{\text{pur}} + E1 + E2)$  and SP improves the confidence of state preparation to more than 80 % (see Fig. 2). Note that if  $W_0 = 100\%$ , the measurement cycle leads to 100 % certain state-preparation without SP, while increasing  $\rho_{\text{CEI}}$  to 100% only leads to 10% increase in the confidence of the final state preparation. Finally, we note that the preparation efficiency is independent of the conditional shelving efficiency,  $\rho_{\text{CS}}$ .

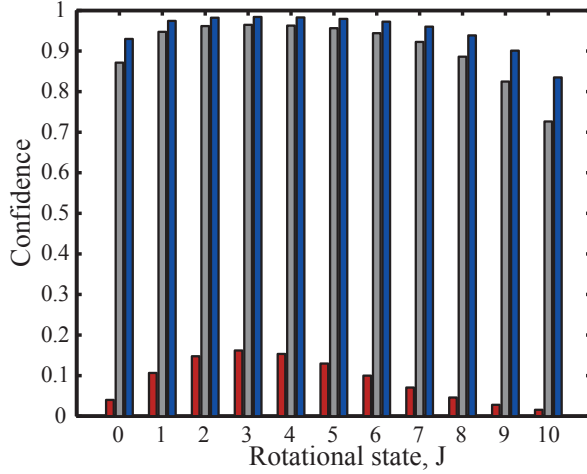


**Figure 7.5:** Confidence of preparing a  $\text{MgH}^+$  ion in rotational states. The red columns show the 300 K Boltzmann distribution over rotational states. The grey columns present the achievable confidence,  $F'$ , when state purification is applied. Finally, the blue columns show the confidence,  $F''$ , obtainable when selections using the second sideband are applied without state-purification.

### 7.6.2 Alternative approach

As an alternative to PS, we may perform CEI and CS on the second motional sideband, i.e., consider  $|g_{\text{at}}, X_{\text{mol}}, 0_{\text{Tr}}\rangle - |g_{\text{at}}, \chi_d, 2_{\text{Tr}}\rangle$  in the CEI step and  $|g_{\text{at}}, \chi_d, 2_{\text{Tr}}\rangle - |s_{\text{at}}, \chi_d, 0_{\text{Tr}}\rangle$  in the CS step. Since the initial probability  $W_2$  for being in  $|2\rangle_{\text{Tr}}$  is much smaller than  $W_1$ , the confidence of the preparation is improved considerably without applying SP, and simply given by  $F'' = S_{\text{prep}} / (S_{\text{prep}} + E'')$  with  $E'' = E \times (1 - W_0 - W_1) / (1 - W_0) \sim E \times 0.06$ . The required laser intensity would, however, increase due to the weaker coupling between  $|0\rangle_{\text{Tr}}$  and  $|2\rangle_{\text{Tr}}$  compared with the  $|0\rangle_{\text{Tr}} - |1\rangle_{\text{Tr}}$  coupling.

## 7.7 Conclusion

Additional complications may appear if different sub-states of the molecular ion result in a different Rabi frequencies for the MST. This can be countered by selecting a specific sub-state for the transition, eg. by splitting the sub-states with a magnetic field. Due to the relaxed demands to the transfer efficiency we do not expect such effect to be critical.

We have demonstrated a robust scheme allowing non-destructive detection of the internal state of a molecular ion in a trap. After preparation the molecule will be available for experiments on a timescale set by BBR-relaxation. It should

be noted, that for homonuclear molecules this timescale is very long, but MST could be harder to implement.

The strong coupling between molecular and atomic ions in an ion trap allowed the construction of a general detection scheme for internal states of molecular ion. The generality of the mapping of the internal state of the molecule to the atomic ion leads us to conclude that the scheme can be used on a large number of molecular species, diatomic as well as polyatomic.

Shortly prior to the submission of this thesis, the group of D. J. Wineland published an experimental demonstration of spectroscopy and state preparation of  $^{27}\text{Al}^+$ , which is not amenable for laser cooling [156]. The experiments were performed using an approach very similar to the one proposed in this chapter, thus confirming the feasibility of the scheme.

## CHAPTER 8

# Summary and Outlook

We have presented several schemes for cooling and preparation of the internal degrees of freedom in trapped and translationally cold molecular ions. The schemes of chapter 3 and 4 are relatively simple from an experimental point of view, and the light-source requirements are modest. Experimental implementation of these schemes is planned in the group here in Aarhus, and a method to measure the internal temperature of a molecular sample has been developed [41, 42, 90]. The cooling schemes of chapter 3 and 4 may readily be applied to many heteronuclear diatomic molecular ions.

In chapter 6, we have presented cooling scheme which do not rely on a spontaneous decay in the molecular ion. Spontaneous decay in the molecule is circumvented by coupling the internal state of the molecule with the collective motional state of a system consisting of the molecular ion and an atomic ion in a trap. The collective motional state of the two-ion system is then cooled by conventional translational cooling on the atomic ion. Although the numerical results were initially discouraging due to a large rate of incoherent scattering, we proposed several ways to improve the scheme and presented preliminary results indicating that the scheme can be salvaged. By avoiding a spontaneous decay in the molecule, the cooling scheme stays highly versatile and implementation with polyatomic molecular ions should be possible. Furthermore, the scheme does not require more than a single laser-driven Raman transition, which is promising for experimental implementation, albeit the required parameters for the Raman transition must be investigated further before a conclusion can be made.

In chapter 7, we considered a different approach to the production of molecular ions in well defined internal states. Rather than cooling, the scheme allows state-specific preparation of molecular ions by a projection measurement on the atomic ion. Again, the creation of correlation between internal degrees of freedom in the molecule and collective motional states of the two ion system is essential to the scheme. The scheme is very versatile and should in principle be applicable to virtually any molecular ion, albeit experimental constraints lead us to focus on lighter molecular ions. The scheme has the important advantage

of being able to prepare the molecular ion in many different internal states, allowing for interesting state-specific studies. While the scheme is technically the most demanding of the presented schemes, an experiment have recently been presented using a similar approach to perform spectroscopy on an atomic ion, which is not amenable for direct cooling [156]. The feasibility of the scheme is thus confirmed, although the experimental demands are considerable.

The state-selected and strongly localized molecular ions produced with the schemes have many potential applications and will be interesting for a large variety of studies. One potential application is high-precision spectroscopy and measurements of absolute reaction rates with molecular ions in a specific internal state. Experiments in ion traps may also complement storage ring experiments of dissociative recombination[92, 131]. Previous experiments in storage rings have shown that dissociative recombination rates for  $D_2H^+$  and  $H_3^+$  depend on the rotational state of the molecular ions [157, 158], thus implying that rotational state specific targets would provide increased understanding of the processes. Furthermore the study of molecular reactions in interstellar media or comet tails [128, 129, 159] could benefit from rotationally cold samples of molecular ions. Ultimately, the access to cold molecular ions could be used in implementations of quantum logic.

# Acknowledgements

First of all, I would like to thank my two supervisors, Lars Bojer Madsen and Michael Drewsen, for four pleasant years under your competent supervision. You are different personalities, but it has been a pleasure working with you both. Most of my daily contact has been with Lars and I would like to thank you especially for being supportive all the way through, even in periods where the project advanced with a snails pace.

During the last four years, lunchtime has generally been blessed with the company of the other theoreticians from the sixth floor. It has amounted to many interesting discussions and only very few dull periods, thanks to Lars and Klaus going great lengths to find an entertaining angle to any story. I would like to thank you all for the company at those lunches. Also, a special thank should be directed at Vivi and Thorbjørn for putting up with my endless complaints about L<sup>A</sup>T<sub>E</sub>X when writing this thesis, and also for taking the time to help. And thanks to Thorbjørn for some good chats and table soccer games during the last months – I think you even won a game once, didn't you? Special thanks also go to Anders and Uffe for proofreading this thesis. My fellow students should also have thanks for many good hours of talks and beer drinking in the friday bar. It may not have been the most intelligent words said in time, but it has been fun.

Finally, I would like to thank my family and friends outside the yellow brick walls of the university. You have always supported me, even when I was slow to return the calls. Thank you very much for that.





# APPENDIX A

## Einstein Coefficients

The most important Einstein coefficients and transition frequencies for the molecular ions treated in chapters 3 and 4 are listed here.

	$A^{rot} (S^{-1})$	$A^{vib} (s^{-1})$	$\omega^{rot} (cm^{-1})$	$\omega^{vib} (cm^{-1})$
$^{24}Mg^1H^+ (X^1\Sigma)$	$2.5 \cdot 10^{-3}$	20.5	12.9	1672
$^{11}B^1H^+ (X^2\Sigma)$	$0.2 \cdot 10^{-3}$ (Q-branch)	11.5	25.0	2437
	$0.4 \cdot 10^{-3}$ (R-branch)	23.0		
$^{16}O^1H^+ (X^3\Sigma)$	$3.8 \cdot 10^{-3}$ (P-branch)	18.3	33.07	2990
	$19.2 \cdot 10^{-3}$ (R-branch)	91.6		
	$11.5 \cdot 10^{-3}$ (Q-branch)	54.9		
	$A^{rot} (S^{-1})$	$A^{vib} (S^{-1})$	$\omega^{rot} (cm^{-1})$	$\omega^{vib} (cm^{-1})$
$^{19}F^1H^+ (X^2\Pi)$	$93.8 \cdot 10^{-3}$ ( $\Omega = \frac{1}{2}$ )	82.4	51.6	2964
	$347 \cdot 10^{-3}$ ( $\Omega = \frac{3}{2}$ )	98.9	85.5	2999

**Table A.1:** Einstein coefficients for selected transitions in  $s^{-1}$  and corresponding transition frequencies in  $cm^{-1}$ .

In the table the quantities have the following meaning:  $A^{rot} = A(\nu = 0, N = 1 \rightarrow \nu = 0, N = 0)$ ,  $A^{vib} = A(\nu = 1, N = 1 \rightarrow \nu = 0, N = 0)$  for the  $\Sigma$ -states and  $A^{rot} = A(\nu = 0, J = \Omega + 1 \rightarrow \nu = 0, J = \Omega)$ ,  $A^{vib} = A(\nu = 1, J = \Omega \rightarrow \nu = 0, J = \Omega)$  for the  $\Pi$ -state. A similar notation is used for the transition frequencies. The pure rotational transition rates (first column) indicate the rotational redistribution speed while the vibrational transition rates give the spontaneous decay rate from the excited vibrational state in the pumping schemes. The data largely explains the qualitative difference in cooling efficiency for the molecular ions. Large rotational redistribution rates indicate a fast scheme, while fast spontaneous decays from the excited vibrational state indicate high effective pump rate, i.e. high cooling efficiency. The data for  $BH^+$  is found using the data from reference [137] and the computer program of reference [102] from which

the Hönl-London factors were corrected to conform with the multiplet expressions of section 4.2.3. Data for  $\text{OH}^+$  was found using the same approach and data from figure 4.7. Finally the data on  $\text{FH}^+$  was obtained using the data of references [135, 136].

# APPENDIX B

## Hönl-London Factors of $^1\Sigma$ States

For completeness we include the details of the derivation of equation (3.8).

Equation (3.4) must be modified if  $\Psi_m$  and  $\Psi_n$  are degenerate. The effective Einstein B-coefficient is found as  $B_{n,m} = \sum_{\mu} \sum_{\xi} \frac{B_{m\xi,n\mu}}{g_n}$ , where  $\mu, \xi$  denote the sub-states of  $\Psi_n$  and  $\Psi_m$ , respectively, and  $g_n$  the degeneracy of the initial (upper) state. One summation is done to include transitions to all sub-states of the final state,  $m$ , while the remaining terms correspond to averaging the result over the sub-states of the initial state. We then define the total transition dipole moment for degenerate states as

$$|\mathcal{D}_{n,m}|^2 = \sum_{\xi,\mu} |D_{n\xi,m\mu}|^2, \quad (\text{B.1})$$

where the summation is done over all transitions between sub-states of the system. The Einstein coefficients between degenerate states then take the form

$$\begin{aligned} B_{n,m} &= \frac{\pi |\mathcal{D}_{n,m}|^2}{3g_n \epsilon_0 \hbar^2} \\ A_{n,m} &= \frac{\hbar \omega^3}{\pi^2 c^3} B_{n,m}, \end{aligned} \quad (\text{B.2})$$

Which is the same as equation (3.4) except for the degeneracy factor. We now move to a molecule-fixed coordinate system. We define the electronic dipole moment function by integrating the dipole operator,  $\mathbf{M}^{mol}$ , over the electronic variables,  $\tau_e$

$$\mathbf{D}_e^{mol}(R) = \int \psi_e(\{\mathbf{r}'_i\}, R)^* \mathbf{M}^{mol} \psi_e(\{\mathbf{r}'_i\}, R) d\tau_e. \quad (\text{B.3})$$

Here we stay in the electronic state defined by the wave function  $\psi_e(R)$  in the body-fixed frame. We have calculated  $\mathbf{D}_e^{mol}(R)$  *ab initio* with *Gaussian* [101]. Details of these calculations are molecule-specific and will be given below.

For  $^1\Sigma$  diatomic molecules the cylindrical symmetry of the potential will ensure that  $\mathbf{D}_e^{mol}(R)$  points along the internuclear axis. Hence the  $Z$ -component of  $\mathbf{D}_e^{mol}(R)$  in the laboratory system is given by

$$\mathbf{D}_e^{lab}(R)_Z = \mathbf{D}_e^{mol}(R) \cdot \hat{Z} = D_e^{mol}(R) \cos \theta. \quad (\text{B.4})$$

The molecular states are degenerate so it is necessary to sum over all sub-states to obtain the transition dipole moment defined in equation (B.1). In the case of  $^1\Sigma$  molecules this corresponds to summing over all projections  $M_J$  of the molecular angular momentum  $\mathbf{J}$ . In carrying out the summation over the sub-states in equation (B.1) the selection rule  $\Delta M_J = 0, \pm 1$  makes it possible to rewrite the expression as a single sum over  $\mu = M_J$  which can be related to the total transition dipole moment. Since the transition probability must be independent of the orientation of the laboratory coordinate system we have

$$|\mathcal{D}_{m,n}^{lab}|^2 = \sum_{M_J} |\mathbf{D}^{lab}|^2 = 3 \sum_{M_J} |\mathbf{D}_Z^{lab}|^2. \quad (\text{B.5})$$

Inserting equation (B.4) in equation (3.5) we find

$$\begin{aligned} \mathbf{D}_Z^{lab} = \int & \psi_{r_n, \nu_n}^{mol}(\theta, \phi, R) \cdot D_e^{mol}(R) \cos \theta \times \\ & \psi_{r_m, \nu_m}^{mol}(\theta, \phi, R) R^2 \sin \theta dR d\theta d\phi, \end{aligned} \quad (\text{B.6})$$

where  $\psi_{r_n, \nu_n}$  and  $\psi_{r_m, \nu_m}$  are the remaining ro-vibrational wave functions obtained after the integration over electronic coordinates in equation (B.3). Now, we assume that the ro-vibrational wave function may be written as a product,  $\Psi_{r_n, \nu_n}(R, \theta, \phi) = \Phi_{r_n}(\theta, \phi) f_{\nu_n}(R)$ . Then

$$|\mathbf{D}_Z^{lab}|^2 = \left| L_{J_n, M_n}^{J_m, M_m} \right|^2 \times \left| \int f_{\nu_n}(R) D_e^{mol}(R) f_{\nu_m}(R) R^2 dR \right|^2, \quad (\text{B.7})$$

with

$$L_{J_n, M_n}^{J_m, M_m} = \int \Phi_{r_n}^{lab*}(\theta, \phi) \cos \theta \Phi_{r_m}^{lab}(\theta, \phi) \sin \theta d\theta d\phi. \quad (\text{B.8})$$

Defining

$$S_{J_m, J_n} = 3 \sum_{M_n, M_m} \left| L_{J_n, M_n}^{J_m, M_m} \right|^2 \quad (\text{B.9})$$

known as the Hönl-London factors [51, 99, 160], we combine the above results with equation (B.5) to find the total transition dipole moment entering equation (B.2)

$$|\mathcal{D}_{m,n}|^2 = S_{J_m, J_n} \left| \int f_{\nu_n}(R) D_e(R) f_{\nu_m}(R) R^2 dR \right|^2. \quad (\text{B.10})$$

# APPENDIX C

## Hönl-London Factors for Hunds Case (a) and (b)

In order to establish proofs of equation (4.3) and (4.11), we here derive the Hönl-London factors for Hunds case (a) and (b).

### C.1 Hunds Case (a)

We use the Hunds case (a) eigenfunctions in the lab frame from [133] (cf. equation (4.2))

$$\langle \{\mathbf{r}_i\} \mathbf{R} | nJM_J\Omega S\Sigma \rangle = \sqrt{\frac{2J+1}{8\pi^2}} \langle \{\mathbf{r}'_i\}, R | n \rangle | S\Sigma \rangle \mathcal{D}_{M_J\Omega}^{J*}(\alpha\beta\gamma), \quad (\text{C.1})$$

and write the  $l$ th component of the  $k$ th moment transition operator in the laboratory frame,  $T_l^k$ , as a similar rotation of the operator working in the molecular rest frame

$$T_l^k(\{\mathbf{r}_i\} \mathbf{R}) = \sum_{\Lambda=-k}^k T_{\Lambda}^k(\{\mathbf{r}'_i\}, R) \mathcal{D}_{l\Lambda}^{k*}(\alpha\beta\gamma). \quad (\text{C.2})$$

Combining the above equations and performing the integral over Euler angles, while writing the Wigner rotation functions as an expansion over Clebsch-Gordan coefficients [44], one finds the dipole moment transition matrix elements ( $k = 1$ )

$$\begin{aligned} \langle n' J' M'_J | T_l^1(\{\mathbf{r}_i\}, \mathbf{R}) | n'' J'' M''_J \rangle = & \\ \sqrt{\frac{2J''+1}{2J'+1}} \sum_{\Lambda=-1}^1 \langle n' \nu' | T_{\Lambda}^1 | n'' \nu'' \rangle & \\ \langle J'' M''_J 1 l | J' M'_J \rangle \langle J'' \Omega'' k \Lambda | J' \Omega' \rangle. & \end{aligned} \quad (\text{C.3})$$

Summing over the projections of  $\mathbf{J}$  and emission directions one finds the line strength

$$\begin{aligned} & \sum_{M'_J, M''_J} |\langle n' J' M'_J | T_l^1(\{\mathbf{r}_i\}, \mathbf{R}) | n'' J'' M''_J \rangle|^2 = \\ & (2J'' + 1) |\langle n' \nu' | T_\Lambda^1 | n'' \nu'' \rangle|^2 \times \\ & |\langle J'' \Omega'' 1(\Omega' - \Omega'') | J' \Omega' \rangle|^2 \delta(S', S'') \delta(\Sigma', \Sigma''). \end{aligned} \quad (\text{C.4})$$

Finally we find the Hönl-London factors in Hunds case (a)

$$\begin{aligned} S(J', J'') &= (2J'' + 1) \times \\ & |\langle J'' \Omega'' 1(\Omega' - \Omega'') | J' \Omega' \rangle|^2 \delta_{S', S''} \delta_{\Sigma', \Sigma''}. \end{aligned} \quad (\text{C.5})$$

## C.2 Hunds Case (b)

We gave the Hunds case (b) eigenfunctions in the laboratory frame in equation (4.10)

$$\begin{aligned} \langle \{\mathbf{r}_i\}, \mathbf{R}, n J M_J N M_N S M_S \rangle &= \sqrt{\frac{2N+1}{8\pi^2}} \times \\ & \sum_{M_S=-S}^S \sum_{M_N=-N}^N \langle \{\mathbf{r}_i\}, R | n \rangle \langle N M_N S M_S | J M_J \rangle \times \\ & |S M_S\rangle \mathcal{D}_{M_N \Lambda}^{N*}(\alpha \beta \gamma). \end{aligned} \quad (\text{C.6})$$

The rotated dipole moment operator was given in a general form in equation (C.2). We then use the identities [134]

$$\begin{aligned} \mathcal{D}_{l\lambda}^k \mathcal{D}_{m\mu}^n &= \sum_{N' M' \mu'} \langle n m k l | N' M' \rangle \times \\ & \langle n \mu k \lambda | N' \mu' \rangle \mathcal{D}_{M \mu'}^{N'} \end{aligned} \quad (\text{C.7})$$

and

$$\int \mathcal{D}_{lm}^k \mathcal{D}_{\lambda\mu}^\kappa d\Omega = \frac{8\pi^2}{2k+1} \delta_{l,\lambda} \delta_{m,\mu} \delta_{k,\kappa}, \quad (\text{C.8})$$

where  $\int d\Omega = \int_0^{2\pi} d\alpha \int_0^{2\pi} d\gamma \int_0^\pi d\beta \sin\beta$ . One thereby finds the expression for the dipole matrix element

$$\begin{aligned} \langle n' J' M'_J | T_l^1(\{\mathbf{r}_i\}, \mathbf{R}) | n'' J'' M''_J \rangle &= \sqrt{\frac{2N''+1}{2N'+1}} \langle n' \nu' | T_{\Lambda'}^1 | n'' \nu'' \rangle \langle N'' \Lambda'' 1(\Lambda' - \Lambda'') | N' \Lambda' \rangle \times \\ & \sum_{\substack{M'_N, M''_N \\ M'_S, M''_S}} \langle N'' M''_N 1 l | N' M'_N \rangle \langle N' M'_N S' M'_S | J' M'_J \rangle \langle N'' M''_N S'' M''_S | J'' M''_J \rangle \delta_{S', S''} \delta_{M'_S, M''_S}. \end{aligned} \quad (\text{C.9})$$

This is summed over the projections of  $\mathbf{J}$  and squared to find the dipole transition probability. The task is simplified by rewriting the products of Clebsch-Gordan coefficients in terms of Wigner 6j symbols [161]. After some algebra one then finds

$$\begin{aligned}
 & |\langle n' J' N' | T_i^1 | n'' J'' N'' \rangle|^2 = \frac{1}{3} (2N'' + 1) \times \\
 & (2J' + 1)(2J'' + 1) \langle n' \nu' | T_{\Lambda' - \Lambda''}^1 | n'' \nu'' \rangle^2 \times \\
 & \langle N'' \Lambda'' 1(\Lambda' - \lambda'') | N' \Lambda' \rangle^2 \left\{ \begin{matrix} S & N'' & J'' \\ 1 & J' & N' \end{matrix} \right\}^2.
 \end{aligned} \tag{C.10}$$

Summing over the emission directions cancels the factor of  $\frac{1}{3}$ , leaving the expression for the Hönl-London factor in Hunds case (b)

$$\begin{aligned}
 S(J', J'') &= (2N'' + 1)(2J' + 1) \times \\
 & (2J'' + 1) \langle N'' \Lambda'' 1(\Lambda' - \Lambda'') | N' \Lambda' \rangle^2 \times \\
 & \left\{ \begin{matrix} S & N'' & J'' \\ 1 & J' & N' \end{matrix} \right\}^2 \delta_{S' S''}.
 \end{aligned} \tag{C.11}$$





# Bibliography

- [1] C. Adams, M. Sigel, and J. Mlyneck, Phys. Rep. **240**, 143 (1994).
- [2] F. Dalfovo et al., Rev. Mod. Phys. **71**, 463 (1999).
- [3] M. Nielsen and I. Chuang, *Quantum computation and Quantum Information* (Oxford University Press, 2000).
- [4] D. Miller, *Atomic and Molecular Beam Methods* (Oxford University Press, 1988).
- [5] S. Y. T. van de Meerakker et al., Phys. Rev. Lett. **94**, 023004 (2005).
- [6] J. Doyle et al., Eur. Phys. J. D **31**, 149 (2004).
- [7] D. Egorov et al., Phys. Rev. A **66**, 043401 (2002).
- [8] M. W. Zwierlein et al., Phys. Rev. Lett. **91**, 250401 (2003).
- [9] S. Jochim et al., Science **302**, 2101 (2003).
- [10] C. A. Regal et al., Nature **424**, 47 (2003).
- [11] M. Greiner, C. A. Regal, and D. S. Jin, Nature **426**, 537 (2003).
- [12] J. Cubizolles et al., Phys. Rev. Lett. **91**, 240401 (2003).
- [13] N. Vanhaecke et al., Phys. Rev. Lett. **89**, 063001 (2002).
- [14] A. J. Kerman et al., PhysRevLett **92**, 153001 (2004).
- [15] J. D. Weinstein et al., Nature **395**, 148 (1998).
- [16] H. Bethlem et al., Phys. Rev. A **65**, 053416 (2002).
- [17] H. Bethlem and G. Meijer, Int. Rev. Phys. Chem. **22**, 73 (2003).
- [18] S. Y. T. van de Meerakker et al., Phys. Rev. A **68**, 032508 (2003).
- [19] J. van Veldhoven, H. L. Bethlem, and G. Meijer, Phys. Rev. Lett. **94**, 083001 (2005).
- [20] S. Y. T. van de Meerakker et al., Phys. Rev. Lett. **94**, 023004 (2005).

- [21] J. R. Bochinski et al., Phys. Rev. Lett. **91**, 243001 (2003).
- [22] M. R. Tarbutt et al., Phys. Rev. Lett. **92**, 173002 (2004).
- [23] M. Zwierlein et al., Phys. Rev. Lett. **92**, 120403 (2004).
- [24] Y. Ohashi and A. Griffin, Phys. Rev. Lett. **89**, 130402 (2002).
- [25] T. Bourdel et al., Phys. Rev. Lett. **93**, 050401 (2004).
- [26] M. H. Szymanska, B. D. Simons, and K. Burnett, Phys. Rev. Lett. **94**, 170402 (2005).
- [27] M. Greiner, C. A. Regal, and D. S. Jin, Phys. Rev. Lett. **94**, 070403 (2005).
- [28] M. Holland et al., Phys. Rev. Lett. **87**, 120406 (2001).
- [29] M. H. Szymańska et al., Phys. Rev. A **72**, 013610 (2005).
- [30] M. Bartenstein et al., Phys. Rev. Lett. **92**, 120402 (2004).
- [31] M. Greiner, C. A. Regal, and D. S. Jin, Phys. Rev. Lett. **94**, 070403 (2005).
- [32] M. Zwierlein et al., Phys. Rev. Lett. **92**, 120403 (2004).
- [33] M. Smith, in *Unimolecular and Biomolecular Reaction Dynamics*, edited by C. Ng, T. Baer, and I. Powis (Wiley, 1994), vol. 1, p. p183.
- [34] R. Krems et al., J. Chem. Phys., **121**, 11639 (2004) **121**, 11639 (2004).
- [35] S. Rice and M. Zaho, *Optical control of molecular Dynamics* (Wiley, 2000).
- [36] S. A. Harich et al., Nature **419**, 281 (2002).
- [37] X. Liu et al., Science **289**, 1536 (2000).
- [38] K. Mølhave and M. Drewsen, Phys. Rev. A **62**, 011401(R) (2000).
- [39] M. A. van Eijkelenborg et al., Phys. Rev. A **60**, 3903 (1999).
- [40] M. Drewsen et al., Phys. Rev. Lett. **93**, 243201 (2004).
- [41] A. Bertelsen, S. Jørgensen, and M. Drewsen, *The rotational temperature of polar molecular ions in coulomb crystals* (2005), physics/0504128.
- [42] A. Bertelsen et al., Eur. Phys. J. D **31**, 403 (2004).
- [43] D. J. Griffiths, *Introduction to Quantum Mechanics* (Prentice Hall, 1995).
- [44] J. J. Sakurai, *Modern Quantum Mechanics* (Addison-Wesley, 1994).
- [45] P. W. Milonni and J. H. Eberly, *Lasers* (Wiley, 1988).
- [46] J. H. Shirley, Phys. Rev. **138**, B979 (1965).

- [47] H. J. Metcalf and P. van der Straten, *Laser Cooling and Trapping* (Springer, 1999).
- [48] B. H. Bransden and C. J. Joachain, *Physics of Atoms and Molecules* (Prentice Hall, 2003), 2nd ed.
- [49] H. Haken and H. C. Wolf, *Molecular Physics and Elements of Quantum Chemistry* (Springer, 1995).
- [50] P. W. Atkins and R. S. Friedman, *Molecular Quantum Mechanics* (Oxford University Press, 2003), 3rd ed.
- [51] K. Huber and G. Herzberg, *Molecular Spectra and Molecular Structure, IV Constants of Diatomic Molecules* (Van Nostrand Reinhold Company, 1979).
- [52] C. H. Townes and A. L. Schawlow, *Microwave Spectroscopy* (McGraw-Hill, 1955).
- [53] H. Lefebvre-Brion and R. W. Field, *Perturbations in the Spectra of Diatomic Molecules* (Academic Press Inc., 1986).
- [54] J. R. Kuklinski et al., *Phys. Rev. A* **40**, 6741 (1989).
- [55] K. Bergmann, H. Theuer, and B. W. Shore, *Rev. Mod. Phys.* **70**, 1003 (1998).
- [56] M. P. Fewell, B. W. Shore, and K. Bergmann, *Aust. J. Phys.* **50**, 281 (1997).
- [57] P. Staantum, PhD thesis, University of Aarhus (2004), the thesis is available at <http://www.phys.au.dk/main/publications/PhD/>.
- [58] U. Gaubatz et al., *J. Chem. Phys.* **92**, 5363 (1990).
- [59] A. Mortensen, PhD thesis, University of Aarhus (2005), the thesis is available at <http://www.phys.au.dk/main/publications/PhD/>.
- [60] J. D. Prestage, G. J. Dick, and L. Maleki, *J. Appl. Phys.* **66**, 1013 (1989).
- [61] M. G. Raizen et al., *Phys. Rev. A* **45**, 6493 (1992).
- [62] M. Drewsen and A. Brøner, *Phys. Rev. A* **62**, 045401 (2000).
- [63] M. Drewsen et al., *Int. J. Mass Spectrom.* **229**, 83 (2003).
- [64] R. F. Wuerker, H. Shelton, and R. V. Langmuir, *J. Appl. Phys.* **30**, 342 (1959).
- [65] C. Monroe et al., *Phys. Rev. Lett.* **65**, 1571 (1990).
- [66] L. Hornekær, PhD thesis, University of Aarhus (2000).
- [67] T. Hänsch and A. Schawlow, *Opt. Comm.* **13**, 68 (1975).
- [68] D. R. Yarkony, *J. Chem. Phys.* **91**, 4745 (1989).

- 
- [69] S. Y. van de Meerakker et al., *Phys. Rev. A* **64**, 041401 (2001).
- [70] E. L. Pollock and J. P. Hansen, *Phys. Rev. A* **8**, 3110 (1973).
- [71] R. F. Wuerker, H. Shelton, and R. V. Langmuir, *J. Appl. Phys.* **30**, 342 (1959).
- [72] M. D. Barrett et al., *Phys. Rev. A* **68**, 042302 (2003).
- [73] N. Kærgaard., *Appl. Phys. B* **71**, 207 (2000).
- [74] T. Koerber et al., *Phys. Rev. Lett.* **88**, 143002 (2002).
- [75] D. J. Berkeland et al., *Phys. Rev. Lett.* **80**, 2089 (1998).
- [76] T. Udem et al., *Phys. Rev. Lett.* **86**, 4996 (2001).
- [77] L. Deslauriers et al., *Phys. Rev. A* **70**, 043408 (2004).
- [78] D. J. Wineland and H. Dehmelt, *Bull. Am. Phys. Soc.* **20**, 637 (1975).
- [79] C. Roos et al., *Phys. Rev. Lett.* **83**, 4713 (1999).
- [80] H. Rohde et al., *J. Opt. B* **3**, S34 (2001).
- [81] C. Monroe et al., *Phys. Rev. Lett.* **75**, 4011 (1995).
- [82] E. Peik et al., *Phys. Rev. A* **60**, 439 (1999).
- [83] C. A. Sackett et al., *Nature* **404**, 256 (2000).
- [84] P. Bowe et al., *Phys. Rev. Lett.* **82**, 2071 (1999).
- [85] M. Drewsen et al., in *AIP conference Proceedings* (1998), vol. 457, p. 305.
- [86] B. B. Blinov et al., *Phys. Rev. A* **65**, 040304(R) (2002).
- [87] B. M. Jelenkovic et al., *Phys. Rev. A* **67**, 063406 (2003).
- [88] H. Rohde et al., *J. Opt. B: Quantum Semiclass. Opt.* **3**, s34 (2001).
- [89] U. Fröhlich et al., *Lect. Notes Phys.* **648**, 297 (2004).
- [90] S. Jørgensen, M. Drewsen, and R. Kosloff, Accepted for publication in *J. Chem. Phys.* (2005).
- [91] D. van Heijnsbergen et al., *Chem. Phys. Lett.* **364**, 345 (2002).
- [92] U. Hechtfischer et al., *Phys. Rev. Lett.* **80**, 2809 (1998).
- [93] D. J. Wineland et al., *J. Res. Natl. Inst. Stand. Technol.* **103**, 259 (1998).
- [94] I. S. Vogelius, L. B. Madsen, and M. Drewsen, *Phys. Rev. Lett.* **89**, 173003 (2002).

- [95] I. S. Vogelius, L. B. Madsen, and M. Drewsen, *Phys. Rev. A* **70**, 053412 (2004).
- [96] I. S. Vogelius, L. B. Madsen, and M. Drewsen, *J. Phys. B*, **37**, 4571 (2004).
- [97] R. Loudon, *The quantum theory of light* (Clarendon Press, 1983).
- [98] J. B. Tatum, *Can. Journ. Phys.* **44**, 2944 (1966).
- [99] I. Kovács, *Rotational Structure in the Spectra of Diatomic Molecules* (Adam Hilger Ltd, 1969).
- [100] E. E. Whiting et al., *J. Mol. Spec.* **47**, 84 (73).
- [101] M. Frisch et al., Tech. Rep., Gaussian inc., Pittsburgh, PA (1995).
- [102] R. J. LeRoy, *Level 7.5: A Computer Program for Solving the Radial Schrödinger Equation for Bound and Quasibound Levels* (2002), the source code and manual for this program may be obtained from the "Computer Programs" link on the www site <http://leroy.uwaterloo.ca>.
- [103] J. B. Foresman and Æ. Frisch, *Exploring Chemistry with Electronic Structure Methods* (Gaussian, Inc., Pittsburgh, PA, 1996), and references therein.
- [104] C. Møller and M. S. Plesset, *Phys. Rev.* **46**, 618 (1934).
- [105] C. W. Bauschlicher and S. R. Langhoff, *Chem. Rev.* **91**, 701 (1991).
- [106] K. P. Lawley, ed., *Advances in Chemical Physics: Ab initio methods in quantum chemistry*, vol. 67 and 69 (Wiley, 1987).
- [107] R. Krishnan and J. A. Pople, *Int. J. Quant. Chem.* **14**, 91 (1978).
- [108] J. A. Pople, M. Head-Gordon, and K. Raghavachari, *J. Chem. Phys.* **87**, 5968 (1987).
- [109] W. Zemke et al., *J. Chem. Phys.* **80**, 356 (1984).
- [110] F. R. Ornellas, W. C. Stwalley, and W. T. Zemke, *J. Chem. Phys.* **79**, 5311 (1983).
- [111] F. B. C. Machado and F. R. Ornellas, *J. Chem. Phys.* **94**, 7237 (1991).
- [112] J. R. Dormand and P. J. Prince, *J. Comp. Appl. Math.* **6**, 19 (1980).
- [113] C. J. H. Schutte, *Chem. Phys. Lett.* **350**, 181 (2001).
- [114] N. Picqué and G. Guelachvili, *J. Chem. Phys.* **113**, 2134 (2000).
- [115] P. Rosmus, *Theor. Chim. Acta* **51**, 359 (1979).
- [116] K. B. Laughlin et al., *Phys. Rev. Lett.* **58**, 996 (1987).

- [117] C. J. H. Schutte, *Chem. Phys. Lett.* **345**, 525 (2001).
- [118] E. V. Kovalchuk et al., *Opt. Lett.* **26**, 1430 (2001), and references therein.
- [119] M. Kimmit et al., *Infrared Phys. Techn.* **37**, 471 (1996).
- [120] C. Winnewisser et al., *Appl. Opt.* **38**, 3961 (1999).
- [121] W. Shi et al., *Appl. Phys. Lett.* **80**, 3889 (2002).
- [122] K. L. Vodopyanov et al., *Appl. Phys. Lett.* **75**, 1204 (1999).
- [123] J. S. Yu et al., *Appl. Phys. Lett.* **82**, 3397 (2003).
- [124] C. Gmachl et al., *Rep. Prog. Phys.* **64**, 1533 (2001).
- [125] See, e.g., *Alpes Lasers*: <http://www.alpeslasers.ch>.
- [126] F. M. Nicolaisen, Private communication (2003).
- [127] J. C. Lagarias et al., *SIAM J. Optim.* **9**, 112 (1998).
- [128] T. P. Snow, in *Interstellar Molecules*, edited by B. H. Andrew (Reidel, Dordrecht, 1992), vol. 87 of *Proceedings of the IAU Symposium*, p. 247.
- [129] L. E. Snyder, in *Astrochemistry of Cosmic Phenomena*, edited by P. D. Singh (Kluwer Academic, Dordrecht, 1992), vol. 150 of *Proceedings of the IAU symposium*, p. 427.
- [130] J. Fišer and J. Vojtík, *Chem. Phys.* **205**, 351 (1996).
- [131] Z. Amitay et al., *Science* **281**, 75 (1998).
- [132] F. Lewen et al., *Rev. Sci. Instrum.* **69**, 32 (1998), see also [www.istok.com](http://www.istok.com).
- [133] J. O. Hornkohl and C. Parigger, *Am. J. Phys.* **64**, 623 (1996).
- [134] D. Brink and G. Satchler, *Angular Momentum* (Clarendon Press, 1994).
- [135] J. V. Coe et al., *J. Chem. Phys.* **90**, 3893 (1989).
- [136] H. J. Werner et al., *J. Chem. Phys.* **80**, 831 (1984).
- [137] R. Klein, P. Rosmus, and H. J. Werner, *J. Chem. Phys.* **77**, 3559 (1982).
- [138] R. Wegmann, K. Jockers, and T. Bonev, *Planet. Space Sci.* **47**, 745 (1999).
- [139] M. Larsson, J. B. A. Mitchell, and I. F. Schneider, eds., *Dissociative recombination: theory, experiment and applications IV* (World Scientific, 1989).
- [140] H. J. Werner, P. Rosmus, and E. A. Reinsch, *J. Chem. Phys.* **79**, 905 (1983).
- [141] D. J. Wineland and W. M. Itano, *Phys. Rev. A* **20**, 1521 (1979).

- [142] M. Abramowitz and I. Stegun, *The Physics and Astronomy Library* (US Government printing office, 1967), 6th ed.
- [143] J. I. Cirac and P. Zoller, *Phys. Rev. Lett.* **74**, 4091 (1995).
- [144] A. Sørensen and K. Mølmer, *Phys. Rev. Lett.* **82**, 1971 (1999).
- [145] D. James, *Appl. Phys. B.* **66**, 181 (1998).
- [146] D. Kielpinski et al., *Phys. Rev. A* **61**, 032310 (2000).
- [147] F. Schmidt-Kaler et al., *Nature* **422**, 408 (2003).
- [148] D. J. Wineland et al., in *Proc. 2003 Joint Meeting IEEE International Frequency Control Symposium and EFTF Conference* (2003), p. 68.
- [149] I. S. Vogelius, L. B. Madsen, and M. Drewsen, *Probabilistic state preparation of a single molecular ion by projection measurement* (2005), submitted for publication, physics/0507181.
- [150] P. A. Barton et al., *Phys. Rev. A* **62**, 032503 (2000).
- [151] P. Staantum et al., *Phys. Rev. A* **69**, 032503 (2004).
- [152] M. A. Rowe et al., *Nature* **409**, 791 (2001).
- [153] C. Monroe et al., *Phys. Rev. Lett.* **75**, 4714 (1995).
- [154] A. C. Albrecht, *J. Chem. Phys.* **34**, 1476 (1961).
- [155] B. DeMarco et al., *Phys. Rev. Lett.* **89**, 267901 (2002).
- [156] P. Schmidt et al., *Science* **30**, 749 (2005).
- [157] L. Lammich et al., *Phys. Rev. Lett.* **91**, 143201 (2003).
- [158] B. J. McCall et al., *Nature* **422**, 500 (2003).
- [159] T. W. Hartquist and D. A. Williams, *The Chemically Controlled Cosmos - Astronomical Molecules from the Big Bang to Exploding Stars* (Cambridge University Press, Cambridge, 1995).
- [160] H. Hönl and F. London, *Z. Physik* **33**, 803 (1925).
- [161] I. I. Sobelman, *Atomic Spectra and Radiative Transitions* (Springer, 1992), 2nd ed.